

INFORMATION TO USERS

This reproduction was made from a copy of a document sent to us for microfilming. While the most advanced technology has been used to photograph and reproduce this document, the quality of the reproduction is heavily dependent upon the quality of the material submitted.

The following explanation of techniques is provided to help clarify markings or notations which may appear on this reproduction.

1. The sign or "target" for pages apparently lacking from the document photographed is "Missing Page(s)". If it was possible to obtain the missing page(s) or section, they are spliced into the film along with adjacent pages. This may have necessitated cutting through an image and duplicating adjacent pages to assure complete continuity.
2. When an image on the film is obliterated with a round black mark, it is an indication of either blurred copy because of movement during exposure, duplicate copy, or copyrighted materials that should not have been filmed. For blurred pages, a good image of the page can be found in the adjacent frame. If copyrighted materials were deleted, a target note will appear listing the pages in the adjacent frame.
3. When a map, drawing or chart, etc., is part of the material being photographed, a definite method of "sectioning" the material has been followed. It is customary to begin filming at the upper left hand corner of a large sheet and to continue from left to right in equal sections with small overlaps. If necessary, sectioning is continued again—beginning below the first row and continuing on until complete.
4. For illustrations that cannot be satisfactorily reproduced by xerographic means, photographic prints can be purchased at additional cost and inserted into your xerographic copy. These prints are available upon request from the Dissertations Customer Services Department.
5. Some pages in any document may have indistinct print. In all cases the best available copy has been filmed.

**University
Microfilms
International**

300 N. Zeeb Road
Ann Arbor, MI 48106



8414631

Hertzog, David William

**A PRECISION MEASUREMENT OF THE MAGNETIC MOMENT OF THE
SIGMA MINUS HYPERON**

The College of William and Mary in Virginia

PH.D. 1983

**University
Microfilms
International** 300 N. Zeeb Road, Ann Arbor, MI 48106

PLEASE NOTE:

In all cases this material has been filmed in the best possible way from the available copy. Problems encountered with this document have been identified here with a check mark .

1. Glossy photographs or pages _____
2. Colored illustrations, paper or print _____
3. Photographs with dark background _____
4. Illustrations are poor copy _____
5. Pages with black marks, not original copy _____
6. Print shows through as there is text on both sides of page _____
7. Indistinct, broken or small print on several pages
8. Print exceeds margin requirements _____
9. Tightly bound copy with print lost in spine _____
10. Computer printout pages with indistinct print _____
11. Page(s) _____ lacking when material received, and not available from school or author.
12. Page(s) _____ seem to be missing in numbering only as text follows.
13. Two pages numbered _____. Text follows.
14. Curling and wrinkled pages _____
15. Other _____

University
Microfilms
International

**A PRECISION MEASUREMENT OF THE MAGNETIC MOMENT
OF THE SIGMA MINUS HYPERON**

A Dissertation

Presented to

**The Faculty of the Department of Physics
The College of William and Mary in Virginia**

In Partial Fulfillment

Of the Requirements for the Degree of

Doctor of Philosophy

by

David William Hertzog

June 1983

APPROVAL SHEET

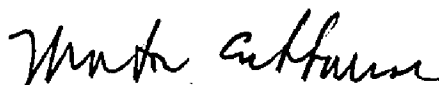
This dissertation is submitted in partial fulfillment of
the requirements for the degree of

Doctor of Philosophy



David W. Hertzog

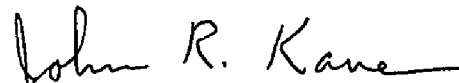
Approved, June 1983



Morton Eckhause

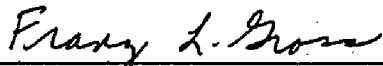


Carl E. Carlson



John R. Kane

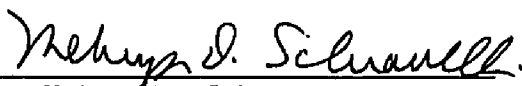
John R. Kane



Franz L. Gross



Rolf G. Winter



Melvyn D. Schiavelli
Department of Chemistry

DEDICATION

**To my parents William and Verletta Hertzog
for instilling the dream**

AND

**To my wife Nancy
for the love, encouragement, and support
necessary for the fulfillment of that dream**

CONTENTS

ACKNOWLEDGMENTS	vi
ABSTRACT	x
<u>Chapter</u> <u>page</u>	
I. INTRODUCTION	1
II. THEORY	7
Additive Quark Model	8
Bag Models	16
Chiral Bag Models	16
The Little Bag	17
The Cloudy Bag	19
Summary	20
III. ATOMIC PHYSICS CONSIDERATIONS	21
Choice of Targets (Z,A)	23
Atomic Capture and Cascade	26
Non-Circular Transitions	27
Spin-up to Spin-down Intensity Ratio	28
IV. EXPERIMENTAL METHOD	30
Introduction	30
K ⁻ Beam	32
Experimental Arrangement and Geometry	33
Kaon Stop Identification	34
Hydrogen Target	37
π ⁺ Spectrometers	37
X-ray Spectroscopy	41
Data Acquisition	46
Events	46
Computer System	49
CAMAC Gating	50
Data Acquisition Software	50
V. TESTS OF THE SYSTEM AND ANALYSIS OF THE DATA	53
Data Set Characteristics	53
Tape Replay	54
Requirements for Fine-Structure Analysis	57
Detector Resolution	58

Determination of Non-Circular Contributions	62
Detector Relative Efficiency	63
Target Transmission	64
Laboratory Measurement	64
Monte-Carlo Method	65
Comparison of K^- X-ray Yields	66
Cascade Calculation	67
Measured Values	67
Calculated Values	68
Strong-Interaction Effect on the $n=10$ State	70
New Determination of Magnetic Moment	71
The Sign of the Magnetic Moment	72
The Magnitude of the Magnetic Moment	75
Determination of Systematic Errors	79
Tests of the Fitting Technique	80
Computer Simulations	80
Laboratory Simulations	81
Sensitivity of Magnetic Moment to Input Parameters	82
 VI. CONCLUSIONS	 84
Theoretical Implications	86
 REFERENCES	 88
LIST OF TABLES	93
FIGURE CAPTIONS	95
FIGURES	98

ACKNOWLEDGMENTS

I am particularly indebted to the following people for their valuable contributions to and assistance in this work:

Dr. Morton Eckhause, my advisor, for his attention to detail with the electronics logic, the runs, the analysis, and the reading of several drafts of the manuscript, and, especially for his guidance and kindness shown to me throughout my graduate studies.

Dr. John Kane, for his significant contributions to the design of the π^+ spectrometer system and the laminar targets, and, for always having an open door and a willingness to talk about the experiment.

Dr. Robert Welsh, for suggesting this experiment, guiding its organization, negotiating the design of the Ge detector array, for many creative ideas, and for his positive outlook and excellent sense of humor which often inspired me when things looked bleak.

Dr. Rolf Winter, for many discussions during the design and analysis phases of this work, and for often giving me the necessary confidence that my approach to the analysis of the data was correct.

Mr. William Vulcan, electronics engineer, for tutoring me in electronics, computers, and general experimental knowhow, and for the many favors extended to me.

Dr. Robert Whyley for significant assistance during the data runs, for many programming contributions, numerous discussions about the data analysis, and help in preparing several presentations of the results.

Dr. Franz Gross for several helpful discussions about the theory.

Drs. Lee Roberts and James Miller for contributions to the design and running of the experiment and for many discussions during the analysis of the data.

Dr. Roger Sutton for the development of many of the beam telescope counters, Monte-Carlo simulations, and help in the experimental runs.

Dr. Raymond Kunselman for work with the cascade program and help during the experimental runs.

Fellow graduate students William Phillips and Fran O'Brien for their constant dedication to the experiment, their many long working hours, and for their individual significant contributions which helped make this work a success.

Mr. Timothy Williams for tireless work developing the computer plotting routines used to display the data in this manuscript.

Dr. David Ritchie and Mr. Timothy Miles for providing distributions of MULTI and for many suggestions which aided in its implementation and in the introduction of our modifications.

Dr. Walter Dey for teaching me the basics of data acquisition programming and for writing the original PDP data acquisition program.

Dr. Rene Hartmann for many useful discussions and calculations during the design phases of this experiment.

My other fellow collaborators on this experiment, Dr. George Dodson for many contributions to the preparation of the experiment, Mr. Nick Colella for development of the hodoscope array, Mr. Dan Tieger for

providing useful wire chambers, Dr. Dick Powers for helpful discussions about the atomic physics aspects of the analysis, and Dr. Kevin Giovanetti for important discussions throughout all phases of this work.

Dr. Phil Pyle for significant assistance in tuning the beam.

The entire staff of the AGS for their hospitality and for the excellent operation of the accelerator, and in particular, the Hydrogen Target Group, for the construction of the laminar targets, and the Electronics Group, for their exceptional help and service.

Mr. Richard Pehl, Mr. Fred Goulding, Mr. Donald Landis, and Mr. Norm Madden of Lawrence Berkeley Laboratory and Mr. Rex Trammell of Ortec for the development of the Ge detector array and associated electronics.

Dr. Edith Borie for a copy of her computer program to calculate electromagnetic energies.

Drs. Vanamali Raghunathan and Donald Joyce for many useful discussions.

Dr. John Bensei, Mr. Melvin Woods, and Mr. Norman Rainville of the William and Mary physics machine shop for production of the π^+ spectrometer scintillation counters.

The operators and staff of the William and Mary computer center for efficient throughput of the many jobs necessary for the Monte-Carlo designing of the experiment and analysis of the data.

Ms. Sylvia Stout for helping with the many details encountered during my six years at William and Mary.

Finally, it has been a particular privilege to have been associated with the William and Mary physics department. It is a department

large enough to provide many areas of significant research opportunities, yet small enough so that everyone can know each other well.

This work was supported in part by the National Science Foundation.

ABSTRACT

A new measurement of the magnetic moment of the Σ^- hyperon has been made and the result is $\mu(\Sigma^-) = -1.111 \pm 0.031 \pm 0.011$ nuclear magnetons.

Negative kaons from a low-energy separated beam at the Alternating Gradient Synchrotron of the Brookhaven National Laboratory were brought to rest in a novel laminar target consisting of thin metal foils immersed in liquid hydrogen. The production of Σ^- hyperons occurred primarily through the reaction $K^- p \rightarrow \Sigma^- \pi^+$. Σ^- hyperon production was tagged by the identification of the energetic π^+ . Many of the Σ^- so produced stopped in nearby foils of Pb (or W) where atomic capture into a highly excited state could occur. The energies of the subsequent de-excitation x rays were recorded with three high-resolution intrinsic Ge detectors located below the target. The tagging technique resulted in an enhancement of 15 in x-ray signal-to-noise compared to that of previous Σ^- exotic atom experiments. The $\Sigma^- \text{Pb}(11-10)$, $\Sigma^- \text{Pb}(12-11)$, and $\Sigma^- \text{W}(11-10)$ transitions were analyzed for fine-structure from which the Σ^- magnetic moment was deduced. Self-consistent results were obtained from the three transitions and from the data accumulated in each detector.

**A PRECISION MEASUREMENT OF THE MAGNETIC MOMENT
OF THE SIGMA MINUS HYPERON**

Chapter I

INTRODUCTION

The study of magnetic moments in particle physics has led to important progress in understanding the structure of matter. In 1922, Stern and Gerlach¹ demonstrated the concept of space-quantization by passing a beam of neutral silver atoms through an inhomogeneous magnetic field. The beam split into two patterns because of the net force acting on distinctly aligned orientations of an internal magnetic moment within the system. Uhlenbeck and Goudsmit,² in an attempt to explain their own observations in the optical spectra of alkali atoms, postulated that the electron contained an internal degree of freedom associated with an angular momentum component. Gibbs and Taylor³ repeated the experiment of Stern and Gerlach with a neutral hydrogen beam and confirmed that the observations in silver atoms were due to quantization of electron spin. The splitting observed in the latter experiment was unambiguously associated with an intrinsic magnetic moment of the electron. Dirac⁴ later developed a theory for pointlike, spin- $\frac{1}{2}$ particles which rigorously described the observations in terms of energy eigenvalues corresponding to the projection on any selected z axis of an intrinsic magnetic moment having the two values

$$\mu_z = \pm \frac{e\hbar}{2m_e c}. \quad (1.1)$$

The relationship between the magnetic moment μ of a particle and its intrinsic spin vector \mathbf{S} is given by

$$\mu = g\mu_b\mathbf{S}, \quad (1.2)$$

where the Bohr magneton is defined by

$$\mu_b = \frac{q\hbar}{2mc}, \quad (1.3)$$

for a particle with charge q and mass m . The g -factor is exactly equal to 2 in the Dirac theory for pointlike spin- $\frac{1}{2}$ particles. In precise experiments, slight deviations from the value of 2 for the g -factors of electrons and muons have been measured.⁵ These deviations can be accounted for and are predicted by quantum electrodynamical (QED) effects such as virtual photon emission and vacuum polarization and have been calculated⁵ to order α^2 in one of the most sensitive tests of the remarkably successful quantum electromagnetic theory.

In contrast to the pointlike structure characteristic of leptons, baryons exhibit a more complex inner structure as evidenced in their large "anomalous" magnetic moments; i.e., in the large deviations of g from 2. The family of particles in the $J^{\pi}=\frac{1}{2}^{+}$ baryon octet consists of the neutron (n), proton (p), lambda hyperon (Λ^0), sigma hyperons (Σ^{+} , Σ^0 , Σ^{-}), and the cascade hyperons (Ξ^0 and Ξ^{-}). All of these hadrons can be described by quark models and their magnetic moments calculated from the summed contributions of three constituent quarks and their associated interaction fields. A systematic study of the magnetic moments of baryons provides stringent constraints on the theoretical models used to describe baryon structure. A review of recent theoretical work is given in Chapter II.

The magnitude μ_B of the magnetic moment of a baryon of mass m_B can be expressed as

$$\mu_B = (g_0 + g_1) \frac{e\hbar}{2m_B c} \quad (1.4)$$

where g_0 is the Dirac component equal to the charge of the particle in units of e , and g_1 represents the anomalous magnetic moment contribution. The magnetic moment μ_B in Eq. (1.4) is expressed in terms of the Bohr magneton of the baryon. In this report, however, baryon magnetic moments will be given in nuclear magnetons $\mu_N = e\hbar/2m_p c$, which is the more commonly quoted unit in the literature. Thus, $\mu_B = (g_0 + g_1) m_p / m_B \mu_N$.

In the past few years, measurements of the magnetic moments of the Λ^0 , Ξ^0 , Ξ^- , Σ^+ , and Σ^- hyperons have been reported.⁶⁻¹¹ The neutron and proton magnetic moments have been precisely known for some time.¹² Generally, magnetic moments of strange baryons have been obtained by correlating the decay trajectories from polarized hyperons with the precession applied to the hyperon spin by a relatively strong magnetic field. All of the hyperons exhibit an angular asymmetry in their decay relative to their spin direction due to the parity violating weak interaction. For strange baryons with large values of the asymmetry parameter a , this precession technique works well. For the Σ^- hyperon, with the small value $a \simeq 0.07$, the first reported measurement¹¹ of its magnetic moment by the precession technique has led to a result less precise than that for other strange-baryon magnetic moments. A second group¹³ has recently reported preliminary results for $\mu(\Sigma^-)$ which were obtained in a manner similar to that in Ref. 11. Their sam-

ple of data is significantly larger but the analysis is not complete. Recent values obtained from precession experiments at Fermilab for the magnetic moments of strange baryons are listed in Table I.

TABLE I
Recent Measurements of Strange Baryon Magnetic Moments in Precession Experiments

Particle	Ref.	Asymmetry Parameter	Magnetic Moment (μ_N)
Λ^0	6	0.642	-0.6138 ± 0.0047
Σ^+	9	-0.979	2.33 ± 0.03
	13		$2.368 \pm 0.014 \pm 0.04^*$
Σ^-	11	-0.068	-0.89 ± 0.14
	13		$-1.180 \pm 0.028 \pm xx^*$
Ξ^0	7	-0.413	-1.250 ± 0.014
Ξ^-	8	-0.434	-0.69 ± 0.04

* Preliminary results, statistical and systematic errors given
xx -- Tests of systematics not complete

The Σ^- magnetic moment can alternatively be measured by an atomic physics technique which is described next and which forms the basis of the experiment reported here. When a negatively charged heavy ($m \gg m_e$) particle ($\mu^-, \pi^-, K^-, \bar{p}, \Sigma^- \dots$) comes to rest in a material, atomic capture can occur. The atomic capture takes place in an excited state of the system and de-excitation follows. Initially, Auger transitions occur while the exotic particle is in high-lying states. When the particle cascades to the lower levels, radiative transitions

begin to dominate with selection rules which govern such processes. As the particle makes these transitions, x rays are emitted with energies equal to the differences in energies of the atomic levels of the system consisting of the exotic particle and the corresponding nucleus. The Dirac or Klein Gordon equation, depending on the spin of the orbiting particle, can be solved for the energies of these levels.

Electromagnetic corrections for such effects as vacuum polarization, finite nuclear size, reduced mass, electron screening, and nuclear recoil must be included to calculate the precise energies of the levels. The masses of the muon, pion, kaon, antiproton, and sigma hyperon have been determined from precise measurements of the energies of the x rays emitted by exotic atoms containing these particles.¹⁴

If the particle is a fermion, e.g. μ^- , \bar{p} , Σ^- , the energy levels of an atomic state of principal quantum number n are split by the interaction of the orbital motion and the magnetic moment of the particle. The splitting of an atomic level of given n and orbital quantum number ℓ is approximately:

$$\Delta E = (g_0 + 2g_1) \frac{(\alpha Z)^4}{2n^3} \frac{m}{\ell(\ell+1)} \quad (1.5)$$

where α is the fine-structure constant, Z is the nuclear charge, and m is the reduced mass of the system. The technique of measuring the splitting of atomic levels has been used to determine the magnetic moment of the antiproton and of the sigma hyperon.¹⁵⁻¹⁸

We have performed new measurements of the fine-structure splittings for several $\Sigma^- \text{Pb}$ and $\Sigma^- \text{W}$ atomic transitions and have deduced a corresponding value for $\mu(\Sigma^-)$. Considerable refinements in the experimental technique have resulted in a measurement of

$\mu(\Sigma^-)$ to a precision of $\pm 0.04 \mu_N$.

A review of the theoretical motivation and current quark-model predictions for baryon magnetic moments is given in Chapter II. The relevant atomic physics considerations are outlined in Chapter III. Details of the experimental technique are discussed in Chapter IV and the presentation and analysis of the data are given in Chapter V. Results are described and conclusions drawn in Chapter VI.

Chapter II

THEORY

At the present time, the quark model is well established and the prescription for hadron structure is defined. Quarks (q) are spin- $\frac{1}{2}$ Dirac particles that exist in a variety of flavors ($u, d, c, s, t?, b, \dots$) and corresponding charges ($\frac{2}{3}, -\frac{1}{3}, \frac{2}{3}, -\frac{1}{3}, \dots$). They additionally possess an internal degree of freedom denoted as color (e.g. red, white, or blue). Baryons are composed of qqq combinations and mesons are composed of $q\bar{q}$ pairs where a bar denotes an antiquark. The couplings of quarks within hadrons are governed by the exchange of colored, massless, neutral gluons.

At high energies (short distances), quarks behave as if they couple weakly and perturbative quantum chromodynamics (QCD) has been used with great success to calculate the interactions of hadrons. At low energies, however, the coupling becomes large and the perturbative QCD approach breaks down. Furthermore, since free quarks and gluons are not observables of nature and since QCD does not yet provide a confinement mechanism, the study of hadron static properties has evolved from a more phenomenological approach.

In the following, calculations of the magnetic moments of the members of the $J^{\pi} = \frac{1}{2}^{+}$ baryon octet will be discussed. Calculations in the framework of the non-relativistic additive quark model (AQM) (also called the "naive" or "simple" quark model) and in that of the bag mod-

els will be presented. The Σ^- hyperon magnetic moment will be used as an example and specific tests for which a precise measurement of $\mu(\Sigma^-)$ has direct implications will be emphasized.

2.1 ADDITIVE QUARK MODEL

If one considers only three flavors of quarks (u,d,s) and allows each of these to be in one of two spin states (\uparrow, \downarrow), then there are six base states from which the baryons can be constructed. The symmetry group¹⁹ is called SU(6), or SU(3)_{flavor} X SU(2)_{spin}. By forming all possible combinations of the six states into three-quark groups we get

$$6 \times 6 \times 6 = 20 + 70 + 70 + 56 \quad (2.1)$$

irreducible possibilities where only the 56-plet forms a completely symmetric wavefunction in spin-flavor indices. The space wavefunction is assumed to be symmetric, having quarks in the ground state (angular momentum = 0), and the statistics of fermions are therefore accounted for by an antisymmetric color wavefunction. Within the 56-plet, sixteen states, designated (2,8), and forty states, designated (4,10), form the spin- $\frac{1}{2}$ baryon octet and spin- $\frac{3}{2}$ decuplet, respectively. The first number in parenthesis represents the spin multiplicity $2J+1$ for each "physical" particle. The second represents the number of different spin-flavor combinations which can be formed independent of the overall spin orientation.

We next form the wavefunction for a Σ^- hyperon (qqq=dds). The spin and flavor pieces are each antisymmetric. Two quarks can be placed in an antisymmetric spin singlet state

$$\frac{1}{\sqrt{2}} (\uparrow\downarrow - \downarrow\uparrow), \quad (2.2)$$

and coupled to an antisymmetric combination of d and s

$$\sqrt{\frac{1}{2}} (ds - sd). \quad (2.3)$$

Combining these, we obtain

$$\frac{1}{2} (\uparrow\downarrow - \downarrow\uparrow)(ds - sd), \quad (2.4)$$

and adding the final d quark,

$$\frac{1}{2} (d\uparrow s\downarrow - d\downarrow s\uparrow - s\uparrow s\downarrow + s\downarrow d\uparrow) d\uparrow \quad (2.5)$$

which is totally symmetric only when all cyclic permutations are considered. We therefore must write,

$$\begin{aligned} \phi_{\Sigma^-} = 1/\sqrt{18} \{ & 2d\uparrow d\uparrow s\downarrow + 2s\downarrow d\uparrow d\uparrow + 2d\uparrow s\downarrow d\uparrow \\ & - d\downarrow s\uparrow d\uparrow - d\uparrow d\downarrow s\uparrow - d\downarrow d\uparrow s\uparrow \\ & - s\uparrow d\downarrow d\uparrow - d\uparrow s\uparrow d\downarrow - s\uparrow d\uparrow d\downarrow \}. \end{aligned} \quad (2.6)$$

The calculation of magnetic moments within this framework presupposes that the quarks are massive, non-relativistic Dirac particles, each having a magnetic moment proportional to its charge-to-mass ratio,

$$\mu_q = \frac{e_q \hbar}{2m_q c}. \quad (2.7)$$

The baryon magnetic moment $\mu(B)$ is just the vector sum of the constituent moments.

We calculate $\mu(\Sigma^-)$ in such a manner. If

$\mu = \sum_i \mu_i \sigma_i$ is the magnetic moment operator, then

$$\mu(\Sigma^-) = \langle \phi_{\Sigma^-} | \sum_i \mu_i \sigma_i | \phi_{\Sigma^-} \rangle \quad (2.8)$$

and the z-projection of μ is obtained as follows

$$\begin{aligned}
\mu(\Sigma^-) &= 3/18 \{ \langle 2d\uparrow d\uparrow s\downarrow | \sum_i \mu_i \sigma_{iz} | 2d\uparrow d\uparrow s\downarrow \rangle \\
&\quad + \langle d\uparrow d\uparrow s\uparrow | \sum_i \mu_i \sigma_{iz} | d\uparrow d\uparrow s\uparrow \rangle \\
&\quad + \langle d\uparrow d\downarrow s\uparrow | \sum_i \mu_i \sigma_{iz} | d\uparrow d\downarrow s\uparrow \rangle \} \\
&= 3/18 \{ 4(\mu_d + \mu_d - \mu_s) + (-\mu_d + \mu_d + \mu_s) + (\mu_d - \mu_d + \mu_s) \} \\
&= \frac{1}{3}\mu_d - \frac{2}{3}\mu_s, \tag{2.9}
\end{aligned}$$

an expression which requires only the value of the quark masses for further evaluation. (Eq. (2.9) can be extended to the other baryons $\mu(qqq')$ = $\frac{1}{3}\mu_q - \frac{2}{3}\mu_{q'}$, except that $\mu(\Lambda^0) = \mu_s$ only). In the limit of exact $SU(3)$ flavor, the quark masses are equal and Eq. (2.9) is equivalent to the Coleman - Glashow relation²⁰

$$\mu(\Sigma^-) = -\{\mu(p) + \mu(n)\} = -0.93 \mu_N \tag{2.10}$$

where μ_N is the nuclear magneton, a unit which will henceforth be implied for all baryon magnetic moments. One of the early successes of the $SU(6)$ predictions²¹ for magnetic moments was the ratio $\mu(p)/\mu(n) = -\frac{1}{2}$ which was used to evaluate Eq. (2.10).

Baryon masses and magnetic moments are more accurately described if symmetry breaking of the quark masses is allowed. DeRujula, Georgi, and Glashow²² (DRGG) deduced from the hadron mass spectrum the mass ratio

$$y = \frac{m_u (= m_d)}{m_s} = 0.622, \tag{2.11}$$

which follows from the relation

$$y = \frac{2(m_{\Sigma^*} - m_{\Sigma})}{2m_{\Sigma^*} + m_{\Sigma} - 3m_{\Lambda}}. \quad (2.12)$$

The quark masses were then calculated by noting that $\mu(p) = \frac{1}{3}\mu_u - \frac{1}{3}\mu_d = e\hbar/2m_u c$ for $m_u = m_d$; hence, $m_u = m_p/\mu(p) = 336$ MeV. It follows from Eq. (2.11) that $m_s = 540$ MeV. We can now evaluate $\mu(\Sigma^-)$:

$$\begin{aligned} \mu(\Sigma^-) &= \frac{4}{3} \left(\frac{-e/3\hbar}{2(336)} \right) - \frac{1}{3} \left(\frac{-e/3\hbar}{2(540)} \right) \\ &= (-1.24 + 0.19) \frac{e\hbar}{2(939)} \\ &= -1.05 \mu_N. \end{aligned} \quad (2.13)$$

The experimentally measured magnetic moments of the $\frac{1}{2}^+$ baryons are listed in Table II. Those denoted "Broken SU(6) I" were taken from Ref. 22. If the condition $m_u = m_d$ is further relaxed and the neutron and lambda-hyperon magnetic moments used as additional input, then we obtain the results listed in the column labeled "Broken SU(6) II." Experimental numbers are included for comparison. For $\mu(\Sigma^-)$, we list only that of Ref. 11, deferring comment regarding the result reported here to Chapter VI.

The prediction²¹ for the $\mu(p)/\mu(n)$ ratio is one of the great triumphs of SU(6) theory. With the addition of mass breaking,²² the Λ^0 magnetic moment is predicted remarkably well. However, the calculation of other baryon magnetic moments is only qualitatively acceptable. The Σ^+ magnetic moment should be very nearly the same as that of the proton, namely, $(\frac{1}{3}\mu_u - \frac{1}{3}\mu_s)$ vs $(\frac{1}{3}\mu_u - \frac{1}{3}\mu_d)$. The small difference be-

TABLE II
Theoretical and Experimental Magnetic Moment Values

Particle	Experiment	Broken SU(6) I Ref. 22	Broken SU(6) II Ref. 34	Lipkin Ref. 39	Little Bag $\delta = 0.4$ Ref. 50	CBM Ref. 52
p	2.793	---	---	---	---	2.60
n	-1.913	-1.86	---	---	---	-2.01
Λ^0	-0.614 ± 0.005	-0.60	---	---	---	-0.58
Σ^+	2.33 ± 0.03	2.67	2.67	2.24	2.28	2.34
Σ^-	$-0.89 \pm 0.14^*$	-1.05	-1.09	-0.81	-0.64	-1.08
Ξ^0	-1.25 ± 0.014	-1.39	-1.44	-1.22	-1.33	-1.27
Ξ^-	-0.69 ± 0.04	-0.46	-0.50	-0.61	-0.60	-0.51

* Ref. 11 only

tween the contribution of the s quark in the Σ^+ and the d quark in the proton cannot account for the observed difference in magnetic moments between these two particles. The Ξ^- presents another problem. Since $\mu(\Xi^-) = (\frac{1}{2}\mu_s - \frac{1}{2}\mu_d)$, and $\mu(\Lambda^0) = \mu_s$, the inequality $\mu_s < \mu_d$ guarantees that $\mu(\Xi^-) < \mu(\Lambda^0)$. Experimentally, the reverse is true. Finally, one also notes that the experimental value of $\mu(\Xi^0)$ is lower in magnitude than the corresponding prediction. The experimental value of $\mu(\Sigma^-)$ from Ref. 11 is not of sufficient precision to test the theory.

Numerous variations²³⁻⁴⁰ on the AQM and discussions of its underlying difficulties⁴¹⁻⁴³ have been published, especially in light of

the precise measurements of hyperon magnetic moments now available. Such studies have suggested, for example, introducing "effective" or anomalous magnetic moments,^{26,31,35} redefining the mass scales and the mass-breaking ratio y ,^{28-30,36} breaking SU(3) spin symmetry,^{27,33,37} introducing mechanisms for reducing the moments of strange baryons,³⁹ considering quark-diquark clusters,³⁸ including harmonic oscillator potentials,^{32,40} and estimating the contributions of nonstatic effects.^{25,32,34} In this report, we limit the discussion to two examples in which a new measurement of $\mu(\Sigma^-)$ has direct implications.

Sum rules^{23,25} can be used to isolate nonstatic contributions of individual quark moments in different baryons. The spin-independence assumption in SU(6) which requires quarks in different spin states to contribute to the overall baryon magnetic moment by the vector addition of their Dirac moments can be tested by one such set of rules.³⁴ The spin wavefunction for each of the octet members considered here, except the Λ^0 , is formed from the coupling of a spin-1 piece (for the two like quarks qq) and a spin- $\frac{1}{2}$ piece (for the third quark q'). In the Λ^0 , the u and d quarks align their spins in opposite directions to form a spin-0 component. The s quark provides the baryon spin and magnetic moment; i.e., $\mu(\Lambda^0) = \mu_s$. The following three relations isolate the s -quark magnetic moment in different baryons:

$$\mu_S(\Lambda) = \mu(\Lambda^0) \quad (2.14.a)$$

$$\begin{aligned} \mu_S(\Xi) &= \frac{1}{2}(\frac{1}{2}\mu_S - \frac{1}{2}\mu_U) + \frac{1}{2}(\frac{1}{2}\mu_S - \frac{1}{2}\mu_D) \\ &= \frac{1}{2}\mu(\Xi^0) + \frac{1}{2}\mu(\Xi^-) \end{aligned} \quad (2.14.b)$$

$$\begin{aligned} \mu_S(\Sigma) &= -(\frac{1}{2}\mu_U - \frac{1}{2}\mu_S) - 2(\frac{1}{2}\mu_D - \frac{1}{2}\mu_S) \\ &= -\mu(\Sigma^+) - 2\mu(\Sigma^-), \end{aligned} \quad (2.14.c)$$

where the SU(6) result $\mu_U = -2\mu_D$ has been used. Evaluating Eqs. (2.14.a) and (2.14.b) with experimental quantities, gives $\mu_S(\Lambda) = -0.614 \pm 0.005$ and $\mu_S(\Xi) = -0.66 \pm 0.02$ which are in good agreement considering the assumptions used. Equation (2.14.c) can be rewritten by substituting the experimental quantity for $\mu(\Sigma^+)$ and the weighted average of $\mu_S(\Lambda)$ and $\mu_S(\Xi)$ for $\mu_S(\Sigma)$ to obtain the prediction

$$\begin{aligned} \mu(\Sigma^-) &= -\frac{1}{2}[(2.33 \pm 0.03) + (-0.615 \pm 0.005)] \\ &= -0.86 \pm 0.015 \end{aligned} \quad (2.15)$$

In the absence of spin-symmetry breaking effects, Eq. (2.15) should be approximately satisfied.

Next we discuss the recent analysis by Lipkin³⁹ of hyperon magnetic moments and hyperon-nucleon cross sections. Lipkin concludes that the data on both could be characterized by a model having two parts:

- i) a flavor symmetric contribution satisfying the AQM
- ii) an enhancement of the contributions of nonstrange quarks, which breaks both flavor-symmetry and additivity simultaneously

The following procedure is used to incorporate these parts into an expression for magnetic moments. First, exact SU(3) component wavefunc-

tions are constructed and the mass scale chosen to fit the magnetic moment of the Λ^0 (instead of the moment of the proton, as has been customary). Next, the ad hoc factor of $(1 + \frac{1}{3}(N-1))$ is introduced, with N equal to the number of nonstrange quarks in the baryon. Lipkin obtains the following formula for computing the moments:

$$\begin{aligned} \mu(qqq') &= (4q - q')\mu(\Lambda^0) \\ &+ [2qx(x+x') - q'xx']\frac{1}{3}\mu(\Lambda^0), \end{aligned} \quad (2.16)$$

where in this case q represents the quark charge and the factor x has the value 0 for strange quarks and 1 for nonstrange quarks. For $\mu(\Sigma^-)$,

$$\begin{aligned} \mu(\Sigma^-) &= (\frac{1}{3} - \frac{2}{3})\mu(\Lambda^0) + [\frac{2}{3}]\frac{1}{3}\mu(\Lambda^0) \\ &= \frac{1}{3}\mu(\Lambda^0) = -0.81 \end{aligned} \quad (2.17)$$

This model works very well for most of the baryons as exhibited in Table II under the column "Lipkin." Whether serious physical models should be pursued in an effort to justify the above ad hoc manipulations depends to some extent on a precise measurement of $\mu(\Sigma^-)$. The experimental value $\mu(\Sigma^-) = -0.89 \pm 0.14$ from Ref. 11 is in agreement with this model.

2.2 BAG MODELS

Although the non-relativistic AQM is used with qualitative success to predict some hadronic properties, fundamental difficulties with the theory keep it from being a physically satisfying model of hadrons.⁴⁴ The MIT bag model^{44,45} is an attempt to rectify this situation. With the exception of confinement (quarks must reside within a sphere of radius R), the theory includes many of the essential features of QCD. Since the introduction of the MIT bag model in 1974, the level of additional sophistication and effort that has been put into its further development is substantial.⁴⁶

When chiral symmetry was recognized to be an important exact symmetry of QCD for massless up and down quarks, mechanisms to include it in the bag model were introduced.⁴⁷ Although there is no unique prescription for this inclusion, recent examples of bag models⁴⁸ use pion fields coupled to the surface of the bag to achieve chiral symmetry. The inclusion of these fields affects bag-model calculations of magnetic moments, which originally⁴⁴ were equivalent to those of the AQM. We will discuss two calculations of baryon magnetic moments in the context of chiral bag models.

2.2.1 Chiral Bag Models

The Lagrangian which defines the unmodified MIT bag model is

$$L(x) = [i/2 \bar{q}(x) \not{\partial} q(x) - B] \Theta_B - \frac{1}{2} \bar{q}(x) q(x) \delta_s \quad (2.18)$$

where

$q(x), \bar{q}(x)$ are quark field operators,

$$\not{\partial} = \gamma^\mu \nabla_\mu,$$

$\Theta_B = 1$ for $r \leq R$, and 0 for $r > R$,

B is the positive energy density equal to the Dirac pressure of the constituent quarks, and

δ_s is a surface delta function = $\delta(r-R)$.

Chiral symmetry is satisfied when the Lagrangian is invariant under the transformation

$$q(x) \rightarrow q(x) + \frac{1}{2} \tau \cdot \epsilon \gamma_5 q(x) \quad (2.19)$$

with τ , the Pauli (isospin) matrices and ϵ , an infinitesimal constant isovector. The above Lagrangian does not possess this invariance because of the presence of the $\bar{q}(x)q(x)$ term, as pointed out by Chodos and Thorn.⁴⁷ Since the axial-vector current A_μ is conserved inside the bag and discontinuous on the surface, chiral invariance (which demands that the total $\partial_\mu A_\mu = 0$) can be restored by including in the bag Lagrangian a term which compensates for this "surface" problem.

2.2.1.1 The Little Bag

Brown and Rho⁴⁹ propose a solution to this problem by attaching a pion field to the surface of the bag. The axial current within the bag is determined from the quarks alone; outside the bag it is carried by the pion field. The authors argue that in addition to inclusion of chiral invariance into the model, a mechanism for one-pion exchange between nucleons is introduced. Furthermore, they claim that the "pressure" exerted on the bag surface by the pion field dramatically reduces

the size of the bag to a value more consistent with the concept of a small hard nucleon core of approximate radius 0.4 - 0.5 fm; hence the name "little bag."

The baryon magnetic moments are calculated in the framework of this model by Brown, Rho, and Vento.⁵⁰ They note in particular that the pion field influences the strange (Λ, Σ, Ξ) and nonstrange (p,n) baryons differently. Since all quarks in the nucleons can couple to the pion field (pions are $q\bar{q}$ combinations of the u and d quarks), a two-body exchange operator of the form

$$\mu^{(2)} = \sum_{i \neq j} [\sigma(i) \times \sigma(j)], [\tau(i) \times \tau(j)], \quad (2.20)$$

has a non-zero expectation value. For strange baryons, $\mu^{(2)} = 0$. To the extent that the pion field consists of exchange between two different quarks (the authors calculate it to be 6/11), the magnetic-moment dependence is shown to have an "isovector" part. The remaining contribution from the pion field to the u and d quarks is folded in with the Dirac moments of the quarks into "effective" quark moments, giving an "isoscalar" contribution.

The following relations are obtained for the "effective" quark magnetic moments

$$\begin{aligned} \mu_u^{\text{eff}} &= \left[+\frac{2}{3} m_N / m_u - \frac{1}{2} \frac{6}{11} 2.356\theta \right] \mu_N \\ \mu_d^{\text{eff}} &= \left[-\frac{1}{3} m_N / m_u + \frac{1}{2} \frac{6}{11} 2.356\theta \right] \mu_N \\ \mu_s^{\text{eff}} &= \mu(\Lambda^0) = -0.61 \mu_N \end{aligned} \quad (2.21)$$

where $\theta=1$ for nucleons and 0 for strange baryons. The parameter δ is determined to be 0.4 to 0.5 and m_u is adjusted accordingly to fit the

nucleon moments. From Eq. (2.21) and the AQM relations (e.g., Eq. (2.9)) the strange-baryon magnetic moments can be calculated. For $\delta=0.4$, Brown, Rho, and Vento obtain the results listed in Table II under the heading "Little Bag" (although for the strange baryons they use $R=1$ fm). The value for $\mu(\Sigma^-)$,

$$\mu(\Sigma^-) = \frac{1}{3}\mu_d - \frac{2}{3}\mu_s = -0.84 + 0.20 = -0.64 \mu_N, \quad (2.22)$$

is significantly lower than the SU(6) result because of the implicit "quenching" of the d-quark contribution in the strange baryon compared to its contribution, say, of $\frac{1}{3}\mu_d - \frac{2}{3}\mu_u$ for the neutron.

2.2.1.2 The Cloudy Bag

In 1980, Theberge, Thomas, and Miller⁵¹ developed a different mechanism for introducing chiral symmetry in the bag Lagrangian. The method includes a pion field distinct from that proposed by Brown and Rho in two important ways. Firstly, the pion field is quantized and secondly, the resulting quantized pions are allowed to "leak" into the bag; hence the name "cloudy bag model" (CBM).

The baryon magnetic moments are calculated within the CBM approach⁵² by including the additional coupling of the photon to the current from pion loops. The three lowest-order diagrams

(2.23)

are included. No other free parameters are needed to fit the resultant quantities to experiment other than the bag radius which is taken to be $R=1$ fm. (In all the other examples discussed the magnetic moments had to be scaled to at least one of the experimental measurements.) The results are listed in Table II under the heading "CBM." We point out, in particular, the value $\mu(\Sigma^-)=-1.08$ and the overall good agreement achieved for the other baryon magnetic moments.

2.3 SUMMARY

We have presented calculations of baryon magnetic moments in the naive AQM framework and have described the results obtained from some of the more recent chiral-bag calculations. In general, the basic models provide good qualitative results. However, recent precise measurements of the strange-baryon magnetic moments have motivated sophisticated extensions and revisions of these basic models. Among these "revised" models, there exists a wide range of predictions for $\mu(\Sigma^-)$ for which the data are less precisely known.

Franklin³⁴ implicitly predicts $\mu(\Sigma^-)=-0.86$ from simple sum rules. Lipkin³⁹ and Brown et al.⁵⁰ independently advocate mechanisms which quench the nonstrange quark-moment contributions in the strange baryons and obtain results in the range $-0.54 < \mu(\Sigma^-) < -0.81$. These results are in contrast to the AQM prediction²² of -1.05 and that of -1.08 using the CBM approach⁵² Hence a new measurement of $\mu(\Sigma^-)$, the least well known of the moments shown, is very important.

Chapter III

ATOMIC PHYSICS CONSIDERATIONS

The formation and subsequent disappearance of a hadronic atom involves three coupled stages: atomic capture of the hadron, de-excitation of the atom by electromagnetic transitions, and nuclear absorption of the hadron. De-excitation x rays are the observables but each of the other stages plays a role which affects what is observed. In the discussion which follows, the emphasis will be on the relevant features of these stages as they pertain to the observation of Σ^- atomic x rays and to the analysis of the energies of these x rays for fine-structure splitting information.

As noted in Chapter I, the atomic capture of a low-energy Σ^- hyperon in a material takes place in a highly-excited state of the $\Sigma^-(Z,A)$ system. The quantized energy states for such a system can be calculated in first approximation from the Dirac equation.⁴ The energy eigenstates are described by the quantum numbers (n,j,m) where n is the principal, $j=\ell+s$ the total angular momentum, and m the magnetic quantum number of the state. The quantity ℓ represents the orbital quantum number with the allowed values $\ell=1,2,\dots,n-1$ for a given n , and the quantity s represents the spin quantum number equal to $\frac{1}{2}$ for the Σ^- hyperon. The allowed values of $j=\ell+s$ are thus $\ell \pm \frac{1}{2}$.

In the absence of an external magnetic field, no spatial direction is preferred and states of given (n,j) values are degenerate in

energy. The splitting in energy of the two states ($j=\ell\pm\frac{1}{2}$) of given n and ℓ is known as atomic fine structure. The energy levels E'_{nj} given by the Dirac equation are

$$E'_{nj} = \left[m \left(1 + \frac{Z\alpha}{n - (j + \frac{1}{2}) + \sqrt{(j + \frac{1}{2})^2 - Z^2\alpha^2}} \right)^2 \right]^{-\frac{1}{2}} \quad (3.1)$$

where m is the reduced mass of the $\Sigma^-(Z,A)$ system. The effects of lower- and higher-order vacuum polarization, finite nuclear size, nuclear polarization, electron screening, and recoil corrections to the vacuum polarization and anomalous moment must be added to this result to produce the exact energy levels E_{nj} .

The magnetic moment of the Σ^- hyperon can be decomposed into two parts as given in Eq. (1.4), and Eq. (1.5) contains the essential dependence of the splitting in energy on the magnetic moment. The following procedure was used to determine the magnetic moment from the present data. For a transition from $(n,\ell) \rightarrow (n',\ell')$, the Dirac energies of the states were calculated. Non-magnetic-moment dependent corrections were then applied to obtain the exact energies of the states with g_1 taken as zero. The data were then fitted in small steps of g_1 corresponding to a wide range in values of the magnetic moment. At each value of g_1 , the anomalous-moment dependent contributions were added to the energies of the states to give the final corrected levels. The result for $\mu(\Sigma^-)$ reported in this work corresponds to the value of g_1 that minimized the χ^2 of the fit.

Corrections to the Dirac energy levels were calculated in two ways. First, a computer program⁵³ was used in which the energies of

states were calculated from a second-order perturbative expansion of the Dirac equation. The program included contributions from vacuum polarization to order $\alpha(Z\alpha)^7$ and finite nuclear size, following Bloomquist.⁵⁴ Furthermore, electron screening contributions, following Vogel;⁵⁵ and nuclear polarization effects, following Ericson and Hufner⁵⁶ were included. Second, an algorithm of a different philosophy incorporated into a computer code written by Borie and Rinker,⁵⁷ was used. They solved the energy-level eigenvalue problem numerically including relativistic (recoil) corrections and lowest-order vacuum polarization as part of the wave function. Higher-order effects were calculated with perturbation theory. Energy-level corrections obtained from the two methods agreed to within 3 eV for all effects except the contribution "per unit" anomalous moment. In the worst case, a difference of 3 eV out of 1011 eV existed in the the correlation of a given $\mu(\Sigma^-)$ with that of a corresponding separation of fine-structure components. This ambiguity was below the sensitivity of the measurements. A more complete discussion of corrections of this type is given by Roberts.⁵⁸

3.1 CHOICE OF TARGETS (Z,A)

The choice of targets used to study Σ^- x-ray fine-structure was guided by Eq. (1.5). The difference in energy between the $\ell + \frac{1}{2}$ to $\ell' + \frac{1}{2}$ transitions and the $\ell - \frac{1}{2}$ to $\ell' - \frac{1}{2}$ transitions from a state n to a state n' increases as Z^4 , so that high Z is preferable. For a given Z , transitions between states of low n were desired since the splitting of the doublet components decreases approximately as $1/n^5$. The strong-interaction absorption of the Σ^- hyperon by the nucleus pre-

cludes observation of the lowest transitions. For a given n , the absorption increases for increasing Z . The choice of the Z of the target took into account all these factors.

Within these basic constraints, there were several other considerations. The target nucleus could contain no static electric-quadrupole moment since the induced splitting in energy of the states caused by this property would complicate the analysis for fine-structure splitting. Similarly, targets having low-lying (≤ 200 keV) excited states were not used because of the probability of inducing dynamic quadrupole moments in the nuclei of these targets. Background-inducing processes from γ -ray de-excitation of excited nuclear states of the target or from those fragments which remain after absorption of π^- , K^- , or Σ^- were difficult to anticipate. Therefore, the candidate target materials were tested by exposing them to a π^- beam and recording the γ -ray background spectrum in the region of Σ^- x-ray transition energies. Although the results of these tests did not guarantee the absence of contaminants under Σ^- x-ray peaks, they revealed the background structure from pion-induced interactions.

Several transitions were nearly degenerate and targets in which any of these transitions were primary candidates for analysis were not used. These transitions ($n-n'$) were:

- (6-5) and (8-6)
- (7-6) and (11-8)
- (10-9) and (13-11).

Finally, the data from previous Σ^- exotic atom experiments,¹⁶ where Pt, Pb, and U targets were used, indicated the presence of severe background contaminants near the $\Sigma^-U(12-11)$ and $\Sigma^-Pt(11-10)$ transition energies.

The targets used and the associated transitions analyzed in this work are listed in Table III. Also included are the approximate energies of the transitions, the corresponding fine-structure splittings of the components for two values of $\mu(\Sigma^-)$, and the typical detector resolution R at the given transition energy. The quantity S/R is a "figure-of-merit" corresponding to the splitting-to-resolution ratio. The simple quark-model value of $\mu(\Sigma^-) = -1.05 \mu_N$ and the previous exotic-atom experiment result of $\mu(\Sigma^-) = -1.40 \mu_N$ were used as representative values from which to compute the splittings.

TABLE III

Targets and Transitions Analyzed in the Experiment

Transition	Energy (keV)	R (eV)	$-1.05 \mu_N$		$-1.40 \mu_N$	
			S (eV)	S/R	S (eV)	S/R
$\Sigma^-Pb(11-10)$	373	1058	558	0.53	954	0.90
$\Sigma^-Pb(12-11)$	283	951	319	0.34	492	0.52
$\Sigma^-W(11-10)$	303	974	374	0.38	575	0.59

3.2 ATOMIC CAPTURE AND CASCADE

When brought to rest in the target (Z,A) , the Σ^- hyperon can be captured into a high n state of the exotic-atom system. For a given n , there are $2\ell + 1$ possible angular momentum states available. The initial population of these states as well as the initial n determines the ratio of the intensity of "circular" ($\ell=n-1$) to "non-circular" ($\ell < n-1$) radiative transitions between subsequent low- n states.

The cascade of the Σ^- hyperon to lower-energy levels following atomic capture progresses initially by Auger transitions dominantly for $\Delta\ell = -1$ and Δn corresponding to differences in energy large enough to cause ejection of an atomic electron. At high n values, the energy difference between adjacent levels is small, so that only a large Δn can provide the energy for an Auger transition. The net effect of many such transitions is to weight the distribution of (n,ℓ) toward high ℓ for a given n , *i.e.*, to circularize the distribution.

Eventually, the cascade reaches a state with a classical Bohr radius close to that of the $1s$ electron. For an atomic system with reduced mass m , this radius is given by

$$r_n = \frac{\hbar^2}{me^2} \frac{n^2}{Z}. \quad (3.2)$$

For $r_n(\Sigma^-) \simeq r_1(e^-)$, n is about 48.

Radiative transitions dominate the cascade for smaller n because there the overlap of the wave function of the Σ^- with that of the atomic electrons is small. The pertinent selection rule is $\Delta\ell = \pm 1$ and generally $\Delta n = -1$. However, as in the Auger case, transitions of magnitude $\Delta n > 1$ are allowed and these transitions, too, tend to circularize the population of states.

Strong-interaction (SI) absorption competes with the electromagnetic (EM) cascade in depleting the $n=10$ states for both Σ^- Pb and Σ^- W atoms. The $n=10$ to $n'=9$ radiative transitions for these atoms are noticeably reduced in intensity compared with those of the corresponding (11-10) transitions. In addition, for highly non-circular orbits (low ℓ), the SI absorption depletes states of even higher values of n than 10 because these states overlap the nucleus significantly.

3.2.1 Non-Circular Transitions

The measurement of the magnetic moment of the Σ^- hyperon is based on a determination of the splitting in circular transitions caused by atomic fine structure. However, the effects of competing non-circular transitions (of very nearly the same energy) must be included.

In Fig. 1, selected EM transitions are shown, with fine-structure splittings suppressed. The α_0 is the circular and $\alpha_1, \alpha_2, \alpha_3, \dots$ are the first, second, third, ... non-circular transitions from the $n=15$ to $n=14$ states. The $\eta_1, \eta_2, \eta_3, \dots$ are $\Delta n=-2$, (15-13) transitions which also deplete the $(n, \ell < n-1)$ states. A measured (15-14) "peak" in a Σ^- x-ray spectrum actually consists of the sum of the α_i transitions, each distinct in energy, but not resolved by the spectroscopy system. In addition, transitions with $\Delta \ell = +1$, which are not shown in the figure, are included in the peak shape. The intensity of each α_i transition decreases rapidly with increasing i and only the first few need be considered. A (15-13) "peak", consists of the η_i s and is resolved in

energy from the (15-14) "peak." The relative-intensity ratio of these two composite peaks is therefore a measurable quantity. Because the η_i transitions occur from the same initial (n, ℓ) as the α_i and the branching ratios α_i/η_i are known from EM dipole matrix elements, this intensity ratio directly determines the amount of non-circular contribution to the (15-14) peak shape. It follows that measurements of the intensities of other $\Delta n = -2$ transitions determine the percentage of the non-circular contributions contained in other $\Delta n = -1$ "peaks."

3.2.2 Spin-up to Spin-down Intensity Ratio

Fig. 2 shows the fine-structure components of an (11-10) transition, including the circular and first, or primary, non-circular components. The intensity ratio s_1/s_0 is $\ll 1$; hence no other non-circular transitions contribute. The a_i represent the $\ell + \frac{1}{2}$ to $\ell' + \frac{1}{2}$ transitions (spin-up to spin-up), the b_i represent the $\ell - \frac{1}{2}$ to $\ell' + \frac{1}{2}$ transitions (spin flip), and the c_i represent the $\ell - \frac{1}{2}$ to $\ell' - \frac{1}{2}$ transitions (spin-down to spin-down). The intensity of the transitions denoted by b_i is very small since $\Delta j = 0$ and can be ignored. The ratios of the intensities of the $\ell + \frac{1}{2}$ to $\ell' + \frac{1}{2}$ transitions to the $\ell - \frac{1}{2}$ to $\ell' - \frac{1}{2}$ transitions have been calculated assuming an initial statistical population of the spin states.⁵⁹ The validity of this assumption has been demonstrated in muonic atoms, where, even in the 2p-1s transitions, the statistical population of spin states is preserved.⁶⁰ The ratios of interest for the Σ^- atomic transitions studied here are listed in Table IV. Since they differ from unity, the "ordering" of the fine-structure components can in principle be determined and a potential ambiguity in the contribution of the anomalous moment to the total magnetic moment avoided.

TABLE IV

Spin-up to Spin-down Intensity Ratios

Transition ($n-n'$)	Circular a:c	First Non-Circular a:c
(13-12)	1.087	1.096
(12-11)	1.096	1.106
(11-10)	1.106	1.119

Chapter IV
EXPERIMENTAL METHOD

4.1 INTRODUCTION

The experimental equipment, electronic circuitry, and data acquisition system were designed to detect the formation of Σ^- exotic atoms and to record the x-ray spectra resulting from their de-excitation. To form a large sample of these atoms, a copious source of low energy Σ^- must be produced. Owing to the short lifetime of the Σ^- ($\tau = 0.148$ nsec), the development of a low-energy beam of these particles is not feasible. Instead, they can be produced through a secondary reaction using a negative kaon beam. Ziemska⁶¹ has calculated the production fraction of Σ^- when K^- are captured by heavy nuclei such as Pb or W. The result of her calculation indicates a 5% yield of Σ^- which escape such nuclei after K^- capture. The Σ^- can then undergo atomic capture by a neighboring nucleus after losing kinetic energy through ionization. In previous exotic-atom experiments,^{16,18} the yield ratio of Σ^- x rays to K^- x rays in the spectra obtained was consistent with this calculated Σ^- production rate. The signal-to-noise (S/N) of Σ^- x-ray peaks (ratio of doublet peak height to background) was typically 1:5. Extracting fine-structure splitting information from these x-ray peaks involved a sensitive "line-shape" analysis because the splittings were less than the instrumental resolution. Background contaminant γ rays under or near low S/N Σ^- x-ray peaks

were therefore potentially troublesome. Indeed, some candidate transitions could not be included in the analysis for $\mu(\Sigma^-)$ because of severe background problems.⁶² A combined value of $\mu(\Sigma^-) = -1.41 \pm 0.25 \mu_N$ was obtained for the two 1973 BNL experiments and was based primarily on the measurement of the fine-structure splitting of the Σ^- Pb(12-11) transition.

In an effort to overcome the two limiting factors in such an experiment (low production of Σ^- and poor x-ray S/N), we have developed a new technique for enhanced production and identification of low-energy Σ^- . The method was based on the favorable branching ratio of 44% for Σ^- production through the reaction



when K^- were brought to rest in liquid hydrogen (LH_2). The Σ^- so produced had a kinetic energy of 12.5 MeV and were readily stopped in thin target plates immersed in LH_2 . The energetic (82.6 MeV) π^+ were detected exterior to the target and served to tag the production of Σ^- atoms. In addition to this new technique, an advanced spectroscopy and data acquisition system permitted the accumulation of x-ray spectra in a higher-intensity K^- beam while maintaining excellent instrumental resolution.

4.2 K⁻ BEAM

The experiment was performed at the Brookhaven National Laboratory Alternating Gradient Synchrotron (AGS) using the Low Energy Separated Beam line C (LESB I). The experimental apparatus was placed in the C4 extension of this beam line. A plan view of LESB I is shown in Fig. 3. The π^- , K^- , and \bar{p} produced when the 28 GeV slow extracted proton beam impinged axially upon a thin platinum rod placed at Target Station C were focused by a series of magnetic lenses (Q1-Q6 and D1-D3) into an oval spot of approximately 4.5×5.5 cm² at the final focus. An electrostatic separator, operated at a potential of 750 kV, and a crossed magnetic field deflected unwanted pions and muons vertically downward while leaving kaons undeflected. Momentum slits and mass slits provided additional means of collimating the beam. The momentum slits were left in the "open" position throughout the data runs. However the mass slit, located at a vertical focus following the separator, was varied to maintain a steady beam rate and a small final-focus profile. A typical mass slit opening was 1.5 mm. The magnets were tuned to transport 680 MeV/c negative particles through the beam line with a momentum dispersion of $\pm 2\%$. The beam line elements, their settings within the beam line control system, and the equivalent "physical" values of these settings are listed in Table V.

The average flux of K^- measured one meter downstream of Q6 was approximately 60,000 per beam burst when 4.0×10^{12} protons were focused on the C Target Station. The AGS beam cycle was 2.8 seconds when operated in the slow extracted mode consisting of a 0.8-sec burst of continuous "flat-top" beam followed by a 2.0-sec period of no beam. These

TABLE V

C4 Beam Line Elements and Settings for 680 MeV/c

ID	Element	Set Point	Current/Opening
D01	Dipole	2000	1999. A
Q01	Quadrupole	1826	1826. A
Q02	Quadrupole	470	351.8 A
D02	Dipole	1950	1217.0 A
B01	Separator Dipole	1680	638.7 A
Q03	Quadrupole	2568	1598.0 A
Q04	Quadrupole	1568	975. A
K01	Upstream Jaw	2440	OPEN
K02	Mass Slit Opening	2245	1.5 mm
K03	Mass Slit Rotation	2746	64° from beam
K04	Mass Slit Height	2050	-1.0 mm
K05	Downstream Jaw	2128	OPEN
Q05	Quadrupole	1888	889.2 A
D03	Dipole	1476	1477. A
Q06	Quadrupole	1448	1885. A

DATE: 22-APR-82

periods are hereafter referred to as beam-on and beam-off. The LESB I channel is described in more detail by Fox.⁶³

4.3 EXPERIMENTAL ARRANGEMENT AND GEOMETRY

A plan view of the experimental apparatus is shown in Fig. 4. The description of the equipment and associated electronics is broken down into four functional categories: kaon stopping identification, hydrogen target, π^+ spectrometers, and x-ray spectroscopy.

4.3.1 Kaon Stop Identification

Negative pions and kaons emerged from the last beam quadrupole magnet in the approximate ratio of 9:1 and were focused on the target T, located 1.3 meters farther downstream. A Fitch-type⁶⁴ Cherenkov counter, \bar{C} , was placed downstream of beam-defining plastic scintillators S1 and S2 and a coincidence signal from at least four of the six photomultiplier tubes viewing a plastic radiator within \bar{C} was used to distinguish kaons from pions. A time-of-flight (TOF) circuit was employed in setting up the Cherenkov counter system and to check its efficiency for kaon identification and pion (or muon) rejection. The scintillator of counter S4 was viewed by two photomultiplier tubes and a coincidence of these elements, using constant fraction discriminators and a mean timer, formed the definition of the start time for the TOF circuit and for all K^- induced events. The TOF "stop" signal was set with a delayed signal from counter Z, which was located just downstream of the mass slit (Fig. 3). A 3.4 nsec difference existed in the time required for 680 MeV/c π^- and K^- to travel this path length, a time interval readily resolved by the electronics circuitry. This time difference was digitized in a CAMAC time-to-digital converter (TDC) and a plot of TOF for beam particles satisfying the coincidence gating requirement $S1 \cdot S2 \cdot \bar{C} \cdot S3 \cdot S4 \cdot S5$ is shown in Fig. 5. Evident in the figure is the clear separation of π^- and K^- as well as a $\sim 1:15$ area ratio of π^-/K^- . Coupled with the fact that there are 9:1 π^-/K^- in the incident separated beam (given by $S1 \cdot S2 / S1 \cdot S2 \cdot \bar{C}$ ratio), the plot indicates a rejection factor of 135:1 for unwanted π^- by the counter \bar{C} .

A hodoscope array H positioned just upstream of counter S4 provided beam-spot size information which greatly aided in tuning the beam. Four horizontal and three vertical strips of 0.32 cm thick scintillator were overlapped in such a manner as to provide five horizontal divisions (X) and seven vertical divisions (Y) of a 10 x 10 cm² area. Signals from any of the seven phototubes viewing these strips were discriminated and routed to a CAMAC bit register. Figures 6a and 6b show reconstructed X and Y profiles of incoming K⁻ satisfying the above gating requirement.

A Cu block moderator, consisting of 10 x 10 cm² pieces and totaling 14 cm thickness, was positioned directly upstream of the hodoscope to optimize the number of K⁻ which stopped in the target. A plastic scintillator veto box V₁ framing the Cu degrader was designed to trigger on fragments from K⁻ interactions within the moderator. Approximately 25% of K⁻ impinging on the moderator exited and the mean momentum at the target face was calculated to be 50 MeV/c. This latter information was obtained from a Monte Carlo study of the K⁻ beam incident in the geometry used.⁶⁵

The pulse heights from scintillators S4 and S5 were digitized to give dE/dX information of beam particles. This served further to distinguish stopping K⁻ from beam π⁻ or forward-produced nuclear interaction fragments. Fig. 7 displays the pulse height in counter S5 triggered by a S1·S2·C^Y·S3·S4·S5 coincidence. A separation of π⁻ and K⁻ is evident since the energy deposited by a minimum ionizing π⁻ is much less than that of a low-energy K⁻. A discriminator threshold of 300 mV, indicated in the figure, was imposed on S5, thereby eliminating much of the remaining ambiguity in identifying low-energy K⁻ entering T.

Veto counter V_2 , downstream of T, provided a final check on the stopping K^- signature. The K^- stop signature used was therefore defined as

$$KS = S1 \cdot S2 \cdot \bar{C} \cdot S3 \cdot S4 \cdot S5 (300 \text{ mV}) \cdot \bar{V}_1 \cdot \bar{V}_2$$

Beam counter dimensions are listed in Table VI and a complete logic diagram for the beam telescope is shown in Fig. 8. Logic signals formed directly adjacent to the experimental area are represented within the dashed box in the figure. The remainder of the electronic circuitry was placed in a trailer containing the computer and associated data-acquisition elements.

TABLE VI

Beam Telescope Counters

Scintillation Counters	Dimensions (cm)
S1	10.2 x 12.7 x 0.635
S2	10.2 x 12.7 x 0.635
S3	10.2 x 10.2 x 0.635
S4	10.2 x 10.2 x 0.635
S5	10.2 x 10.2 x 1.270
V_1 (4 sides)	10.2 x 15.2 x 0.635
V_2	30.5 x 30.5 x 0.635
Cerenkov Counter	
\bar{C}	8.9 diameter x 1.27 thick (lucite)

4.3.2 Hydrogen Target

The target T consisted of a bath of LH_2 in which were immersed 19 Pb (or W) metal foils. This assembly was enclosed in an Al housing. A front and a side view of the target are shown in Fig. 9. The foils were spaced 0.46 cm apart and each was 15.0 cm in length. The Pb target foils were 0.035 cm thick and the W target foils were 0.020 cm thick. In both targets, the foils were of varying heights with the tallest (10.5 cm), placed in the center and the shortest (6.5 cm) at the sides. This array resulted in both optimum transmission efficiency of x rays through the target and distribution of K^- stops within the LH_2 -foil layers. Optimization of the foil separations, thicknesses, lengths, and heights were studied with the aid of a Monte-Carlo program. Some of the many factors which led to the final design included: the total amount of LH_2 to foil ratio in order to enhance K^- stops in hydrogen, the spacing of foils to minimize losses due to Σ^- decay between plates, and the thickness of foils to maximize stopped Σ^- and minimize the absorption of x rays in the plates and target housing.

4.3.3 π^+ Spectrometers

An essential component in this experiment was the π^+ spectrometer system used to tag the production of Σ^- in LH_2 . Monoenergetic π^+ emitted in the reaction $\text{K}^- \text{p} \rightarrow \Sigma^- \pi^+$ emerged from the target vacuum jacket with an energy between 60 and 82 MeV, depending upon the number of foils traversed. A number of geometric and physical considerations dictated the final design of the system to identify these π^+ .

Since K^- interacted at rest with protons in the hydrogen bath, the Σ^- and π^+ emerged colinear, at 180° . The Pb (or W) target plates within the LH_2 were placed vertically with their planes parallel to the beam line. Therefore, the Σ^- most likely to intercept a target foil before decaying were those which traveled normally or nearly normally to the plates. The π^+ which signalled production of these particular Σ^- thus emerged from the sides of the target. Extensive Monte-Carlo studies showed that detection of those Σ^- intercepted by plates was optimum for π^+ which emerged within a 30° cone from the sides of the target. In satisfying these conditions, each spectrometer telescope subtended a fractional solid angle of ~ 0.09 when counter 3A was positioned 36 cm from the beam-center line.

The ambient delayed background following a K^- stop in a simulated target of CH_2 and Pb was measured by us in a background test run in the adjacent C2 beam line in March 1980. In that test, the technique of detecting delayed positrons from muon decay following π^+ stops in a range telescope array was tested and deemed feasible. The mean lifetime for the decay sequence $\pi^+ \rightarrow \mu^+ \rightarrow e^+$ is approximately 2.2 μsec . An 8 μsec period following π^+ arrival in a counter (sufficiently long to observe 97% of the decay positrons) was chosen for the gating time.

Two plastic scintillation counter arrays were used in the stopping π^+ and decay e^+ signatures, each consisting of three $45.7 \times 45.7 \times 2.54$ cm³ counters (3A,3B,3C) placed between two $45.7 \times 45.7 \times 0.635$ cm³ counters (2 and 4). Aluminum plates of the same area were used to optimize the number of the desired π^+ that stopped in 3A, 3B, or 3C. One $25.4 \times 25.4 \times 0.318$ cm³ plastic scintillator (1) was

mounted on either side of the target and acted as a solid-angle defining counter for the respective spectrometer array. The two spectrometer arms were thus identical (π_L and π_R in Fig. 4) and in the following we discuss the logic for the left (L) side only.

A pion stop was defined to be any of the following fast coincidence signals:

$$\begin{aligned} L\pi_A &= KS \cdot L1 \cdot L2 \cdot L3A \cdot \overline{L3B} \\ L\pi_B &= KS \cdot L1 \cdot L2 \cdot L3A \cdot L3B \cdot \overline{L3C} \\ L\pi_C &= KS \cdot L1 \cdot L2 \cdot L3A \cdot L3B \cdot L3C \cdot \overline{L4} \end{aligned}$$

Each of these pion-stop signals permitted three distinct patterns of delayed positron detection. The patterns recognized as delayed positron tags were:

- 1) A delayed signal in the counter in which the π stopped, a coincident signal in an adjacent counter, and no signal in the opposite adjacent counter. (For example, a delayed $\overline{L3A} \cdot L3B \cdot L3C$ following a $L\pi_B$)
- 2) No delayed signal in the counter in which the π stopped but a coincidence signal in the next two adjacent counters (For example, a delayed $\overline{L3B} \cdot L3C \cdot L4$ following a $L\pi_B$)
- 3) A delayed signal in the counter in which the π stopped which exceeded a second high-level discriminator threshold. This signal pattern would account for decay e^+ directed parallel to the spectrometer plane.

A logic diagram for one of the spectrometers is shown in Fig. 10.

A survey of the reactions in which energetic pions are emitted when a K^- is captured in LH_2 or in a heavy nucleus (Z) was used to optimize spectrometer system variables (*i.e.* Al degrader thickness, discriminator thresholds, gating times, solid angle). Table VII is a list of the most relevant reactions, along with the energy of the π^+ or π^- at

the production point within T. Included in the table are the branching ratios for particular reactions, the absolute rate expected per K^- stop in T and the net rate per K^- stop of π^+ in the range 60-82 MeV. The total thickness of counter array L3 (R3) was such that π^+ in this energy range would stop after being slowed down with an appropriate amount of moderator. This optimum amount of degrader was determined by measuring the number of delayed e^+ following stops in π_B as a function of moderator thickness. Monte-Carlo studies showed that examining any other scaled quantity such as total π stops or total e^+ triggers would lead to the inclusion of too many false triggers from Σ^+ decays. Aluminum plates totalling 4.13 cm in thickness were used in the data runs. Fig. 11 shows a typical time histogram of e^+ triggers following π^+ stops which has been fitted to the function $Ae^{-t/\tau} + B$. The fitted value 2.26 ± 0.10 μ sec for τ is in good agreement with the lifetime of the positive muon.⁶⁶ The time between a K^- stop in T and a decay positron, together with the pattern of the decay and the amount of energy deposited by the e^+ in the counter in which its associated π^+ stopped, were all recorded on magnetic tape for each "tagged" event. An estimate of the efficiency ϵ for identifying those π^+ produced in Reaction (4.1) in either of the two spectrometer arms was

$$\begin{aligned} \epsilon(\pi^+ \rightarrow e^+) &= (\Omega_{\pi^+ \text{ stop}})(\% \pi^+ \text{ stop in L/R3})(\text{electronic efficiency}) \\ &= (0.18)(0.90)(0.91) = 0.147. \end{aligned}$$

TABLE VII

Reactions Producing Energetic Charged Pions Following K^- Stops in Target T

REACTIONS PRODUCING	E_π (MeV)	BR*	Rate per K^- Stop	60-82 MeV π^+ per K^- Stop
Positive Pions				
$K^-p \rightarrow \Sigma^- \pi^+$	82.67	0.44	BR x af = 0.159	0.159
$K^-Z \rightarrow \Sigma^- \pi^+$	10-100	0.154	BR x bf = 0.098	0.024
$K^-p \rightarrow \pi^- \Sigma^+ \rightarrow n\pi^+$	92.2	0.20	BR x adf = 0.034	0.014
$K^-Z \rightarrow \pi^- \Sigma^+ \rightarrow n\pi^+$	92.2	0.27	BR x bcdf = 0.041	0.017
Negative Pions				
$K^-p \rightarrow \Sigma^+ \pi^-$	89.2	0.20	BR x af = 0.065	-----
$K^-Z \rightarrow \Sigma^+ \pi^-$	10-100	0.27	BR x bf = 0.155	-----
$K^-p \rightarrow \pi^+ \Sigma^- \rightarrow n\pi^-$	98.0	0.44	BR x aegf = 0.047	-----
$K^-Z \rightarrow \pi^+ \Sigma^- \rightarrow n\pi^-$	98.0	0.154	BR x bafh = 0.023	-----

Factors: a) 36% K^- stop in LH_2 (p) — Monte Carlo result
 b) 64% K^- stop in foil (Z) — Monte Carlo result
 c) 50% of Σ created by K^-Z capture are reabsorbed — estimate
 d) 48% b.r. ($\Sigma^+ \rightarrow n\pi^+$)
 e) 33% Σ^- decay before reaching foil — Monte Carlo result
 f) 90% survive 4.1 cm Al degrader — estimate
 g) 100% b.r. ($\Sigma^- \rightarrow n\pi^-$)
 h) 50% Σ^- decay before atomic or nuclear capture — Monte Carlo
 * Branching Ratio

4.3.4 X-ray Spectroscopy

The x-ray spectroscopy system was designed to detect photons in the energy range 100-700 keV with good efficiency and resolution. For the Σ^- exotic atoms studied here, the splitting of fine-structure components was less than 2% of the actual transition energies. Therefore a premium was placed on designing a system with optimum resolution. Systems involving bent-crystal spectrometers provide the best

available resolution at such energies; however their intrinsic efficiency would be prohibitively low for experiments involving Σ^- atoms. Instead, a solid-state detector system was utilized. This system consisted of three coaxial intrinsic Ge crystals all housed in a single upward-oriented liquid-nitrogen coldfinger vessel. The detectors and housing are shown in Fig. 12. The cryostat was positioned below T such that the top faces of the crystals were 12 cm from the beam-center line. The typical resolution of these detectors was 900-1100 eV in the region of Σ^- x-ray energies with an absolute photopeak efficiency of about 20% (both parameters being dependent on specific crystal characteristics and on the energy at which they are evaluated). The detectors and their associated electronics were supplied by a collaborative effort of Lawrence Berkeley Laboratory and EG&G-Ortec. Intrinsic n-type Ge was used for each crystal rather than the more common p-type. This permitted a reverse electrode configuration of the high voltage. Detectors of this type and of this electronic configuration have a demonstrated 28 times greater resistance to neutron damage.⁶⁷ Specifications for the three detector crystals are listed in Table VIII.

TABLE VIII

Detector Specifications

Detector	Serial Number	Diameter (mm)	Length (mm)	Operating Bias (Volt)
A	701a	47	26	-2600
B	701b	47	26	-3600
C	708c	57	26	-4000

The electronic configuration of a solid-state photon detector is similar to that of a back-biased diode. In an n-type detector, the outer wall of the crystal is ion-implanted to form a p-type layer and the center is drilled to allow a metallic contact to be made to the n-type layer. A bias is applied between the central contact and the outer layer, thus forming a cylindrically symmetric electric field within the crystal. When a photon is absorbed in the crystal, electron-hole pairs are produced and then swept by the field to the respective electrodes of opposite potentials. In the reverse electrode (n-type) detectors used here, the negative potential is applied to the outer p-layer. Holes, which are subject to trapping from radiation-induced dislocations within the crystals, are therefore collected at the outer layer. Since hole-trapping effects are the main cause of degraded detector performance, this electronic configuration minimizes such effects, *i.e.*, holes produced where most of the interactions in the crystal occur have the shortest path for collection. The inner contact of the detector is joined to the gate of a cooled field effect transistor (FET). The current induced by the charge collected predominantly from an "event" within the crystal controls the output current of the FET, the signal of which in turn is fed to the input of a standard preamplifier circuit. A nominal "leakage current" exists between detector anode and cathode which produces a slowly rising ramp voltage at the preamplifier output because of the absence of a bleeder resistor to deplete the buildup of charge at the FET gate. Each event within the crystal also adds to the charge buildup and hence the ramp voltage. When the output of the preamplifier exceeds two volts (an overload threshold), the charge must be drained.

This is accomplished in the present system by having a low-capacity, low-noise reset transistor clamp the gate input of the FET when the overload threshold within the amplifier is reached. Energy-dependent efficiency is avoided by actually firing the reset after the pulse which triggered the threshold is processed. The two-volt threshold is set at half the true system overload level, thereby allowing the full processing of any 0-2 volt pulse at any point in the cycle (except during a reset). For low-energy photon detection, a reset occurs after many pulses have been collected. A charged particle traveling through the crystal or a neutron-scattered event can deposit enough energy to exceed at once the overload condition and force an immediate reset. For applications involving particle beams, a fast reset system similar to the one employed here,⁶⁸ is essential.

The outputs from the preamplifiers were fed to spectroscopy amplifiers where pulse-shaping circuitry generated a flat-topped stretched pulse whose voltage was proportional to the amount of energy deposited in the crystals. A nine- μ sec peaking circuit built into the amplifiers indicated the time required for the fast event to be processed into a voltage level. "Valid-out" logic signals, generated within the amplifiers when pulse-pileup and overload conditions were not exceeded, were used as triggers to gate the ADC digitizing the amplifier signal. The ADCs were strobed to begin conversion of the input DC level, independent of voltage, upon arrival of the center of the stretched pulse. In an effort to eliminate possible ground-loop problems in each of the amplifier-ADC systems, the ground reference of the linear section of each ADC was tied to that of its associated amplifier by their common

signal cable ground. The detector array and preamplifiers, together with the amplifiers and ADCs, were housed in thermally controlled, insulated enclosures to minimize pulse-height drifts within the linear sections of the electronics. The enclosure containing the detectors and pre-amplifiers was positioned directly under the target. A second enclosure containing the amplifiers, ADCs, and fast-slow timing electronics, was placed immediately outside the experimental area so that 8-m cables were long enough to make necessary connections between the thermally stable environments. Only digital information was sent the longer distance (23 m) to the computer trailer, thereby avoiding additional noise pick-up problems in the linear signals.

The preamplifier output signals were split at the input to the spectroscopy amplifiers and fed to timing pickoff circuits consisting of timing filter amplifiers (TFA) and constant fraction discriminators (CFD). Logic outputs from the CFDs, indicating an event in a detector, were fed into the trailer where coincidences with a K^- stop (KS) signature, a beam-on gate, or a beam-off gate defined particular events. If such an event was to be processed by the computer (see discussion below on data acquisition), a gate signal for the particular detector which fired was sent from the trailer back to the ADC gating logic in the ADC hut. The time difference between KS and the CFD output was recorded for all KS-induced events. A histogram of $KS \cdot \gamma(A)$ timing shown in Fig. 13 indicates a very good time resolution of approximately 10 nsec (full-width at half-maximum) for events associated with kaons stopping in T. Electronic block diagrams for the linear/time-pickoff configurations and the γ -event coincidences are shown in Figs. 14 and 15, respectively.

The principal electronic modules used in the x-ray spectroscopy system are listed in Table IX.

TABLE IX
Spectroscopy System Electronic Modules

Module	Manufacturer	Model	Mode/Type
preamplifier	LBL	21X5911 P-1	transistor reset
pulser/HV bias	LBL	21X3331 P-1	negative bias
amplifier	LBL	11X8481 P-5	9 μ sec peaking/bias amp x 1
ADC	LeCroy	3511	DC Sample-Strobe/8000 ch
TFA	Ortec	454	200 nsec diff/int OUT
CFD	Ortec	473a	constant fraction/Ge(Li)

4.4 DATA ACQUISITION

4.4.1 Events

The individual events of this experiment consisted of the energy measured in a Ge detector and a large amount of other information characteristic of the event. Two main categories of events existed: those induced by K^- stops (KS) in T and those induced by detector calibration γ rays.

The principal KS-induced event types and their associated electronic triggers are listed in Table X in the priority order with which they were sorted by the computer. For events labeled MULTIPLE, no selective reading of CAMAC modules was performed; all CAMAC units were read and written to tape. For TAGGED, CLEAN and RAW events, only those data words associated with the detector in which the event occurred were read and saved.

TABLE X
Principal KS-Induced Events

<u>Event Name</u>	<u>Trigger</u>	<u>Recorded Words</u>
MULTIPLE	KS \cdot ($\geq 2 \gamma$) KS \cdot ($\geq 2 \pi$) \cdot γ	All CAMAC Words
TAGGED	KS \cdot γ \cdot π^+ \cdot e $^+$	1) Event Header 2) Detector Energy 3) Hodoscope Pattern 4) KS \cdot γ Time 5) dE/dX S4 (A+B) 6) dE/dX S5 7) Kaon TOF 8) e $^+$ Decay Pattern 9) KS \rightarrow e $^+$ Time 10) e $^+$ Energy
CLEAN	KS \cdot γ \cdot π^\pm	1-7 Above
RAW	KS \cdot γ	1-7 Above

Detector calibration events were accumulated during beam-on spill time as well as during beam-off times. Weak radioactive sources ($\sim 1 \mu\text{Ci}$) emitting γ rays of well-known energies were placed between the target and detectors. These sources were chosen to provide detector resolution information near the energies of the Σ^- x-rays (during beam-on), and to provide information on the stability of the gain of the system (during beam-off). The radioactive sources used in the Pb and W data runs are listed in Table XI. Beam-on calibration events required the random coincidence of a γ ray from any of the sources with a 1.0 μsec gate started by the coincidence

$$[\text{AGS-on}] \cdot S1 \cdot S2 \cdot S3 \cdot S4 \cdot S5 \cdot V_1,$$

primarily the signature of a π^- entering the target.

TABLE XI
Calibration Sources

Source	γ -ray Energy (keV)*	Used with Target(s)
^{57}Co	122.061 136.474	Pb, W
^{133}Ba	276.404(7) 302.858(5) 356.014(9) 383.859(9)	Pb
^{192}Ir	295.958 308.457 316.508	W
^{137}Cs	661.661(3)	Pb, W

* Ref. 69, errors of less than 1 eV not given

The γ -ray energy spectra for such events served to measure the detector response under conditions identical to those in which the x rays from the Σ^- and K^- exotic atoms were actually recorded.

During beam-off cycles, the response of the system to the 122-keV γ rays from ^{57}Co and the 662-keV γ rays from ^{137}Cs was continuously monitored and the data placed into "windowed" histograms for each detector. Computer fits to peak centroids in these histograms were made after approximately 200 beam bursts. These fits permitted continuous monitoring of system drifts. These latter histograms formed the basis of an off-line, two-point stabilization routine for data replay and were regularly recorded on tape as beam-off events throughout the data runs.

4.4.2 Computer System

The data acquisition hardware consisted of two similarly-configured PDP 11/34 centered systems — one for data acquisition and one for replay of tapes. Each system contained several RK05-type disks, a Decwriter, magnetic tape drives, a Tektronix 4010 display, and various terminals. In addition, the data acquisition system was interfaced with a microprogrammable branch driver⁷⁰ (MBD) which performed all CAMAC communication. Three CAMAC crates were connected in parallel to the MBD along a standard branch highway. Type A-1 controllers were situated in each crate. The CAMAC structure for this experiment is listed in Table XII.

TABLE XII

CAMAC Crate Composition

Crate	Modules	Function
1	WM Trigger Module Pattern Bit Register Pattern Bit Register TDC (100 nsec) Charge Sensitive ADC Pattern Bit Register Pattern Bit Register TDC (10 μ sec) Charge Sensitive ADC	LAM when fired/BUSY out Event Decoding Hodoscope Pattern KS γ time/K $^-$ TOF dE/dX (S4,S5) Le $^+$ decay pattern Re $^+$ decay pattern KS \rightarrow e $^+$ time e $^+$ energy
2	Scalers (48 in 10 units)	Scale inputs/LAM on overflow
3	Spectroscopy ADCs (3)	Energy in detectors A,B, or C

4.4.2.1 CAMAC Gating

The output of a fan-in unit for event logic signals and a BUSY level from the trigger module (TM) were put into coincidence. The coincidence generated an event gate which the MBD had to acknowledge and which strobed ADCs, started TDCs, and latched pattern units in the CAMAC crates. A LAM was set by the TM and the MBD was interrupted. When an event was completely processed (see below), care was taken to guarantee that all spectroscopy ADCs were cleared (by software) and that a logic signal generated by the TM was fanned out to the fast-clear inputs of the remaining CAMAC modules. A block diagram for the CAMAC gating is shown in Fig. 16.

4.4.2.2 Data Acquisition Software

The software used for the data acquisition system consisted of three main components: 1) an interrupt-driven MBD code to sort events, 2) a magnetic tape and MBD interface routine, and 3) an analysis program. The PDP 11/34's were run under the RSX-11M operating system.⁷¹

The MBD provided a fast and convenient means of accessing CAMAC modules and permitted a limited amount of pre-processing of data. It included direct memory access (DMA) which allowed writing to the host computer memory directly using standard UNIBUS protocol. This last feature was used extensively for tape-buffer filling, scaler transfers, and direct histogramming of energies deposited in the Ge detectors. Eight priority-ordered program "channels" were available within the MBD along with 4096 words of 16-bit memory. An "executive" program resided in the highest priority channel and governed the loading and initialization of

the other channel programs. Six of the remaining channels were utilized in the data acquisition scheme. These channels are listed below in order of priority, along with their principal functions:

- CH 6 run start-stop routine -- included all initialization of modules; at begin-run time, read in all parameters pertaining to on-line histogramming and stability windows for calibration events
- CH 5 event interrupt handler -- initialized before beginning runs, then exited only to be started by look-at-me (LAM) from trigger module, at LAM did the following:
 - a. read the event pattern unit and decoded the type of event
 - b. read all appropriate CAMAC modules for event and transferred resultant event stream to PDP tape buffer and interrupted PDP when buffer was full
 - c. histogrammed in PDP memory the Ge detector words for those histograms defined at begin-run time
 - d. maintained internal windowed histograms of beam-off events and emptied these histograms on to the tape buffer on request
- CH 4 scaler initialization -- allowed scaler useage when no run was in progress; was called as a subroutine when CH 6 was invoked
- CH 3 scaler overflow handler -- all 10 scaler units were LAM-enabled and hardwired to start this program on overflow; the program searched for the overflowed scaler and incremented a corresponding counter within its own memory; it then cleared the LAM
- CH 2 scaler-reading routine -- when called by the host computer it successively read each of 48 24-bit scalers, shifted internal counters 8 bits and added, forming two-word 32-bit integers; wrote to either of two banks in PDP memory
- CH 1 beam-off dump indicator -- initialized by external time-cued PDP program, set FLUSH PENDING flag for beam-off windowed histograms and exited.

The PDP magnetic-tape handling routine performed three important functions in its interfacing role between the analysis package and the MBD. These functions included writing "filled" event buffers to tape, delivering selective event streams to the analysis program, and beginning and ending runs.

The event analysis program consisted of a modified version of MULTI.⁷² This program was designed to be an extremely flexible routine for processing event streams. Standard event-processing commands such as histogramming of data, performing cuts on data, calculating data words with subsequent histogramming of resultant quantities, and finally generating scatter plots were supported. In addition to these, CAMAC scaler handling and histogram save and retrieval routines were developed and added. MULTI was also capable of being used to analyze data tapes with no changes in command format and was also used regularly during the runs to inspect the data.

Chapter V

TESTS OF THE SYSTEM AND ANALYSIS OF THE DATA

5.1 DATA SET CHARACTERISTICS

The data were collected during three running periods in spring 1982. A Pb-LH₂ target was used in the first two of these and a W-LH₂ target in the last. The experimental apparatus and electronics configuration were unchanged throughout the runs except for the energy window viewed by detectors A and B during the first run. All data were written to magnetic tape in event stream buffers as discussed in section 4.4.1. Histograms of the energy spectrum for each detector were formed from the replay of these tapes. Information characterizing the three runs is summarized in Table XIII.

TABLE XIII

Data Set

Run	Dates (1982)	Tapes Written	Target	Gain (eV)		Energy Window (keV)	
				A and B	C	A and B	C
1	3/16 - 4/6	90	Pb	45	90	90-450	76-750
2	4/15 - 4/30	144	Pb	90	90	76-750	76-750
3	5/10 - 5/17	79	W	90	90	76-750	76-750

5.2 TAPE REPLAY

Replay of the data tapes to form detector energy histograms was performed on the PDP 11/34 systems and utilized MULTI in playback mode. These histograms were differentiated by detector number, event type, and data cuts.

Data cuts were applied with the intention of enhancing the precision obtainable for $\mu(\Sigma^-)$. Both S/N and total number of counts in x-ray peaks could in principle be altered when a cut was made. Beam diagnostics were examined for incoming K^- identification. However, TOF and dE/dX histograms, as replayed from the tapes, showed that stopping K^- , having survived the additional requirement of a coincident γ -timing signal, were even less contaminated than those shown in Figs. 5 and 7. No further delineation between beam pions and kaons could be made from cuts on these variables. Since x rays following the atomic capture of K^- in metal foils were collected under the same conditions as the RAW Σ^- data, examination of the quality of the reconstructed K^- Pb (or W) x-ray peaks as a function of various data cuts was useful. Inspection of the S/N in the K^- x-ray region as a function of the width of the $KS\gamma$ timing windows showed no improvement over the applied hardware coincidence interval of 100 nsec. However, replay of the data as a function of K^- entrance position as determined by the hodoscope array demonstrated that the S/N of both K^- and Σ^- x-ray peaks was sensitive to this parameter. A sample of 50 tapes from run 2 was sorted into energy spectra, each associated with a different K^- entrance bin in the hodoscope. Patterns of these bins were constructed and the corresponding histograms added together, forming groups of data differentiated by

incoming K^- beam spot size and position. For each of several patterns, Monte-Carlo simulations of the doublet were made according to the measured S/N and extrapolated total areas of Σ^- x-ray transitions within these data sets. Fits to these simulated doublets were then made to determine which set resulted in the smallest error in $\mu(\Sigma^-)$. A modest "cross-shaped" cut was applied to the RAW data and yielded a S/N increase for Σ^- x-ray peaks of approximately 10% with no increase in the statistical error for $\mu(\Sigma^-)$. CLEAN-event histograms ($KS^+\gamma\pi^\pm$) contained x-ray peaks of similar S/N to those in the RAW histograms. These two event types were therefore grouped together in the analysis and are discussed below as "untagged" data. In the final replay of the data, the cross-cut on the hodoscope was applied only to the untagged set of data.

TAGGED-event triggers comprised about 1.1% of all $KS^+\gamma$ events. These events were extracted from the data tapes and formed into "pare-down" tapes. Pare-down tapes were then replayed in their entirety as a function of various cuts. Some of the additional cuts tested with these data included forming spectra as a function of both $KS \rightarrow e^+$ decay time and of decay e^+ patterns in the π^+ spectrometers. Although the Σ^- x-ray S/N improved with the inclusion of these cuts and that for the hodoscope, the precision with which $\mu(\Sigma^-)$ could be determined deteriorated due to the reduction in total number of counts in these peaks. Uncut tagged x-ray spectra showed dramatic S/N improvement for Σ^- induced lines compared to the corresponding data in the untagged spectra. Fig. 17 is a vivid example of this improvement for the Σ^- Pb(12-11) transition and also shows the suppression of the neighboring

K^- Pb(9-8) transition. No cuts were applied to the TAGGED data set shown in the figure or in any tagged histograms used in the analysis for $\mu(\Sigma^-)$. Although TAGGED triggers satisfied the electronic definitions of RAW and CLEAN events, they were not included in the untagged data set.

MULTIPLE events comprised approximately 47% of the tape volume primarily because of two factors. All CAMAC units were read for each MULTIPLE event rather than the selective subset of words read for RAW, CLEAN, TAGGED, and beam-on calibration event types. In addition, for these last four event types, each spectroscopy ADC was scanned by the MBD for a valid event in the energy window as defined in Table XIII. When an overload or underload pulse triggered the detector timing circuits, an event sequence was initiated for which no valid detector energy word existed. For these events, the Q-flag of the CAMAC crate was set FALSE when the associated ADC was read by the computer. The event was not written to tape. No such pre-sorting of events was performed for the more complex MULTIPLE events and hence many of these did not contain a valid detector energy word. Histograms were constructed from a subset of those MULTIPLE events which contained valid detector signals, and they were examined for x-ray S/N. For all detectors, K^- and Σ^- x-ray S/N were found to be more than a factor of two worse compared to the untagged data set. These MULTIPLE event data were not included in the analysis.

A final replay of the data was based on a program which guaranteed that the gain and intercept for all the histograms were the same. The following algorithm was applied for each of the tapes and for each of the histograms: untagged, tagged, and beam-on calibration.

- 1) Initialization of histogram area in PDP core for temporary playback histograms
- 2) Data-tape replayed and events sorted into core histograms
- 3) Beam-off "windowed" histogram event encountered; replay suspended
- 4) Least-squares fit to low- and high-energy "windowed" stabilization peaks for each detector determined gain and intercept for data histogrammed in core (about 200 beam-bursts)
- 5) Core histograms gain-shifted and mapped to disk histograms of pre-designated gain and intercept. Fractional counts per channel in disk histograms were allowed and proper variance of each disk bin was calculated and updated (it was not necessarily equal to the bin count in this procedure)
- 6) Core histograms cleared
- 7) Steps repeated starting at 2) until tape finished

Summed files were formed from the disk histograms for 10 sequential tapes and for the entire Pb and W runs. These files were then transferred to disk files of an IBM 370 where the rest of the analysis was completed.

Histograms of the untagged and tagged energy spectra for the Pb and W data are shown in Figs. 18-21. The data shown are the sum obtained from all three detectors.

5.3 REQUIREMENTS FOR FINE-STRUCTURE ANALYSIS

The Σ^- x-ray peaks analyzed for fine-structure splitting were considered to be composed of two circular and two primary non-circular components. Higher-order non-circular transitions (*i.e.* transitions between states of $\ell \leq n-3$) were in all cases much less than 1% in relative intensity and were not included in the function used for the peak shape. For a given value of $\mu(\Sigma^-)$, the four component lines were fixed in

energy and constituted the observed Σ x-ray peak. The differences in energy among these lines were less than the relevant instrumental resolution of the detectors. Hence a broadened structure was observed, described with the function

$$D(x) = A_0 R_0 f(x, x_0) + A_0 f(x, x_0 + \Delta_0) \\ + A_1 R_1 f(x, x_1) + A_1 f(x, x_1 + \Delta_1) \quad (5.1)$$

where the A_i are the amplitudes of the $\ell - \frac{1}{2}$ to $\ell' - \frac{1}{2}$ components, $A_i R_i$ the amplitudes of the $\ell + \frac{1}{2}$ to $\ell' + \frac{1}{2}$ components, and x_i and $x_i + \Delta_i$ the $\ell + \frac{1}{2}$ to $\ell' + \frac{1}{2}$ and the $\ell - \frac{1}{2}$ to $\ell' - \frac{1}{2}$ transition energies. In this notation, $i=0$ implies circular and $i=1$ implies the primary non-circular components. The function $f(x, x_i)$ describes the spectrometer response at energy x for photons of energy x_i that are absorbed in one of the detector crystals. The determination of $f(x, x_i)$ and of A_1/A_0 is discussed next.

5.4 DETECTOR RESOLUTION

Solid-state detectors in particle beam environments suffer resolution degradation due to accumulated neutron damage. Such effects were minimized in these experiments with the use of n-type Ge crystals having a reverse electrode electronic configuration. However, slight resolution changes were experienced by the detectors over the course of the three runs. A study of this change as a function of time assured that the data were analyzed with the proper function.

The data sets were divided into two levels: groups and sub-groups. Groups were the sets of data upon which the analysis for

$\mu(\Sigma)$ was based. Subgroups were sets of tapes for which analysis of detector resolutions was possible. A subgroup typically consisted of data obtained in about 24 hours of beam time. Beam-on histograms for each subgroup contained the calibration lines listed in Table XI. Each of these lines was fitted, using the method of least-squares,⁷³ to the function

$$G(x) = f(x, x_0) + B_0 + B_1(x-x_0) + B_2(x-x_0)^2, \quad (5.2)$$

where $f(x, x_0)$ was the Gaussian

$$f(x, x_0) = A \cdot \exp\{-(x-x_0)^2 \cdot 4 \cdot \ln 2 / (\text{FWHM})^2\}, \quad (5.3)$$

and the B_i 's the coefficients of the second-order polynomial background term. FWHM represents the full width of the response of the detector system at half the maximum of the peak amplitude. The quantity χ^2 , defined as

$$\chi^2 = \sum_{i=1}^n \frac{(G(x) - y_i)^2}{\sigma_i^2} \quad (5.4)$$

was minimized in each fit. In this notation, the sum included all histogram channels, the y_i represented the counts in the x_i th bin and the σ_i^2 represented the corresponding variances. The reduced (or normalized) χ^2 was defined to be the above quantity divided by the number of degrees of freedom ν in the fit. For data exhibiting statistical fluctuations, and fitted to an "appropriate" functional form, χ^2/ν should be distributed about 1.0. A distribution of the χ^2/ν obtained for fits to Eq. (5.2) of the data from each of the four ¹³³Ba lines from each of the Pb

subgroups is shown in Fig. 22. The plot indicates that the function $f(x, x_0)$ adequately represented the instrumental response over this energy interval for all three detectors. The stability of detector resolution as a function of time was studied by plotting FWHM vs subgroup number for each of the calibration lines which were fit. Groups of these subgroups were then constructed in which detector resolution at a given energy was not changing; (i.e., any change was much less than that which would have affected the determination of $\mu(\Sigma^-)$ within the error).

Four groups were formed for the three runs. Group R1 consisted of all the analyzable data from run 1. Many of the 90 tapes written during this run were not included in this set because they contained data accumulated during runs made for beam diagnostics, detector optimization, and beam-off stabilization studies. Run 2 was divided into two groups, R2A and R2B, consisting of the first nine and the last five subgroups, respectively. All the data from run 3 were grouped together and labeled R3.

The ^{133}Ba source lines, from beam-on calibration histograms, were used to obtain detector resolutions at 283.5 keV and 373.0 keV, the energies corresponding to the $\Sigma^-\text{Pb}(12-11)$ and $\Sigma^-\text{Pb}(11-10)$ transition lines, respectively. The ^{57}Co lines and the three ^{192}Ir lines listed in Table XI were used to determine the resolution at 303 keV, the energy corresponding to the $\Sigma^-W(11-10)$ transition. The ^{192}Ir lines alone would have been adequate for the data from W; however, the ^{192}Ir source used for the first seven days of the W run was too weak. The ^{57}Co lines were therefore included as well to monitor resolution stability throughout this period of accumulating data in W.

The resolutions obtained for each calibration line in each subgroup of data within a group were averaged and these average resolutions were then fitted to a straight line. The parameters of these fits for resolution ys energy for each detector and group are listed in Table XIV. The linear function was

$$FWHM(x) = m(x-\bar{x}) + b \quad (5.5)$$

where x and \bar{x} are in keV and $FWHM$ is in eV. The value for \bar{x} is defined as

$$\bar{x} = \frac{\sum w_i x_i}{\sum w_i} \quad (5.6)$$

where the x_i are the respective calibration energies and the w_i are the weights determined from the fits to the subgroups. Included in Table XIV are the detector resolutions at the energies of important Σ^- x-ray transitions.

TABLE XIV
Beam-On Detector Resolution Parameters

Group	Detector	\bar{x} (keV)	m(eV/keV)	b (eV)	FWHM(283.5) (eV)	FWHM(373.0) (eV)
R1	A	341.5	1.128	975.9	910.4(<1.0)	1011.4(<1.0)
	B	340.9	1.183	1003.3	934.9(3.5)	1041.2(2.3)
	C	342.7	1.382	1051.5	969.6(3.6)	1093.4(2.2)
R2A	A	344.4	1.136	996.7	927.5(5.4)	1029.2(3.2)
	B	344.0	1.200	1023.5	950.8(7.5)	1058.2(4.5)
	C	344.9	1.365	1063.7	979.9(6.4)	1102.1(3.6)
R2B	A	343.8	1.265	1006.1	929.8(4.1)	1043.1(2.5)
	B	344.5	1.111	1033.5	965.7(2.5)	1065.1(1.4)
	C	345.1	1.387	1087.8	1002.3(10.2)	1127.9(5.9)
					FWHM(303.3) (eV)	
R3	A	125.0	1.286	750.0	979.2(<1.0)	
	B	124.6	1.323	752.6	989.0(5.8)	
	C	127.9	1.519	792.4	1058.8(5.4)	
$(\Delta FWHM)^2 = (\bar{x} - \bar{x})^2 (\Delta m)^2 + (\Delta b)^2$						

5.5 DETERMINATION OF NON-CIRCULAR CONTRIBUTIONS

The ratio A_1/A_0 of the amplitudes of non-circular to circular transitions was determined from a cascade calculation which was constrained to reproduce the relative yields of Σ^- x-ray transitions measured in this experiment. The total area of each of nine Σ^- x-ray peaks in the Pb data and seven Σ^- x-ray peaks in the W data was measured in the summed tagged spectra of the three detectors. These areas were then corrected for target transmission and detector relative efficiency. The detector relative efficiency was determined in the lab-

oratory and the target transmission was determined separately in the laboratory and with a Monte-Carlo program. The product $\epsilon(x)$ of these two corrections was tested for consistency by comparing the yields of kaonic x-ray transitions in the untagged data to those of Wiegand and Godfrey.⁷⁴

5.5.1 Detector Relative Efficiency

The relative efficiency $\epsilon(x)$ was determined by comparing the observed intensities of γ rays from calibration source sets with the known relative intensities of these lines. The γ rays from ^{133}Ba , ^{75}Se , ^{192}Ir , and ^{154}Eu were accumulated in the laboratory for each detector separately with the same data acquisition hardware and software used in the x-ray experiment itself. The area under each peak corresponding to a γ -ray line was determined by an integration of a large area subtending the peak and subtraction of an extrapolated background determined by a similar integration confined to the left or right of the peak. The determination of area by this method was independent of such factors as detector resolution and γ -line peak shape. This latter point was of concern since the detector crystals exhibited modest changes in response after the data runs from that of a pure Gaussian function. In addition, the data used in the determination of efficiency had extremely good S/N, thereby keeping the background component very small. An $\epsilon(x)$ vs energy curve was determined for each source set. Curves from different source sets were normalized by using a scale factor and holding the 356.0 keV line of ^{133}Ba at a defined relative efficiency of 1.0. A second-order polynomial fit to $\ln(\epsilon)$ vs energy was made to all the lines of the four

sets and, for detector B, formed the smooth curve shown in Fig 23. The curves for A and C were essentially identical to that for B.

5.5.2 Target Transmission

X rays from kaonic and sigma hyperonic atoms emanated from within the target plates. The straight-line paths from these locations to any of the detectors included a wide variation in the total quantity of matter traversed. Many of the x rays were either absorbed or scattered, depending both on the cross-sections for these processes and on the path. The study of target transmission $t_s(x)$ accounted for these effects.

5.5.2.1 Laboratory Measurement

A duplicate Pb target was made available to us by the BNL Hydrogen Target Group. The outer cylindrical shell and all insulating material was removed, exposing the array of Pb foils. This array was put on an Al plate equivalent in thickness to the target enclosure and together these were placed above the detector in the geometry of the experiment. Radioactive sources, used for the $r_e(x)$ determination, were sandwiched between small Pb foils of half the thickness of an array foil, simulating x rays emanating from within a plate. These sources were then placed at each of 24 points on a three-dimensional lattice within the target. At each point, data were collected for designated time periods according to Monte-Carlo estimates of the K^- stopping distribution. (A similar set of data taken with a uniform-time distribution gave similar results.) The procedure outlined above for the rela-

tive efficiency measurements was then repeated and a similar set of data points plotted. A fit to these data was made with a fifth-order polynomial in energy and is shown along with the data points in Fig. 24. The product function $s(x)$ was determined directly by this method.

5.5.2.2 Monte-Carlo Method

A Monte-Carlo program was used to determine $t_s(x)$ independently. An initial assumption was made for the distribution of K^- in the target giving a distribution of Σ^- atoms formed in the target plates. At each atom site, x rays were "emitted" isotropically. For those that intercepted a detector cylinder, the quantity of material crossed enroute was calculated. Tables of photon absorption cross sections⁷⁵ were then used to determine the fraction of photons that survived. The resulting $t_s(x)$ function was then multiplied by the $r_s(x)$ function obtained as described in section 5.5.1. The product is also shown in Fig. 24.

Evident in the figure is a small disagreement in the results obtained in the two methods for energies below 300 keV. There is excellent agreement above 300 keV. The discrepancy at low energies can be attributed to the fact that at these energies more than half of the x rays were absorbed and the product $r_s t_s (= s(x))$ was sensitive to the assumptions used to determine it. The functional distribution used in the analysis of x-ray relative yields was the average of the two results. A systematic error, which consisted of the absolute value of $\{s_{lab}(x) - s_{MC}(x)\}/2$, was always included in the analysis of yields, a discussion of which follows. For the W target, only the Monte-Carlo

distribution could be generated since no duplicate W target was available for a similar laboratory test. However, the systematic errors determined in the study for Pb were also applied to the W result.

5.5.2.3 Comparison of K^- X-ray Yields

Each of the K^-Pb and K^-W x-ray peaks in the summed untagged spectra was fitted to a single Gaussian (with free FWHM) and each area determined from the approximation

$$\text{AREA} = \text{Amplitude} \cdot \text{FWHM} \cdot 1.06. \quad (5.7)$$

Each of these areas was corrected for detector relative efficiency and for target transmission, as discussed above, and then normalized to the yield of the $K^-(9-8)$ transition. Normalized relative intensities determined with this method are listed in Table XV. These data were then compared to the results of Ref. 74 for those transitions measured in both works. A plot of the differences between these relative yields is shown in Fig. 25. A straight line is drawn corresponding to zero difference. The χ^2 of 8.6, for 9 degrees of freedom, obtained for this line is quite satisfactory. Since the experiment described in Ref. 74 was designed specifically for measuring yields, the good agreement between the present results and those of Ref. 74 implies that the product function $s(x)$ is understood.

TABLE XV

Relative Intensities of K^- Pb and K^- W Transitions

Transition n-n'	Pb		W	
	E(keV)	Relative Intensity	E(keV)	Relative Intensity
15-13	130.3	0.126±0.054	---	---
11-10	154.0	0.794±0.171	125.2	0.695±0.058
14-12	163.1	0.127±0.028	---	---
10-9	208.4	1.024±0.099	169.4	1.034±0.112
12-10	270.5	0.101±0.004	220.2	0.094±0.008
9-8	291.7	1.00	237.2	1.00
11-9	362.0	0.153±0.003	294.3	0.173±0.008
8-7	426.3	0.908±0.010	346.5	1.020±0.040
10-8	495.0	0.104±0.003	406.2	0.132±0.006

5.5.3 Cascade Calculation

5.5.3.1 Measured Values

The areas of Σ^- x-ray peaks in summed tagged histograms were determined in the same manner as those of the K^- x-ray peaks in the untagged data. There were two exceptions to this procedure. The $\Sigma^-(10-9)$ and $\Sigma^-(13-11)$ for both Pb and W were not resolved in energy. Instead, a small peak, corresponding to the 13-11 transition, was observed on the low-energy side of a larger broadened 10-9 transition. The total area was determined for these peaks (hereafter referred to as (13-11)+(10-9)). In the Pb data, this composite peak fell on the low-energy side of the 511 keV e^+e^- annihilation peak which prevented finding a satisfactory region over which to fit. An integration method was used to determine the total area. In W, the pair of peaks could be fitted to two single Gaussians with freely-varying widths. The

second exception was the peak corresponding to the $\Sigma^- \text{Pb}(12-10)$ transition which was quite broad and very low in yield. Fits with single and double Gaussians of free and fixed widths were performed in order to determine this area. In addition, the integration method was used. These methods resulted in a range of values for the total area in agreement with each other within the statistical errors. The area determined by the integration method was used since this method resulted in the most conservative error. The relative intensities for these Σ^- x-ray transitions in Pb and W are listed in Tables XVI and XVII, respectively. Also included in the Tables are the measured areas of the peaks.

5.5.3.2 Calculated Values

A hadronic-atom cascade program originally written by Seki and Leon was made available for our use. The strong-interaction optical parameters from Batty *et al.*⁷⁶ were used as input and the initial population of angular momentum states was taken as $(2\ell+1)\exp(\alpha\ell)$, with α adjusted to fit the data.¹⁴ The yield of the (10-9)+(13-11) pair, largely dominated by the (10-9) component, constrained the imaginary part of the strong-interaction scattering length. The value of the real part was found to have little effect and was therefore left at the reported value.⁷⁶ The intensities of several $\Delta n=-2$ transitions constrained the values permitted for α . The parameters α and $\text{Im } a$ (the imaginary part of the strong-interaction scattering length), were then varied until the best fit was obtained for the data. The intensities obtained in this cascade program are also listed in Tables XVI and XVII. Agreement between the measured and calculated values is excellent.

The ratios of the amplitudes of the non-circular and circular components for the $\Sigma^- \text{Pb}(12-11)$ and $\Sigma^-(11-10)$ in both Pb and W were determined from these best-fit parameters. The errors on these ratios were obtained by varying the parameter α until χ^2 changed by 1 from its lowest value (one σ error). The ratio A_1/A_0 was found to be 0.022 ± 0.005 for the $\Sigma^- \text{Pb}(11-10)$ transition, 0.122 ± 0.024 for the $\Sigma^- \text{Pb}(12-11)$ transition, and 0.120 ± 0.020 for the $\Sigma^- \text{W}(11-10)$ transition.

TABLE XVI

Relative Intensities of $\Sigma^- \text{Pb}$ Transitions

Transition n-n'	Measured Areas	Cascade Calculation	Experimental Values
15-14	1365 \pm 83	0.83	0.82 \pm 0.23
14-13	2479 \pm 106	0.91	0.92 \pm 0.17
13-12	3518 \pm 85	0.96	0.95 \pm 0.08
12-11	4401 \pm 89	<u>1.00</u>	<u>1.00</u>
15-13	410 \pm 79	0.084	0.091 \pm 0.018
11-10	4473 \pm 84	0.97	1.01 \pm 0.03
14-12	343 \pm 70	0.078	0.079 \pm 0.017
13-11 + 10-9	1905 \pm 138	0.59	0.58 \pm 0.05
12-10	150 \pm 77	0.048	0.053 \pm 0.034
Cascade input:	initial-n:	initial- ℓ distribution	SI optical potential scattering length (Re a + Im a)
	25	$(2\ell + 1)\exp(0.28\ell)$	(0.35 + 0.30) fm

TABLE XVII
Relative Intensities of Σ^- W Transitions

Transition n-n'	Measured Areas	Cascade Calculation	Experimental Values
14-13	686±54	0.85	0.94 ± 0.14
13-12	1126±55	0.94	0.91 ± 0.14
12-11	1755±57	<u>1.00</u>	<u>1.00</u>
11-10	1912±59	1.02	0.94 ± 0.07
14-12	263±47	0.13	0.13 ± 0.02
13-11 + 10-9	1544±69	1.00	0.84 ± 0.07
12-10	187±30	0.10	0.13 ± 0.02
Cascade input:	initial-n:	initial- ℓ distribution	SI optical potential scattering length (Re a + Im a) (0.35 + 0.30) fm
	25	$(2\ell + 1)\exp(0.097\ell)$	

5.6 STRONG-INTERACTION EFFECT ON THE N=10 STATE

As noted in section 3.2, the strong-interaction absorption reduces the intensity of the $\Sigma^-(10-9)$ transitions. The lifetime τ of the n=10 state is equal to

$$\tau = \frac{1}{R_{SI} + R_{EM}} \quad (5.8)$$

where R_{SI} and R_{EM} are the disappearance rates due to strong-interaction (SI) absorption and to electromagnetic (EM) transitions, respectively. The "natural" width Γ of a state is then given by $\Gamma = \hbar/\tau$. From the optical potential scattering lengths deduced in the last section we calculate a width of 23±7 eV for the n=10 state in Pb and 4±2 eV for the n=10 state in W. The values for Γ were determined using (Re a, Im a) of (0.35, 0.30 fm) and the uncertainties were based on a range⁷⁶ of Im a

from 0.19 fm to 0.43 fm, the latter determined from an upper limit of the cascade program used to fit the yield of the 10-9 transition with a one σ error.

The effect of such a width Γ on a transition viewed by a detector with a Gaussian response has been studied by Wilkinson.⁷⁷ For small $\Gamma/\text{FWHM}_{\text{inst}}$, the effective full-width at half-maximum is given by

$$\text{FWHM}_{\text{eff}} = \text{FWHM}_{\text{inst}} + 0.532 \Gamma, \quad (5.9)$$

where the subscripts "inst" and "eff" represent the instrumental and the effective resolutions, respectively. This relation results in a 12 eV and 2 eV increase respectively in the line-shape functions needed to describe the (11-10) transitions in $\Sigma^- \text{Pb}$ and $\Sigma^- \text{W}$. The 2 eV change has a negligible effect for the W case given the uncertainty in the instrumental resolution of the detectors. However, for Pb the effect is one that must be taken into account. Therefore, in the fits of the $\Sigma^- \text{Pb}(11-10)$ transition, an additional 12 eV has been added to the FWHM figures listed in Table XIV. With no such addition, the value obtained for $\mu(\Sigma^-)$ from these transitions alone changes by 0.01 μ_N , well within the statistical error.

5.7 NEW DETERMINATION OF MAGNETIC MOMENT

Three Σ^- x-ray transitions were analyzed for fine-structure splitting: the $\Sigma^- \text{Pb}(12-11)$, the $\Sigma^- \text{Pb}(11-10)$, and the $\Sigma^- \text{W}(11-10)$ transitions. The data set consisted of two types of spectra: tagged, characterized by excellent x-ray peak S/N, and untagged, characterized by poor x-ray peak S/N but of higher total statistics

by a factor of six. The Pb data were separated into three groups, as discussed, each group representing a distinct time period throughout the data runs. The W data were analyzed as one group. Additionally, for all of these groups, the data were further sorted according to detector. This division yielded 42 individual determinations of $\mu(\Sigma^-)$.

The functional form used to fit the Σ^- x-ray peaks for fine-structure splitting was

$$F(x) = D(x) + B_0 + B_1(x-x_0) + B_2(x-x_0)^2 \quad (5.10)$$

where $D(x)$ is given in Eq. (5.1). The function $f(x, x_1)$ was the single Gaussian (Eq. (5.3)) of fixed width given in Table XIV for particular energies, detectors, and groups of data. The Δ_1 and the quantity $(x_1 - x_0)$ were fixed for a given value of $\mu(\Sigma^-)$, leaving A_0 , x_0 , and the B_i as the free parameters in a fit. For each group of data, a series of fits was made at assumed values of the anomalous magnetic moment $g_1\mu_\Sigma$ in the range $-1.0 < g_1\mu_\Sigma < +2.0$, where μ_Σ is the sigma magneton. The step size chosen was $0.01 \mu_\Sigma$. This range corresponded to the interval $-1.57 < \mu(\Sigma^-) < +0.78 \mu_N$ with a step size of $0.0078 \mu_N$. For each fit, χ^2 was calculated and a χ^2 vs $\mu(\Sigma^-)$ map was generated. From these maps, the values of $\mu(\Sigma^-)$ and the corresponding statistical errors were determined.

5.7.1 The Sign of the Magnetic Moment

A χ^2 vs $\mu(\Sigma^-)$ map is shown in Fig. 26a for the tagged Σ^- Pb(11-10) data corresponding to group R2A for detector B. The minima correspond to the best-fit values of $\mu(\Sigma^-)$ and one notes that

the map gives both a "negative" and a "positive" result. In Fig. 26b, these data and the fit corresponding to the "negative" minimum of the map are shown, along with the component transitions which make up the peak shape. (Similar plots are shown in Figs. 27 and 28 for fits to the $\Sigma^- \text{Pb}(12-11)$ and $\Sigma^- \text{W}(11-10)$ transitions, respectively.) The double-valued nature of the χ^2 map corresponds to the "ordering" of the components, *i.e.*, the "negative" minimum corresponds to the $\ell + \frac{1}{2}$ to $\ell' + \frac{1}{2}$ transition being lower in energy and the "positive" minimum corresponds to the $\ell - \frac{1}{2}$ to $\ell' - \frac{1}{2}$ transition being lower in energy. Since the intensity of the $\ell + \frac{1}{2}$ to $\ell' + \frac{1}{2}$ transition is approximately 11% greater than that of the $\ell - \frac{1}{2}$ to $\ell' - \frac{1}{2}$, the ambiguity in sign can, in principle, be resolved. This resolution would be exhibited in χ^2 maps with minima for the "negative" solutions whose χ^2 is lower than that of the "positive" solutions by at least 1 (one σ).

In Fig. 26a, the "negative" solution is lower in χ^2 by 0.4 compared to the "positive" solution. Similarly, in other maps corresponding to fits to the rest of the data no significant difference in χ^2 is observed. To test whether the data, when considered as a whole, results in a definite determination of sign, the χ^2 maps for the separate transitions and for all of the data were added together. The χ^2 's corresponding to the minima of these summed maps are listed in Table XVIII for both the "negative" and "positive" solutions. The column labeled "DOFs" indicates the number of degrees of freedom in the fits which make up the summed map. Clearly the "negative" and "positive" solutions for the data are equally likely to within one σ .

TABLE XVIII

Comparison of Negative and Positive Solution Minima from Summed χ^2 Maps

Summed Maps	DOFs	χ^2 Minima	
		Negative Solution	Positive Solution
$\Sigma^- \text{Pb}(11-10)$	1044	1210.767	1210.494
$\Sigma^- \text{Pb}(12-11)$	774	776.989	777.984
$\Sigma^- \text{W}(11-10)$	288	270.450	270.826
All Data	2106	2259.523	2260.320

Results from tagged data only

The sign of $\mu(\Sigma^-)$ can be inferred from a comparison of the results of the present experiment to those obtained in the two Fermilab precession experiments (Refs. 11 and 13). Multi-valued solutions to the data are also present in the precession results. In these experiments, the magnetic moment is deduced from the angle of precession θ_p that the Σ^- polarization vector \mathbf{P} turns in a magnetic field. The induced rotation θ_p can be obtained from either a clockwise or an anti-clockwise rotation of \mathbf{P} . If in addition the sign of the initial direction of \mathbf{P} is not known, four configurations of the precession process can be inferred from the data. Finally, the unlikely possibility of any number of 2π rotations in addition to θ_p allows for further multiple solutions. Excluding these higher-order solutions ($\theta_p > 2\pi$), Deck *et al.*¹¹ obtain four results of which only one is compatible with the data reported here. Preliminary results of a second Σ^- precession experiment have

been reported by Marriner et al.¹³ In that experiment the initial polarization direction \mathbf{P} of the hyperon was deduced⁷⁸ from data obtained at both vertical and horizontal targeting angles. In addition, data were taken at two different values of the magnetic field integral. These procedures resulted in two values of θ_p from which $\mu(\Sigma^-)$ was deduced. Excluding the higher-order solutions as above, Marriner et al.¹³ tested the results obtained for $\mu(\Sigma^-)$ for self-consistency by assuming a clockwise rotation of \mathbf{P} and an anti-clockwise rotation of \mathbf{P} . Only one solution is statistically probable ($\chi^2/\nu = 1.07$), and this solution is compatible with the 'negative' value reported here. Their other solution is $\mu(\Sigma^-) = -0.21 \mu_N$ with a χ^2/ν of 2.65. The result for the initial polarization direction⁷⁸ can be used to eliminate two of the results from Ref. 11, but not the result $\mu(\Sigma^-) = +0.77 \pm 0.14 \mu_N$. The 'positive' value obtained in the experiment reported here (at the second χ^2 minimum) is $\mu(\Sigma^-) = +0.32 \pm 0.035 \mu_N$. These last three results are incompatible, and together they serve mutually to exclude each other. In the following section, we discuss only the 'negative' results obtained in this work.

5.7.2 The Magnitude of the Magnetic Moment

The fitting procedure outlined above was applied to the 42 data sets, resulting in an equal number of χ^2 maps. The values of $\mu(\Sigma^-)$ were determined from the 'negative' minima of these maps. One σ statistical errors were taken to be the differences between these values for $\mu(\Sigma^-)$ and those corresponding to an increase in χ^2 of 1 from the minima. The results obtained for the tagged data are shown in

Fig. 29 and the corresponding results obtained for the untagged data are shown in Fig. 30. Each of the points shown in these figures represents the result obtained from data sorted according to the divisions mentioned above. The error bars associated with each point correspond to one σ statistical errors. For some of the fits, only an upper limit on the magnitude of $\mu(\Sigma^-)$ could be determined because of the insensitivity of these fits to a separation of components less than a given value. These points are shown with upward-pointing arrows on the "positive-most" error bar. The solid line in each plot represents the average value obtained from the data points shown in each plot. These averages are $-1.111 \mu_N$ for the tagged data and $-1.174 \mu_N$ for the untagged data. The dashed lines represent statistical errors of $\pm 0.031 \mu_N$ and $\pm 0.027 \mu_N$ respectively for the two averages.

We next examine the data for consistency with respect to such factors as detector, transition, and, in particular, tagged vs untagged mode. A comparison of the results derived from data divided in this manner is shown in Table XIX. The combined results were obtained by averaging the results from the fits. The statistical consistency of the results within a set was evaluated by computing the values of χ^2/ν for the members of a set with respect to the average result from all of the data. This was done for the four sets labeled: TAGGED/DETECTOR, TAGGED/TRANSITION, UNTAGGED/DETECTOR, and UNTAGGED/TRANSITION. The χ^2/ν values are also given in Table XIX. This comparison shows excellent consistency in all cases except for the UNTAGGED/TRANSITION case in which a χ^2/ν of 13.1 is obtained. The largest contribution to this poor χ^2/ν is due to the value for $\mu(\Sigma^-)$ obtained from the Pb(12-11) transition. The results from the untagged Σ^- Pb(11-10) and

$\Sigma^-W(11-10)$ transitions agree very well with those from the tagged data.

TABLE XIX
Comparison of Results for Consistency

CATEGORY	TAGGED (μ_N)	UNTAGGED (μ_N)
DETECTOR: A	-1.146±0.050	-1.169±0.045
B	-1.126±0.049	-1.157±0.046
C	-1.034±0.059	-1.201±0.053
χ^2/ν for this set:*	1.04	0.21
TRANSITION: $\Sigma^-Pb(11-10)$	-1.085±0.037	-1.080±0.035
$\Sigma^-Pb(12-11)$	-1.154±0.074	-1.394±0.051
$\Sigma^-W(11-10)$	-1.196±0.089	-1.116±0.089
χ^2/ν for this set:*	0.87	13.1

* χ^2/ν were calculated for three points of a set with respect to average of set (-1.111 for TAGGED, -1.174 for UNTAGGED)

It is important to investigate whether the rather large value obtained for $\mu(\Sigma^-)$ from the untagged $\Sigma^-Pb(12-11)$ transition could be statistically probable. To answer this, the results of the two previous exotic-atom determinations^{16,18} of $\mu(\Sigma^-)$ are useful. In both of those experiments, data were collected in a mode similar to that of collecting untagged data in the present work, although the S/N of x-ray peaks was somewhat poorer in the earlier experiments. The determination of $\mu(\Sigma^-)$ by Dugan *et al.*¹⁸ was based entirely on the $\Sigma^-Pb(12-11)$ transition. The measurement by Roberts *et al.*¹⁶ was based primarily on this transition. Table XX includes the values of $\mu(\Sigma^-)$ obtained in analyses of fine-structure splittings in untagged

Σ^- Pb(12-11) x-ray peaks. For the present data, these results are given separately by detector. These five results (including two from Refs. 16 and 18), which give an average value of $\mu(\Sigma^-)$ of $-1.39 \pm 0.05 \mu_N$, are in excellent agreement with each other but are incompatible with any of the other determinations of $\mu(\Sigma^-)$, reported either here or in Refs. 11 and 13.

The difference in the results obtained for $\mu(\Sigma^-)$ from the tagged and untagged Σ^- Pb(12-11) transitions cannot be attributed to conditions under which the data were either collected or analyzed since these were the same in both cases. The playback of the data tapes was identical for tagged (pared down) and untagged data. Also, the result for the untagged Σ^- Pb(11-10) transition is in excellent agreement with its tagged counterpart, thereby reducing the possibility of a peculiar analysis-related error. Simple fits of the Σ^- Pb(12-11) peaks to single Gaussians of adjustable widths yielded the following conclusions. As expected from the larger value obtained for the magnetic moment from the untagged data, the width in the fits was 90 ± 30 eV greater for the untagged Σ^- Pb(12-11) peak compared to the tagged. The Gaussian centroid of the untagged peak differed from that of the tagged peak by -17 ± 12.6 eV. Finally, the peak-area ratio of untagged to tagged was 6.8 for the Σ^- Pb(12-11) peaks and 5.4 for the Σ^- Pb(11-10) peaks. These facts hint at the possibility of one (or more) contaminant lines lying beneath the peak in the untagged Σ^- Pb(12-11) data, although a larger centroid shift would have constituted a more definitive conclusion. This inconsistency will be discussed further in Chapter VI.

TABLE XX

Comparison of $\mu(\Sigma^-)$ Measurements Based on the Untagged $\Sigma^- \text{Pb}(12-11)$ Transition

<u>Ref.</u>	<u>$\mu(\Sigma^-)$ (Nuclear Magnetons)</u>	
16	-1.48 ± 0.37	
18	$-1.40 \begin{smallmatrix} +0.41 \\ -0.28 \end{smallmatrix}$	
This Expt.	-1.383 ± 0.079	(Det A)
	-1.324 ± 0.096	(Det B)
	-1.453 ± 0.092	(Det C)
Average	-1.39 ± 0.05	

5.8 DETERMINATION OF SYSTEMATIC ERRORS

The determination of $\mu(\Sigma^-)$ from the fine structure of x-ray transitions requires knowledge of parameters used to specify the line-shape of the detectors, of the relative composition of doublet components, and possibly of the width induced by the strong interaction. The sensitivity of $\mu(\Sigma^-)$ to the uncertainties in the values of these parameters constitutes the systematic error. We discuss next tests of the method employed to extract the splitting of fine-structure components from a single broadened peak and also establish systematic errors on the determination of $\mu(\Sigma^-)$.

5.8.1 Tests of the Fitting Technique

5.8.1.1 Computer Simulations

A data simulation routine was used to generate "doublets" on "backgrounds" in which one varied the assumed splitting of the doublet, total number of counts in the doublet, S/N, FWHM of the components, and the ratio A_1/A_0 . Random Gaussian statistics were applied to the composite curves so formed, and these simulations were then fitted with the same routines used in the actual analysis of the data. Many cases studied over a wide range in the values of input parameters indicated that the input splitting was recovered from the fitting routines within the statistical errors. For the same total area within a doublet, the precision obtained in determining the splitting of the components was dependent on the values of the other input parameters. For example, doublets formed from Gaussian components of large FWHM were fitted with less precision than corresponding doublets formed with small FWHM. Similarly, doublets with large splittings could be fitted with higher precision than those with small splittings. The simulations indicated that the ability to extract a definite value for $\mu(\Sigma^-)$ could be made only if the actual value of $\mu(\Sigma^-)$ was greater in magnitude than $0.5 \mu_N$. This limitation includes even the lowest theoretical prediction⁵⁰ for $\mu(\Sigma^-)$. In addition, it forecasts difficulties for any future attempt to measure $\mu(\Xi^-)$ by the exotic-atom method.

Simulations were also used to test the sensitivity to the sign of $\mu(\Sigma^-)$. In these cases, S/N, total number of counts in the doublet, and the FWHM were determined from the actual data and were used as fixed inputs. Only the splitting of the doublet components was varied.

For splittings corresponding to a magnetic moment less in magnitude than about $1.2 \mu_N$, the sensitivity to the sign of $\mu(\Sigma^-)$ disappears.

5.8.1.2 Laboratory Simulations

The fitting technique was also tested with actual data collected with the same spectroscopy system that was used in the x-ray experiment. In these tests, the doublet was formed from individual γ -ray lines separated in energy by an amount similar to that of the components within a Σ^- x-ray peak (see Table III). Spectra⁶⁹ of radioactive ^{203}Hg , ^{75}Se , and ^{182}Ta were collected separately using one of the detectors. The 279.197(1) keV line from ^{203}Hg , the 264.651(8) keV and 279.528(8) keV lines from ^{75}Se , and the 264.075 keV line from ^{182}Ta were then each fitted to single Gaussian functions to establish the FWHM and amplitude of each peak. A "background" spectrum was collected using Compton-scattered events from the high-energy γ -ray lines in ^{60}Co . The ^{203}Hg spectrum and the ^{75}Se spectrum were then summed with the background spectrum to form a doublet at approximately 279 keV with components separated in energy by 331 eV. A second such doublet was formed from the spectra of ^{75}Se and ^{182}Ta , together with background and resulted in a doublet peak at approximately 264 keV separated in energy by 576 eV. Each of the composite peaks was then subjected to the fitting procedure outlined above, and in each case the separation of the peaks was correctly determined to within the statistical errors.

5.8.2 Sensitivity of Magnetic Moment to Input Parameters

The sensitivity of the result for $\mu(\Sigma^-)$ to the values of the input parameters of the fits was tested separately for each of the three relevant transitions. In all cases, these determinations were made by fitting the data at the extremes of the one σ uncertainties of the input parameters themselves. For example, the FWHM at the energies of the Σ^- x-ray peaks are listed in Table XIV with their associated errors. For each transition, a representative set of data was fitted with the FWHM \pm the largest error on the FWHM at that transition. Similarly, this procedure was used with the ratios A_1/A_0 given in section 5.5.3.2. The sensitivity of $\mu(\Sigma^-)$ to the region of fit used for each transition was also tested. Only for the Σ^- Pb(12-11) transition was it difficult to find a satisfactory region in which no statistically significant change in $\mu(\Sigma^-)$ occurred. For this transition, therefore, the largest change in $\mu(\Sigma^-)$ encountered by fitting over a wide range of regions was included.

The uncertainty in the value of $\mu(\Sigma^-)$ due to the width induced by the strong interaction has been described in section 5.6.

The results of these studies are listed in Table XXI by transition and by parameter. In each case, the relevant error associated with a parameter (if available) is given. The method by which the uncertainty in a parameter was included in the determination of the net effect on a given transition is listed next. "Quad/Fit" indicates that the uncertainty was folded into the results of each of the fits which determines the uncertainty of $\mu(\Sigma^-)$ extracted from that transition. "Direct" indicates a linear addition of the uncertainty to the net re-

sult. The final column contains the magnitude and sign of the uncertainties in nuclear magnetons. The sign (when indicated) is with respect to the sign of the individual parameters. The sum of these effects is taken as the systematic error to be used for the relevant transition.

TABLE XXI

Systematic Errors by Transition

<u>Transition</u>	<u>Parameter</u>	<u>This Item</u>	<u>Method Added</u>	<u>Error (μ_N)</u>
Pb(11-10)	FWHM	± 6 eV	Quad/Fit	∓ 0.002
	A_1/A_0	± 0.005	Direct	∓ 0.002
	SI width	± 7 eV	Direct	∓ 0.003
			SUM	0.007
Pb(12-11)	FWHM	± 10 eV	Quad/Fit	∓ 0.003
	A_1/A_0	± 0.024	Direct	∓ 0.016
	Fit Region	----	Quad/Fit	$\underline{0.003}$
			SUM	0.022
W(11-10)	FWHM	± 6 eV	Quad/Fit	∓ 0.001
	A_1/A_0	± 0.020	Direct	∓ 0.010
	SI width	± 2 eV	Direct	∓ 0.004
			SUM	0.015

Chapter VI

CONCLUSIONS

The magnetic moment of the Σ^- hyperon has been deduced from measurements of the fine structure of several transitions in Σ^- Pb and Σ^- W atoms. In the tagged data sets, Σ^- x-ray peaks were the most prominent peaks in the spectra. The signal-to-noise ratio for these peaks is about 3:1. In the untagged data sets, these same peaks exhibited substantially poorer S/N but higher overall yield. A comparison of the results obtained for $\mu(\Sigma^-)$ according to tagged and untagged data showed a clear inconsistency for one of the transitions in the untagged mode, namely the Σ^- Pb(12-11) transition. The result obtained for $\mu(\Sigma^-)$ from analysis of this transition alone was more than five σ from the average of the results for the tagged data. In previous exotic-atom determinations^{16,18} of $\mu(\Sigma^-)$, this same transition, in an untagged mode, yielded essentially the same result. The possibility that an unknown background contaminant may lie under this peak, a danger inherent in data of poor S/N, should be considered. The effect of such a contaminant could be to broaden the Σ^- x-ray peak and thus yield a consistently large, but incorrect, result for the magnitude of $\mu(\Sigma^-)$. The values determined for $\mu(\Sigma^-)$ from the untagged Σ^- Pb(11-10) and the Σ^- W(11-10) transitions do not indicate such problems. However, the most reliable determination of

$\mu(\Sigma^-)$ can be made only from the data of the highest overall quality. The values obtained from the tagged data, shown in Fig. 31 by transition and by detector, form a consistent statistical set of results (χ^2 equal to 10.3 for 8 degrees of freedom). Therefore, in the present work, we consider only the tagged data for the final result. The magnetic moment of the Σ^- hyperon obtained from tagged transitions in Pb and W targets is

$$\mu(\Sigma^-) = -1.111 \pm 0.031 \pm 0.011 \mu_N$$

where the first error is statistical and the second represents the systematic error, based on the weighted average of the summed systematics listed in Table XXI.

This result compares favorably in precision with the recent results from experiments in which a precession technique was used. Deck et al.¹¹ obtained $\mu(\Sigma^-) = -0.89 \pm 0.14 \mu_N$ and Marriner et al.¹³ obtained $\mu(\Sigma^-) = -1.18 \pm 0.03 \mu_N$ in their preliminary analysis. Although the final results of this latter measurement could be significantly different, the preliminary weighted average of the three is computed to be

$$\mu(\Sigma^-) = -1.15 \pm 0.02 \mu_N.$$

The results from the two precession experiments tentatively disagree by two σ . The result reported here lies in between. The completed analysis of the data from the second precession experiment is of considerable interest.

6.1 THEORETICAL IMPLICATIONS

The accuracy of predictions for baryon magnetic moments from the models discussed in Chapter II is expected to be no better than 10%. Isgur and Karl³² point out that nonstatic effects can affect the AQM results to about this level. Theberge and Thomas⁷⁹ discuss similar ambiguities associated with bag-model calculations. For example, center-of-mass corrections, configuration mixing, and sea quark effects could contribute to this level. They conclude that discrepancies of about $0.1 \mu_N$ between their own results and experiment could arise from such higher-order effects. With this in mind, we examine this new experimental result with respect to the example calculations described in Chapter II.

The sum-rule test of spin independence³⁴ leads to the prediction of $\mu(\Sigma^-) = -0.86 \mu_N$ which is in poor agreement with $\mu(\Sigma^-) = -1.111 \pm 0.042 \mu_N$, the result of this experiment. However, in Ref. 79, the authors argue that the relation given in Eq. (2.14.c) contains a pionic correction of about $0.34 \mu_N$. If the authors are correct, the usefulness of such sum rules is lessened.

In his analysis, Lipkin³⁹ suggests that nonstrange-quark moments are enhanced in nucleons compared to strange baryons. This implies that the relation $\mu(\Sigma^-) = (\frac{1}{3}\mu_d - \frac{2}{3}\mu_s)$ should have a much smaller magnitude than that derived with the AQM. Based on parameters used to predict the other octet magnetic moments, Lipkin calculates $\mu(\Sigma^-)$ to be equal to $-0.81 \mu_N$. In the little bag model, Brown, Rho, and Vento⁵⁰ develop a mechanism which effectively quenches the nonstrange quark-moment contributions in strange baryons. They note that pionic correc-

tions affect the nucleon and the strange-baryon magnetic moments differently. As in the Lipkin analysis, the predicted value for $\mu(\Sigma^-)$ is quite small, namely $\mu(\Sigma^-) < 0.64 \mu_N$ in magnitude. The recent additional inclusion of kaon cloud contributions by Gonzalez, Vento, and Rho⁸⁰ does not significantly change the predictions. The value $\mu(\Sigma^-) = -1.111 \pm 0.042 \mu_N$ obtained in this experiment is in sharp contrast to the results of both models which advocate a mechanism for enhanced nonstrange-quark moment contributions in the nucleons and a lessening of the nonstrange-quark contributions to the magnetic moments of the strange baryons.

In the CBM formalism, Theberge and Thomas⁵² obtain $\mu(\Sigma^-) = -1.08 \mu_N$. Their more recent work⁷⁹ includes results from calculations over a wide range in the input bag radius R . From $R = 0.7$ fm to about $R = 1.2$ fm the predictions for $\mu(\Sigma^-)$ are fairly constant and in agreement with the experimental result given here.

Finally, we note that although the AQM does not reproduce the results for the entire spectrum of baryon magnetic moments, the prediction of $\mu(\Sigma^-) = -1.05 \mu_N$ is in agreement with the results documented in this report.

REFERENCES

1. O. Stern and W. Gerlach, *Zeitschrift fur Physik* 8, 110 (1922).
2. G.E. Uhlenbeck and S. Goudsmit, *Die Naturwissenschaften* 13, 953 (1925) and G.E. Uhlenbeck and S. Goudsmit, *Nature* 117, 264 (1926).
3. J.B. Taylor, *Zeitschrift fur Physik* 41, 551 (1927).
4. P.A.M. Dirac, *Proceedings of the Royal Society of London (A)* 117 (1928).
5. For a review of (g-2) experiments and theoretical references, see for example, F.J.M. Farley and E. Picasso, *Ann. Rev. Nucl. and Part. Sci.* 29, 243 (1979).
6. L. Schachinger, G. Bunce, P.T. Cox, T. Devlin, J. Dworkin, B. Edelman, R.T. Edwards, R. Handler, K. Heller, R. March, P. Martin, O.E. Overseth, L. Pondrom, M. Sheaff, and P. Skubic, *Phys. Rev. Lett.* 41, 1348 (1978).
7. G. Bunce, O.E. Overseth, P.T. Cox, J. Dworkin, K. Heller, T. Devlin, B. Edelman, R.T. Edwards, L. Schachinger, P. Skubic, R. Handler, R. March, P. Martin, L. Pondrom, and M. Sheaff, *Phys. Lett.* 86B, 386 (1979) and P.T. Cox, J. Dworkin, O.E. Overseth, R. Handler, R. Grobel, L. Pondrom, M. Sheaff, C. Wilkinson, L. Deck, T. Devlin, K.B. Luk, R. Rameika, P. Skubic, K. Heller, and G. Bunce, *Phys. Rev. Lett.* 46, 877 (1981).
8. R. Rameika, Ph.D. Thesis, Rutgers University 1981 (unpublished).
9. R. Handler, R. Grobel, B. Lundberg, L. Pondrom, M. Sheaff, C. Wilkinson, A. Beretvas, L. Deck, T. Devlin, B. Luk, R. Rameika, P.T. Cox, C. Dukes, J. Dworkin, O. Overseth, and K. Heller, *AIP Conference Proceedings High Energy Spin Physics - 1982*, 95, 55 (1983).
10. R. Settles, A. Manz, W. Matt, T. Hansl, I. Herynek, N. Doble, G. Wolf, S. Rencroft, J. Marraffino, J. Waters, M. Webster, and C.E. Roos, *Phys. Rev. D* 20, 2154 (1979).
11. L. Deck, Ph.D. Thesis, Rutgers University 1981 (unpublished) and L. Deck, A. Beretvas, T. Devlin, K.B. Luk, R. Rameika, R. Whitman, R. Handler, B. Lundberg, L. Pondrom, M. Sheaff, C. Wilkinson, P.T. Cox, C. Dukes, J. Dworkin, O.E. Overseth, and K. Heller, (to be published in *Phys. Rev. D*).
12. Particle Data Group, *Phys. Lett.* 111B (1982).

13. J.P. Marriner, E.W. Anderson, C. Ankenbrandt, J.P. Berge, A. Breakstone, E. E. Brenner, J. Butler, T. Cardello, P.S. Cooper, K. Doroba, J. Elias, J. Lach, P. Laurikainen, J. MacLachlan, E. McCliment, L.J. Teig, J. Thron, and Y.W. Wah, AIP Conference Proceedings High Energy Spin Physics - 1982, 95, 64 (1983).
14. C.J. Batty, Exotic Atoms; A Review, Report RL-80-094, Rutherford and Appleton Laboratories (1980).
15. J.D. Fox, P.D. Barnes, R.A. Eisenstein, W.C. Lam, J. Miller, R.B. Sutton, D.A. Jenkins, R.J. Powers, M. Eckhause, J.R. Kane, B.L. Roberts, M.E. Vislay, R.E. Welsh, and A.R. Kunselman, Phys. Rev. Lett. 29, 193 (1972).
16. B.L. Roberts, C.R. Cox, M. Eckhause, J.R. Kane, R.E. Welsh, D.A. Jenkins, W.C. Lam, P.D. Barnes, R.A. Eisenstein, J. Miller, R.B. Sutton, A.R. Kunselman, R.J. Powers, and J.D. Fox, Phys. Rev. D 12, 1232 (1975).
17. E. Hu, Y. Asano, M.Y. Chen, S.C. Cheng, G. Dugan, L. Lidofsky, W. Patton, C.S. Wu, V. Hughes, and D. Lu, Nucl. Phys. A254, 403 (1975).
18. G. Dugan, Y. Asano, M.Y. Chien, S.C. Cheng, E. Hu, L. Lidofsky, W. Patton, C.S. Wu, V. Hughes, and D. Lu, Nuc. Phys. A254, 396 (1975).
19. See for example, D.H. Perkins, Introduction to High Energy Physics, 2nd ed., Chapter 5 (Addison-Wesley, Reading, 1982) and M. Leon, Particle Physics, An Introduction, (Academic Press, New York, 1973).
20. S. Coleman and S.L. Glashow, Phys. Rev. Lett. 6, 423 (1961).
21. M.A.B. Beg, B.W. Lee, and A. Pais, Phys. Rev. Lett. 13, 514 (1964).
22. A. De Rujula, H. Georgi, and S.L. Glashow, Phys. Rev. Lett. D 12, 147 (1975).
23. H.R. Rubinstein, F. Scheck, and R.H. Socolow, Phys. Rev. 154, 1608 (1967).
24. T.P. Cheng and H. Pagels, Phys. Rev. 172, 1635 (1968).
25. J. Franklin, Phys. Rev. 172, 1807 (1968) and J. Franklin, Phys. Rev. 182, 1607 (1969).
26. D.G. Caldi and H. Pagels, Phys. Rev. D 10, 3739 (1974).
27. A. Bohm, Phys. Rev. D 18, 2547 (1978).
28. Y. Tomozawa, Phys. Rev. D 19, 1626 (1979) and Y. Tomozawa, Phys. Rev. D 25, 795 (1982).

29. H. Lipkin, Phys. Rev. Lett. 41, 1629 (1978).
30. R.B. Teese and R. Settles, Phys. Lett. 87B, 111 (1979).
31. D.A. Geffen and W. Wilson, Phys. Rev. Lett. 44, 370 (1980).
32. N. Isgur and G. Karl, Phys. Rev. D 21, 3175 (1980).
33. R.C. Verma, Phys. Rev. D 22, 1156 (1980).
34. J. Franklin, Phys. Rev. Lett. 45, 1607 (1980).
35. T. Das and S.P. Misra, V High Energy Physics Symposium, Tripunithura, India Dec 1980.
36. C.P. Singh, Phys. Rev. D 23, 2085 (1981).
37. S. Oneda, T. Tanuma, T. Toiya, and M. Slaughter, Phys. Rev. D 23, 787 (1981).
38. D.L. Lichtenberg, E. Predazzi, and J.G. Wills, (preprint) APR 1982.
39. H.J. Lipkin, Nucl. Phys. B214, 136 (1983).
40. S.B. Khadkikar and S.K. Gupta, Phys. Lett. 124B, 523 (1983).
41. H. Fritzsche, (preprint) "Comment About the Magnetic Moments of the Hyperons" 1979.
42. J. Franklin, Phys. Rev. D 20, 1742 (1979) and J. Franklin, (preprint) "Sum Rule Tests of Baryon Magnetic Moments" Aug 1982 and J. Franklin, (preprint) "General Quark Model Analysis of Baryon Magnetic Moments." Jan 1983.
43. H.J. Lipkin, Phys. Lett. 89B, 358 (1980) and H.J. Lipkin, (preprint) Fermilab - Pub -80/95, "Magnetic Moments of Composite Quarks and Leptons--Further Difficulties", Dec 1980 and H.J. Lipkin, Phys. Rev. D 24, 1437 (1981).
44. T. DeGrand, R.L. Jaffe, K. Johnson, and J. Kiskis, Phys. Rev. D 12, 2060 (1975).
45. A. Chodos, R.L. Jaffe, K. Johnson, C.B. Thorn, and V.F. Weisskopf, Phys. Rev. D 9, 3471 (1974) and A. Chodos, R.L. Jaffe, K. Johnson, and C.B. Thorn, Phys. Rev. D 10, 2599 (1974).
46. For a recent critical review of bag models, see C.E. DeTar and J.F. Donoghue, Ann. Rev. Nucl. and Part. Sci. 33 (1983).
47. A. Chodos and C.B. Thorn, Phys. Rev. D 12, 2733 (1975).
48. A review of pionic corrections to the MIT bag model is given in G.A. Miller, S. Theberge, and A.W. Thomas, Comments Nucl. Part. Phys. 10, 101 (1981).

49. G.E. Brown and M. Rho, *Phys. Lett.* **82B**, 177 (1979).
50. G.E. Brown, M. Rho, and V. Vento, *Phys. Lett.* **97B**, 423 (1980).
51. S. Theberge, A.W. Thomas and G.A. Miller, *Phys. Rev. D* **22**, 2835 (1980).
52. S. Theberge and A.W. Thomas, *Phys. Rev. D* **25**, 284 (1982).
53. Marvin Blecher (unpublished).
54. J. Bloomquist, *Nucl. Phys.* **B48**, 95 (1972).
55. P. Vogel, *Atomic and Nuclear Data Tables* **14**, 599 (1974).
56. T.E.O. Ericson and J. Hufner, *Phys. Lett.* **40B**, 459 (1972).
57. E. Borie and G.A. Rinker, *Rev. Mod. Phys.* **54**, 67 (1982).
58. B.L. Roberts, *Phys. Rev. D* **17**, 358 (1978).
59. H.A. Bethe and E.E. Salpeter, *Quantum Mechanics of One- and Two-Electron Atoms* (Springer-Verlag, Berlin, 1957).
60. J. Hufner, F. Scheck, and C.S. Wu, Chapter III of *Muonic Physics I*, ed. V.W. Hughes and C.S. Wu (Academic, New York, 1977).
61. D. Zieminska, *Phys. Lett.* **37B**, 403 (1971).
62. B.L. Roberts, private communication.
63. J.D. Fox, Brookhaven National Laboratory Accelerator Dept., EP&S Division Technical Note No. 20 (1968) (unpublished).
64. V. Fitch and R. Motley, *Phys. Rev.* **101**, 496 (1956).
65. R.B. Sutton and N.J. Colella, Carnegie-Mellon University (unpublished).
66. K.L. Giovanetti, Ph.D. Thesis, The College of William and Mary in Virginia, 1982 (unpublished).
67. R.H. Pehl, N.W. Madden, J.H. Elliott, T.W. Raudorf, R.C. Trammell, and L.S. Darken Jr., *IEEE Nucl. Sci. Symp.*, Washington D.C. (1978).
68. D.A. Landis, C.P. Cork, N.W. Madden, and F.S. Goulding, Lawrence Berkeley Laboratory, Report **13214** (unpublished).
69. *Table of Isotopes* 7th Ed., C.M. Lederer and V.S. Shirley ed., (John Wiley and Sons, New York, 1978).
70. L.R. Biswell and R.E. Rajala, Los Alamos Report **5144** (1973).
71. Copyright Digital Equipment Corp., RSX-11M V03.1 (1978).

72. J.F. Bartlett, J.R. Biel, D.B. Curtis, R.J. Dosen, T.D. Lagerlund, D.J. Ritchie, and L.M. Taff, *IEEE Trans. Nucl. Sci.* NS-26 (1979).
73. P.R. Bevington, Data Reduction and Error Analysis for the Physical Sciences, (McGraw-Hill, New York, 1966).
74. C.E. Wiegand and G.L. Godfrey, *Phys. Rev. A* 9, 2282 (1974).
75. E. Storm and H.I. Israel, Los Alamos Report 3753 (1967).
76. C.J. Batty, S.F. Biagi, M. Blecher, S.D. Hoath, R.A.J. Riddle, B.L. Roberts, J.D. Davies, G.Y. Pyle, G.T.A. Squier, and D.M. Asbury, *Phys. Lett.* 74B, 27 (1978).
77. D.H. Wilkinson, *Nucl. Inst. and Meth.* 95, 259 (1971).
78. P.S. Cooper, E.W. Anderson, C. Ankenbrandt, J.P. Berge, A. Breakstone, E. E. Brenner, J. Butler, T. Cardello, K. Doroba, J. Elias, J. Lach, P. Laurikainen, J. MacLachlan, J.P. Marriner, E. McCliment, L.J. Thron, and Y.W. Wah, *AIP Conference Proceedings High Energy Spin Physics - 1982*, 95, 102 (1983).
79. S. Theberge and A.W. Thomas, *Nucl. Phys.* A393, 252 (1983).
80. P. Gonzalez, V. Vento, and M. Rho, *Nucl. Phys.* A395, 446 (1983).

LIST OF TABLES

<u>Table</u>		<u>page</u>
I.	Recent Measurements of Strange Baryon Magnetic Moments in Precession Experiments	4
II.	Theoretical and Experimental Magnetic Moment Values	12
III.	Targets and Transitions Analyzed in the Experiment	25
IV.	Spin-up to Spin-down Intensity Ratios	29
V.	C4 Beam Line Elements and Settings for 680 MeV/c	33
VI.	Beam Telescope Counters	36
VII.	Reactions Producing Energetic Charged Pions Following K^- Stops in Target T	41
VIII.	Detector Specifications	42
IX.	Spectroscopy System Electronic Modules	46
X.	Principal K_S -Induced Events	47
XI.	Calibration Sources	48
XII.	CAMAC Crate Composition	49
XIII.	Data Set	53
XIV.	Beam-On Detector Resolution Parameters	62
XV.	Relative Intensities of K^-Pb and K^-W Transitions	67
XVI.	Relative Intensities of Σ^-Pb Transitions	69
XVII.	Relative Intensities of Σ^-W Transitions	70
XVIII.	Comparison of Negative and Positive Solution Minima from Summed χ^2 Maps	74
XIX.	Comparison of Results for Consistency	77

XX.	Comparison of $\mu(\Sigma^-)$ Measurements Based on the Untagged $\Sigma^- \text{Pb}(12-11)$ Transition	79
XXI.	Systematic Errors by Transition	83

FIGURE CAPTIONS

<u>Figure</u>	<u>page</u>
1. Selected transitions between atomic energy states labeled by the principal and orbital quantum numbers. Fine-structure splittings and $\Delta\ell=+1$ transitions not shown for clarity.	98
2. Circular and first non-circular (11-10) transitions including fine-structure components.	99
3. Layout of AGS C4 beam line. A series of magnetic lenses is used to transport particles of a desired momentum.	100
4. Experimental apparatus including beam-defining plastic scintillators, π^+ spectrometers, and intrinsic Ge detectors located below target T.	101
5. Typical beam time-of-flight histogram gated by $S1 \cdot S2 \cdot C \cdot S3 \cdot S4 \cdot S5$	102
6. Beam horizontal(a) and vertical(b) profiles in the hodoscope. Histograms gated by $S1 \cdot S2 \cdot C \cdot S3 \cdot S4 \cdot S5$	103
7. Pulse height in counter S5 gated by $S1 \cdot S2 \cdot C \cdot S3 \cdot S4 \cdot S5$. A 300 mV threshold was placed on S5 in the data runs to select stopping kaons by dE/dX	104
8. Beam telescope logic block diagram. Units contained within dashed box were located just outside the experimental area; others were housed in a nearby counting trailer.	105
9. Sketch showing laminar target foil array and surrounding cryogenic housing (a) — side view, (b) — front view.	106
10. Logic diagram for left-arm π^+ spectrometer (right side identical).	107
11. Delayed events recorded in right π^+ spectrometer fit to $A \cdot \exp[-t/\tau] + B$ with the result for the μ^+ lifetime $\tau = 2.26 \pm 0.1$ μsec	108
12. Ge detector array showing top and side views of detector housing and relative positions of crystals.	109
13. Histogram of time coincidence events $KS \cdot \gamma(A)$ between KS signals and detector A events.	110

14. Logic diagram showing those Ge spectroscopy system units which were housed in thermally controlled environment near the experimental area. 111
15. Logic diagram showing Ge spectroscopy-system gating and event-type identification circuitry. 112
16. Logic diagram showing CAMAC gating and CAMAC modules. MBD was interrupted by LAM from trigger module. 113
17. A portion of the energy spectrum from summed tagged(a) and untagged(b) histograms showing the dramatic effect of tagging on Σ^- x-ray signal-to-noise. 114
18. Untagged Pb x-ray summed (A+B+C) histogram with transitions as indicated. Horizontal scale: $E(\text{keV}) = (\text{Channel}+851.5) * 0.090$ 115
19. Tagged Pb x-ray summed histogram with transitions as indicated. Horizontal scale: $E(\text{keV}) = (\text{Channel}+851.5) * 0.090$ 116
20. Untagged W x-ray summed histogram with transitions as indicated. Horizontal scale: $E(\text{keV}) = (\text{Channel}+851.5) * 0.090$ 117
21. Tagged W x-ray summed histogram with transitions as indicated. Horizontal scale: $E(\text{keV}) = (\text{Channel}+851.5) * 0.090$ 118
22. A distribution of the χ^2/ν obtained from the individual fits to the four ^{133}Ba lines in the Pb data subgroups. 119
23. Relative efficiency of detector B. Fit is $\ln(\text{re})$ vs energy (keV) to second-order polynomial with coefficients: 2.026, -7.35×10^{-3} , and 4.74×10^{-6} , respectively. 120
24. Relative efficiency * target transmission vs energy determinations made in the laboratory, with accompanying fit, and with a Monte-Carlo simulation (bold). 121
25. Differences between the relative intensities of various kaonic Pb and W transitions in the present work and in that of Ref. 74. A line is drawn through zero difference as a guide. 122
26. (a) -- Chi-square map for the fit to $\Sigma^- \text{Pb}(11-10)$ data, Det B, group R2A. (b) -- Data and best fit including individual transition components. 123
27. Data and best fit for $\Sigma^- \text{Pb}(12-11)$ transition Det B for group R2A with horizontal scale: $E(\text{keV}) = (\text{Channel}+851.5) * 0.090$ 124

28. Data and best fit for $\overline{\Sigma}W(11-10)$ transition Det B for group R3 with horizontal scale: $E(\text{keV}) = (\text{Channel}+851.5) * 0.090$ 125
29. Results obtained for the individual fits to the tagged data with solid line corresponding to average result of $-1.111 \mu_N$ and dashed lines corresponding to $\pm 0.031 \mu_N$ statistical error. 126
30. Results obtained for the individual fits to the untagged data with solid line corresponding to average result of $-1.174 \mu_N$ and dashed lines corresponding to $\pm 0.027 \mu_N$ statistical error. 127
31. Results of tagged data grouped by transition and detector. . . 128

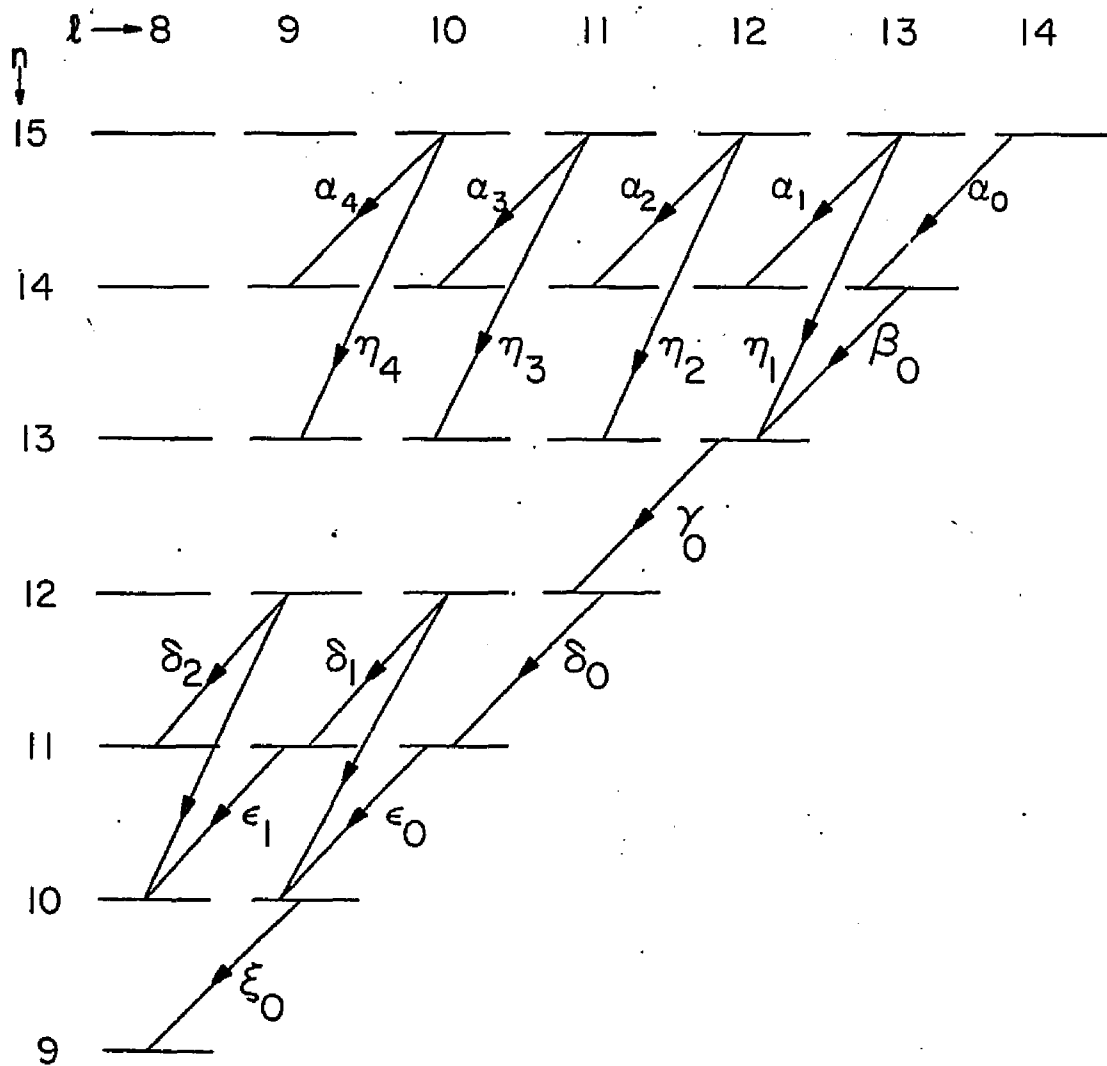


Figure 1

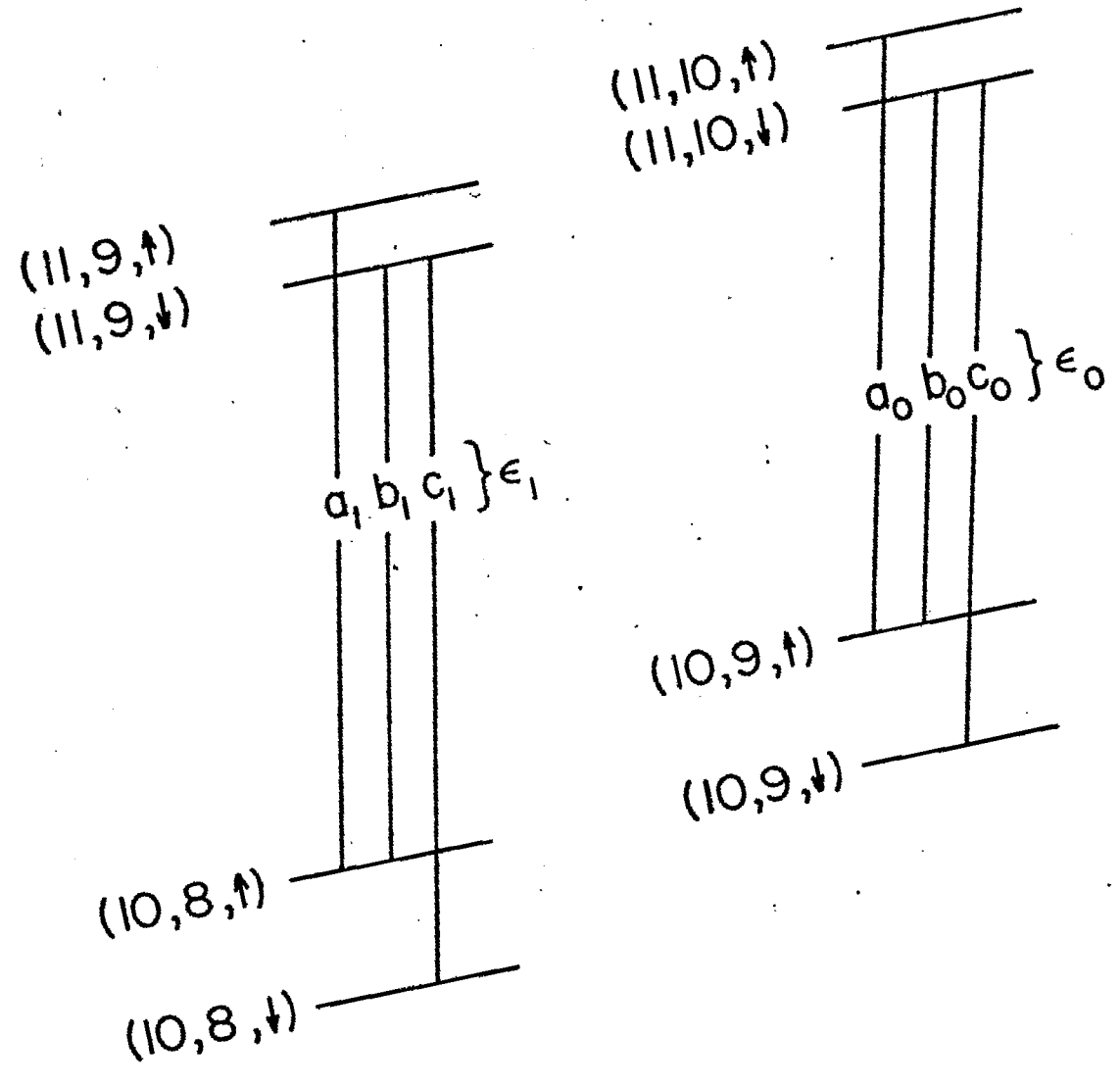


Figure 2

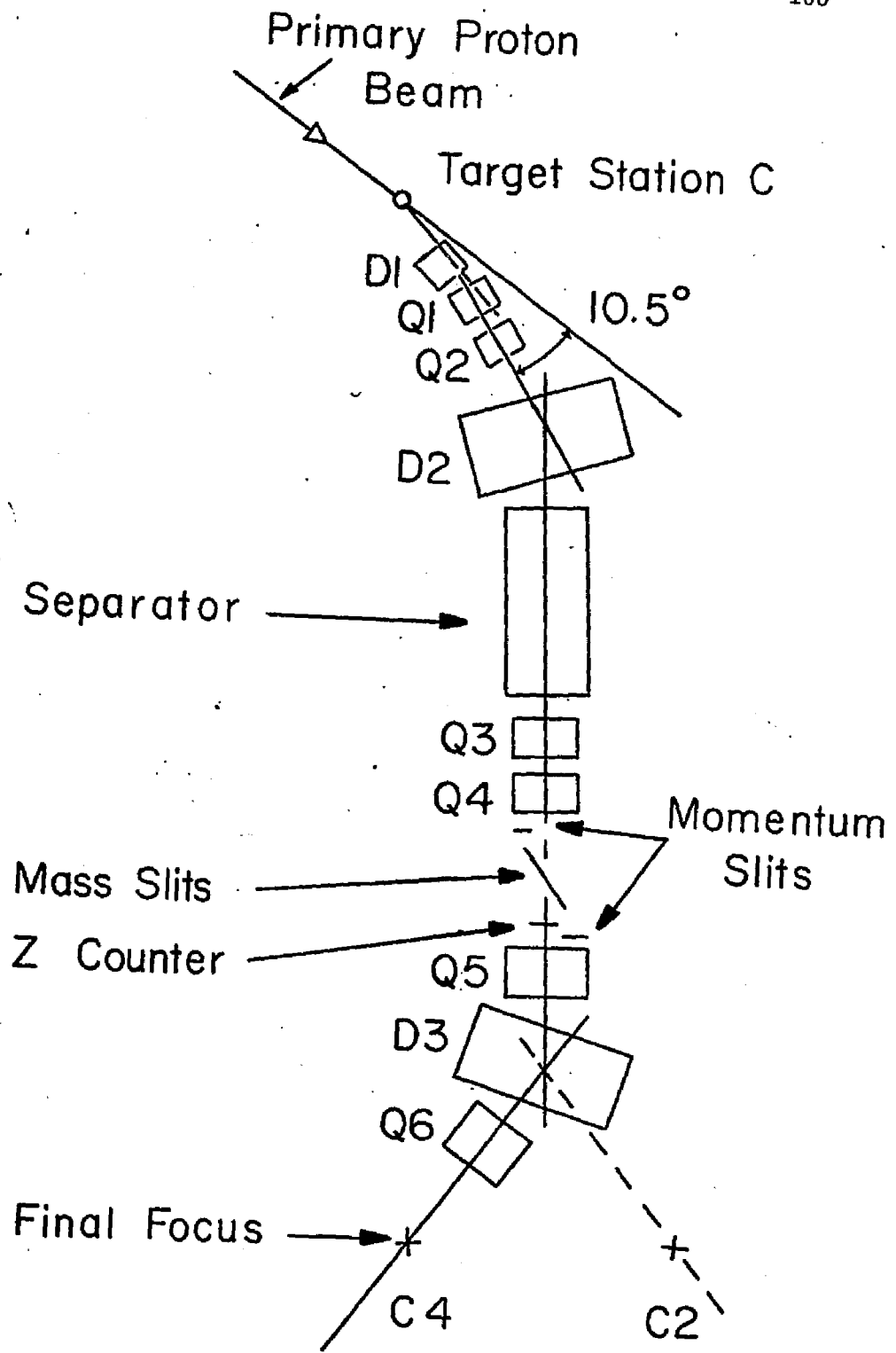


Figure 3

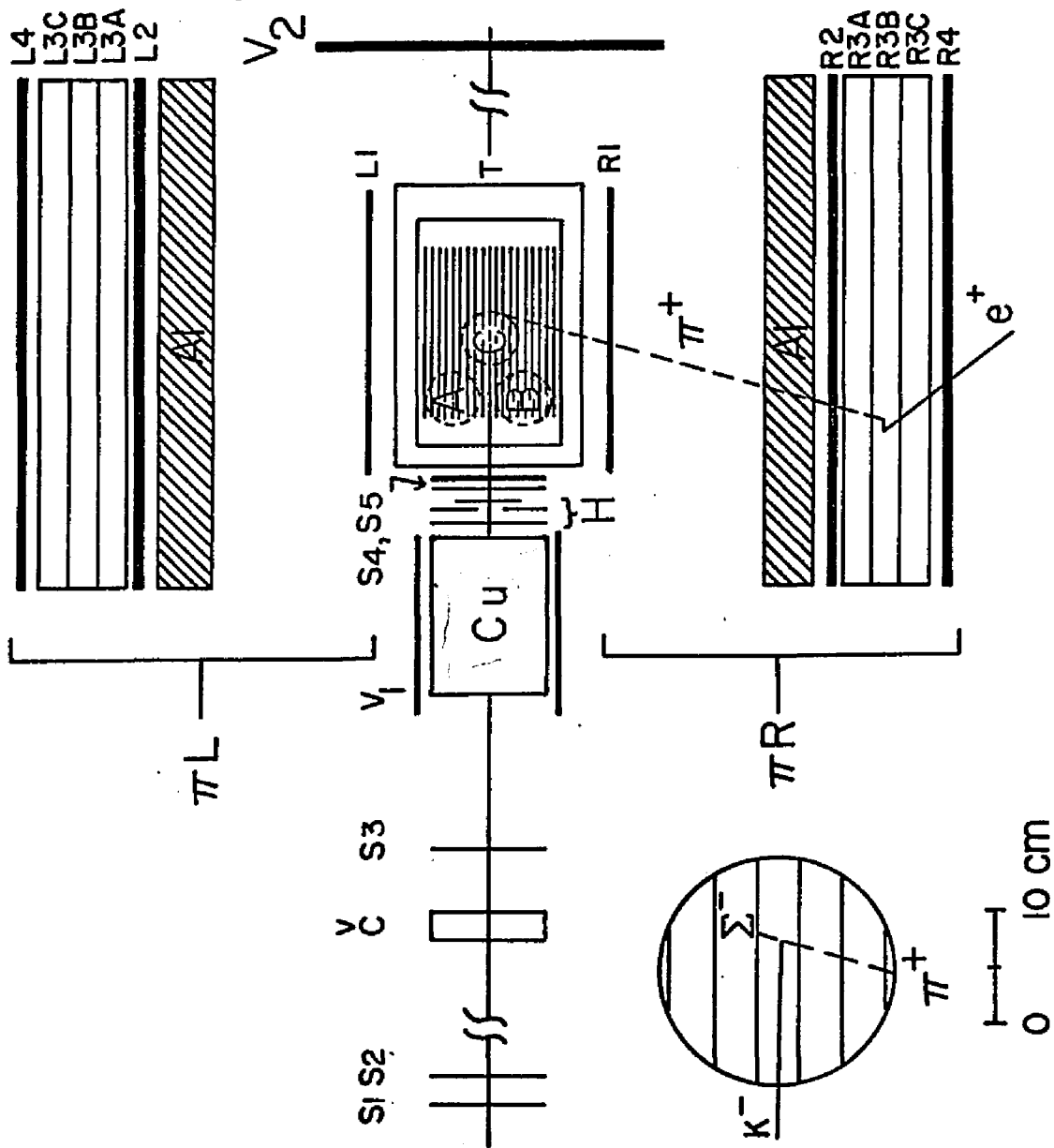


Figure 4

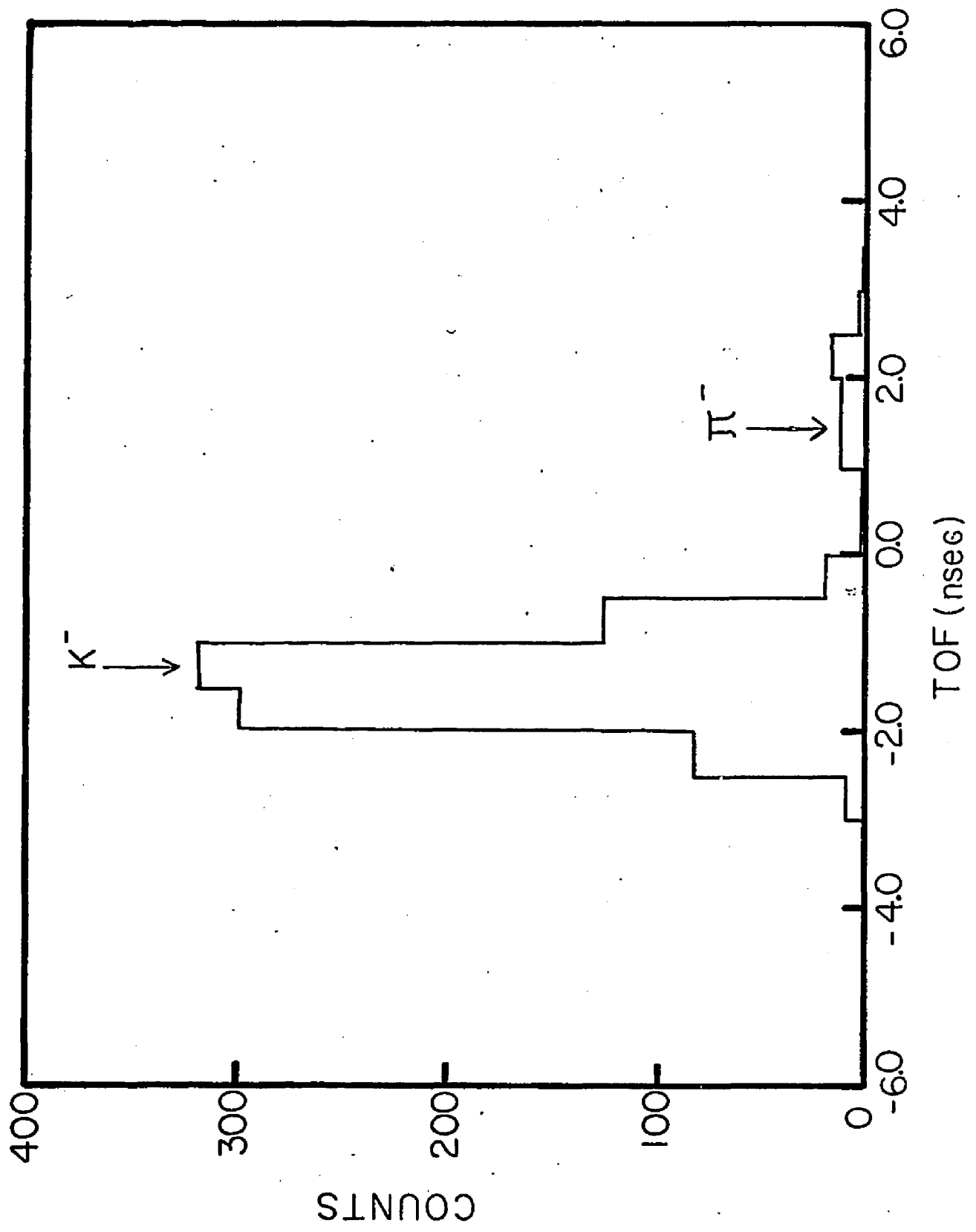


Figure 5

BEAM HODOSCOPE PROFILES

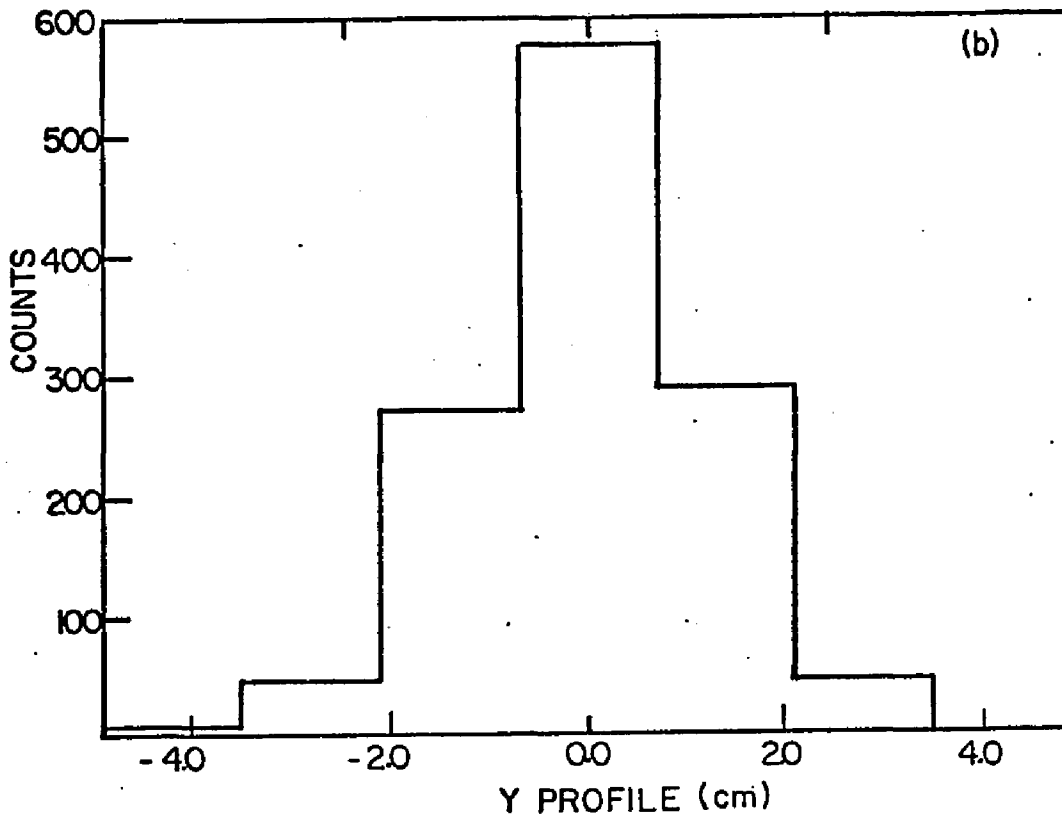
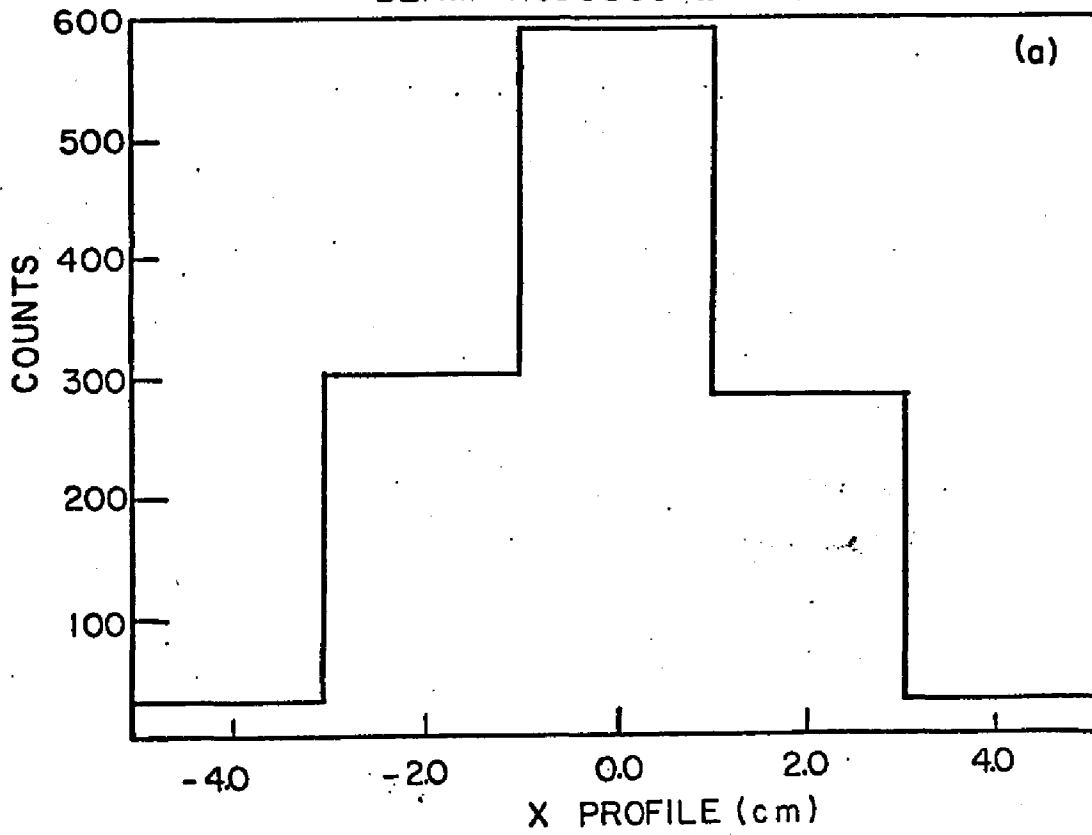


Figure 6

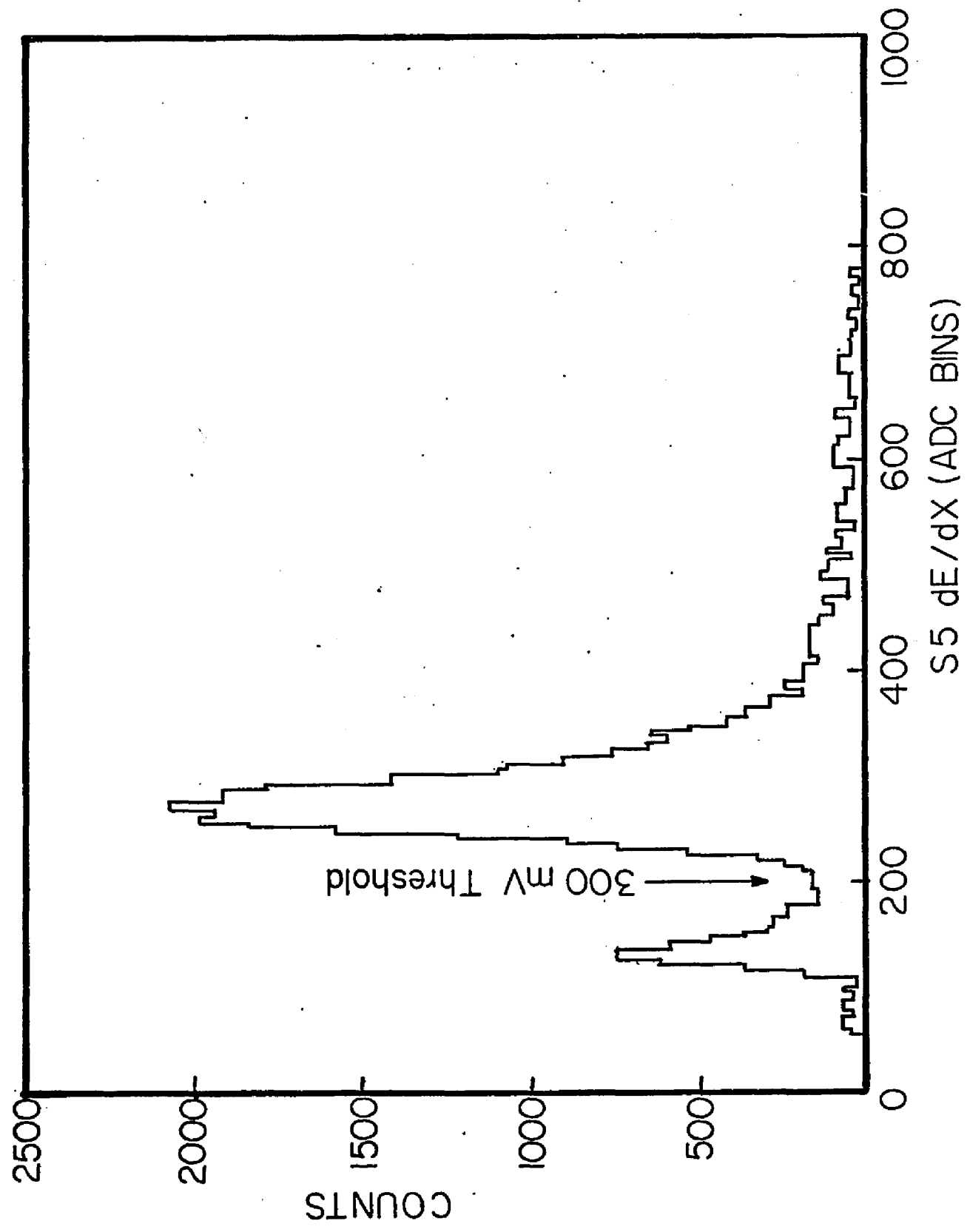


Figure 7

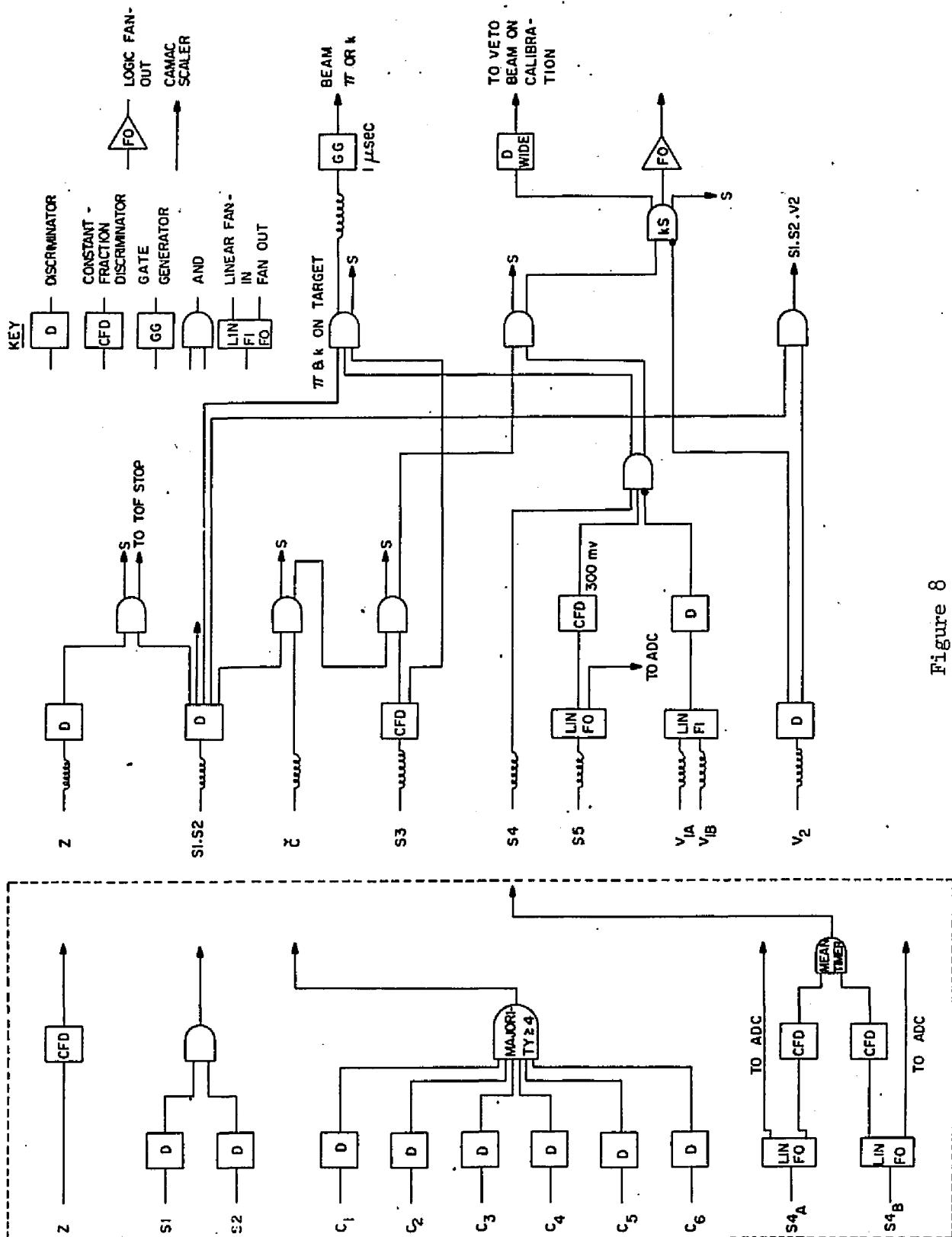


Figure 8

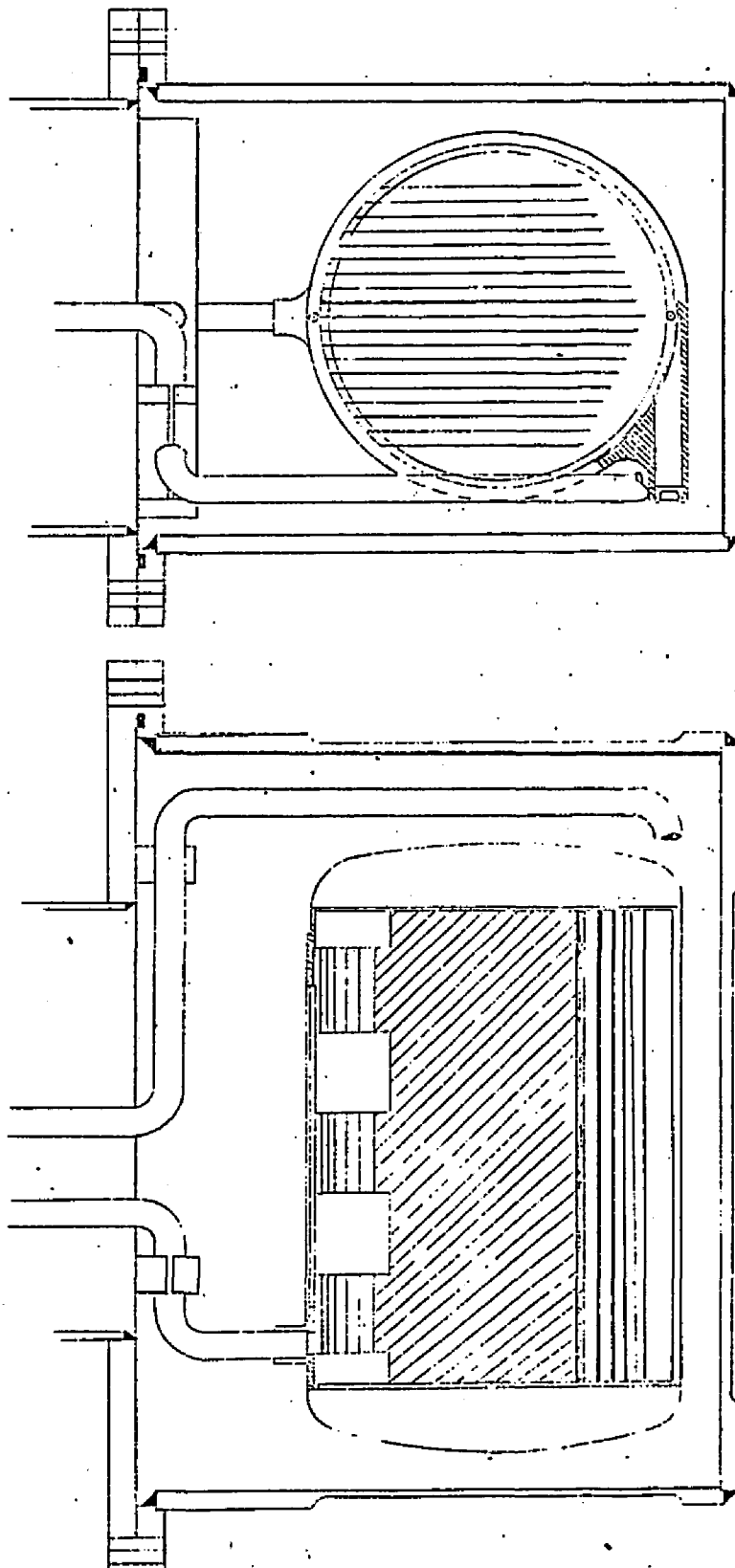


Figure 9

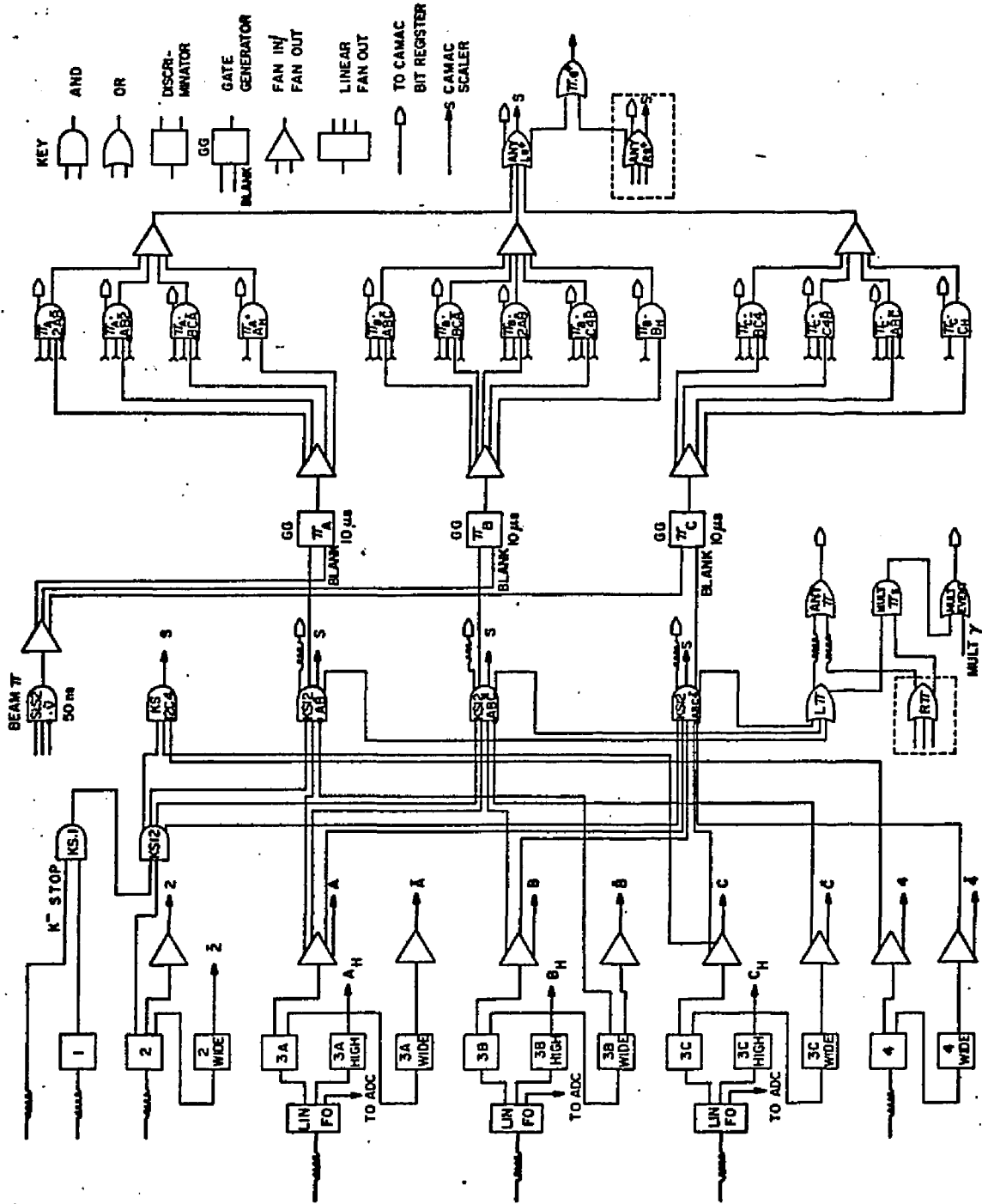


Figure 10

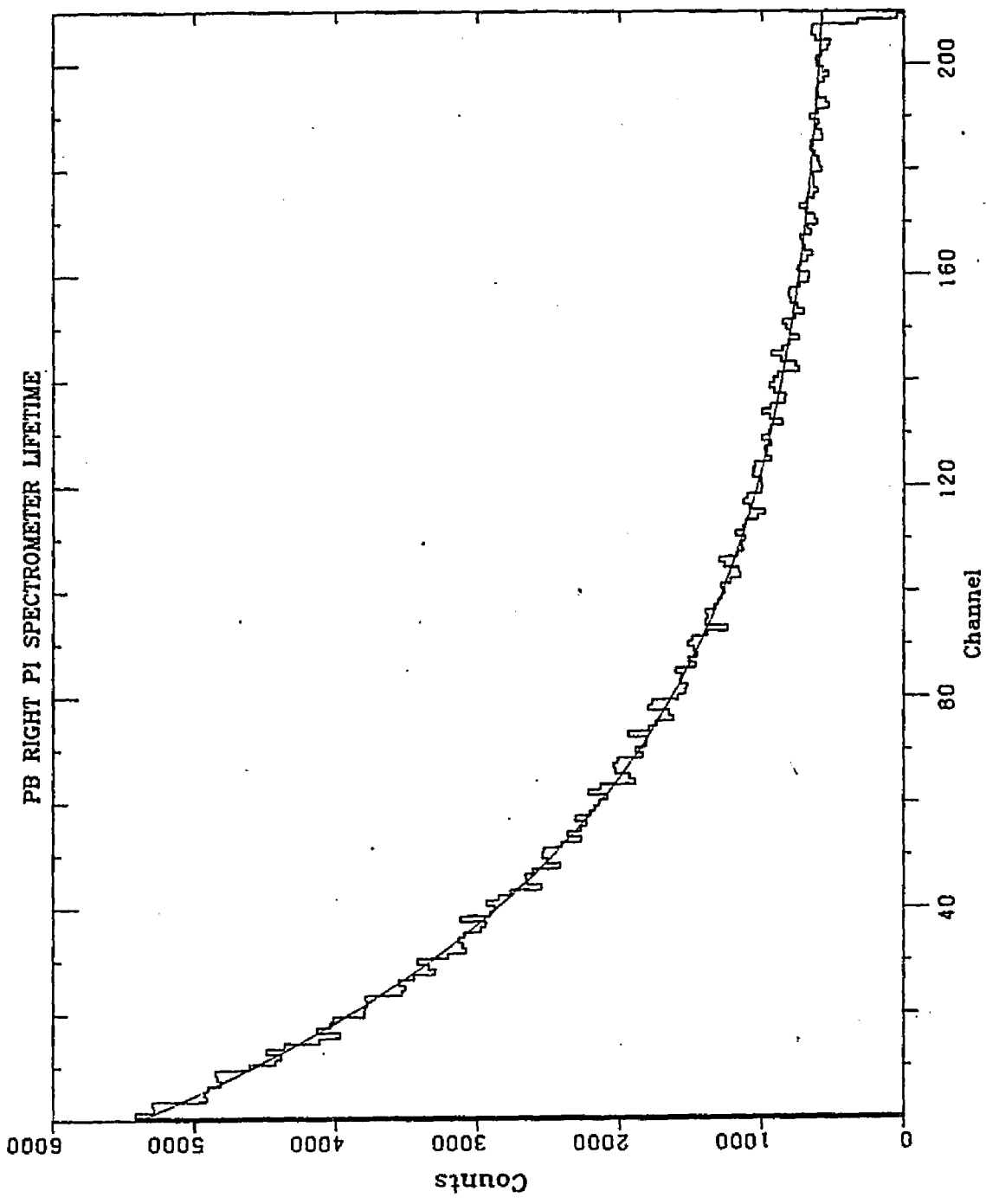


Figure 11

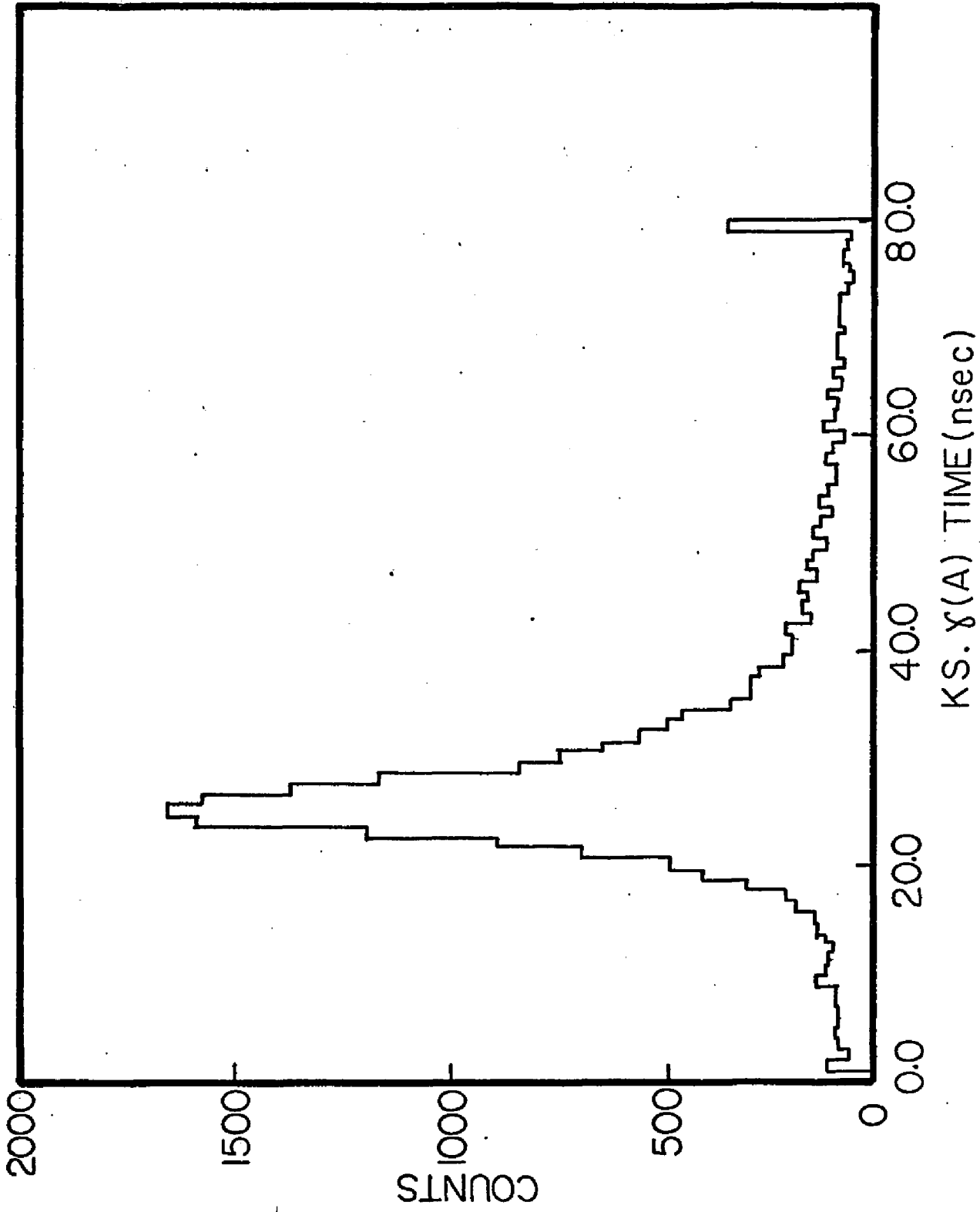


Figure 13

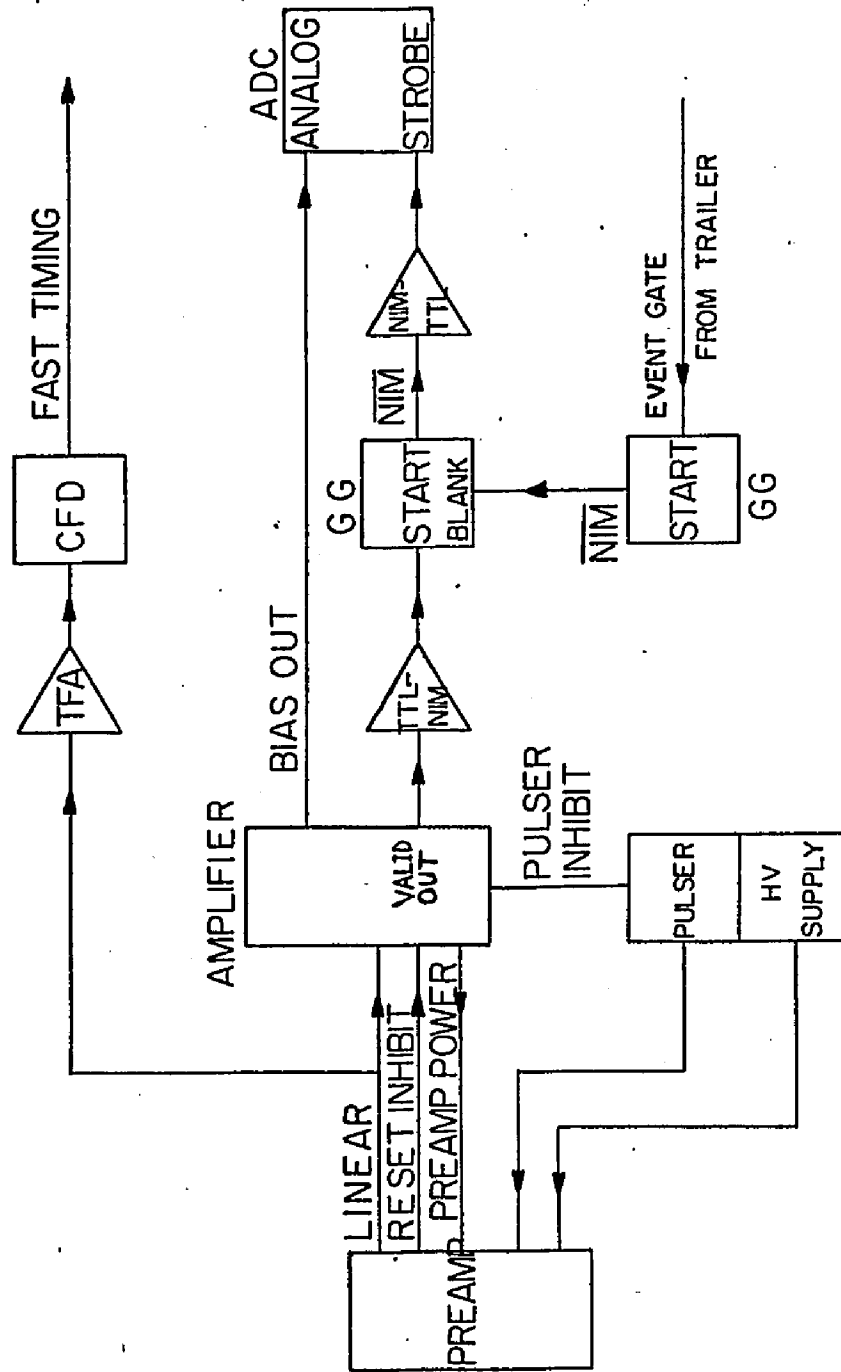


Figure 14

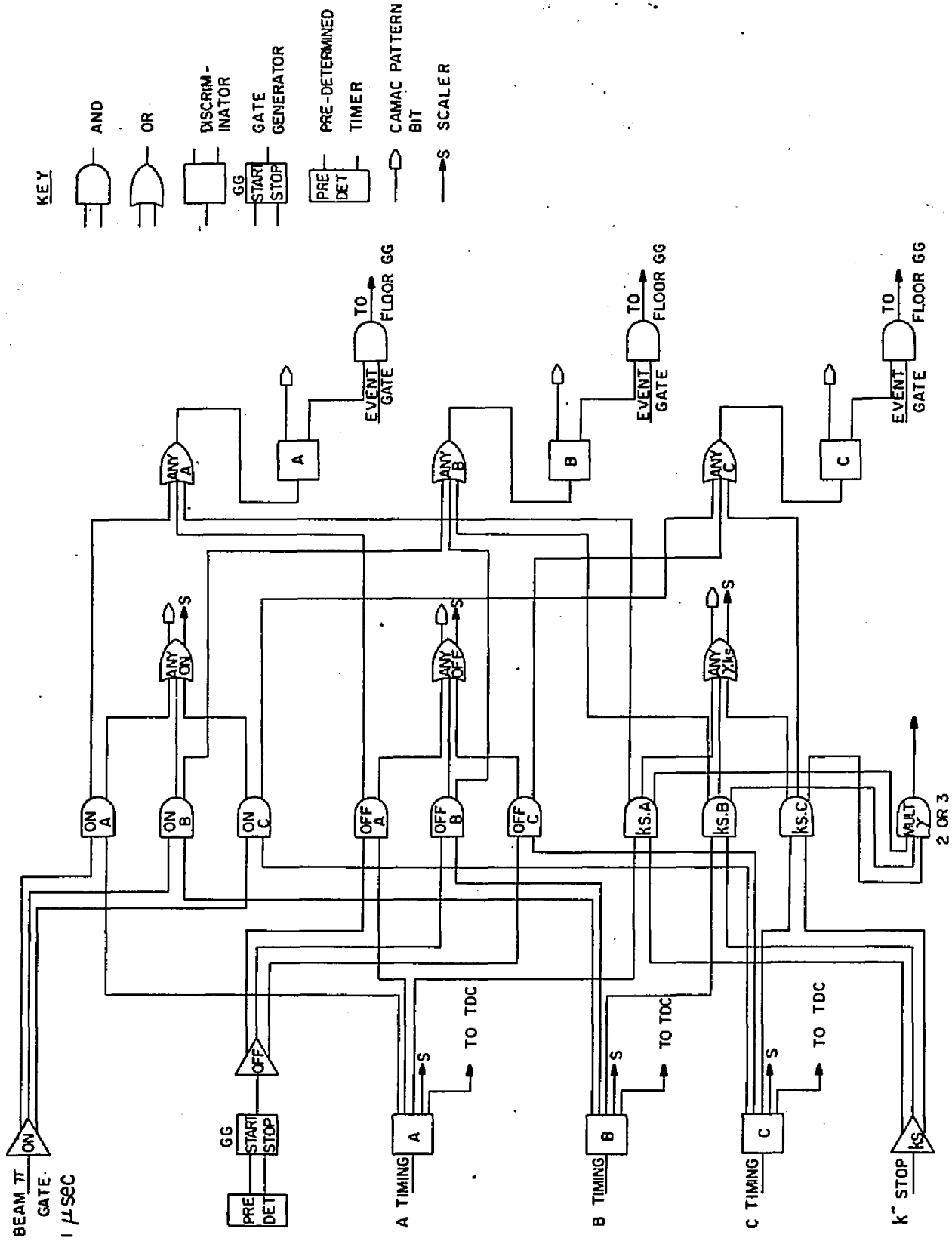


Figure 15

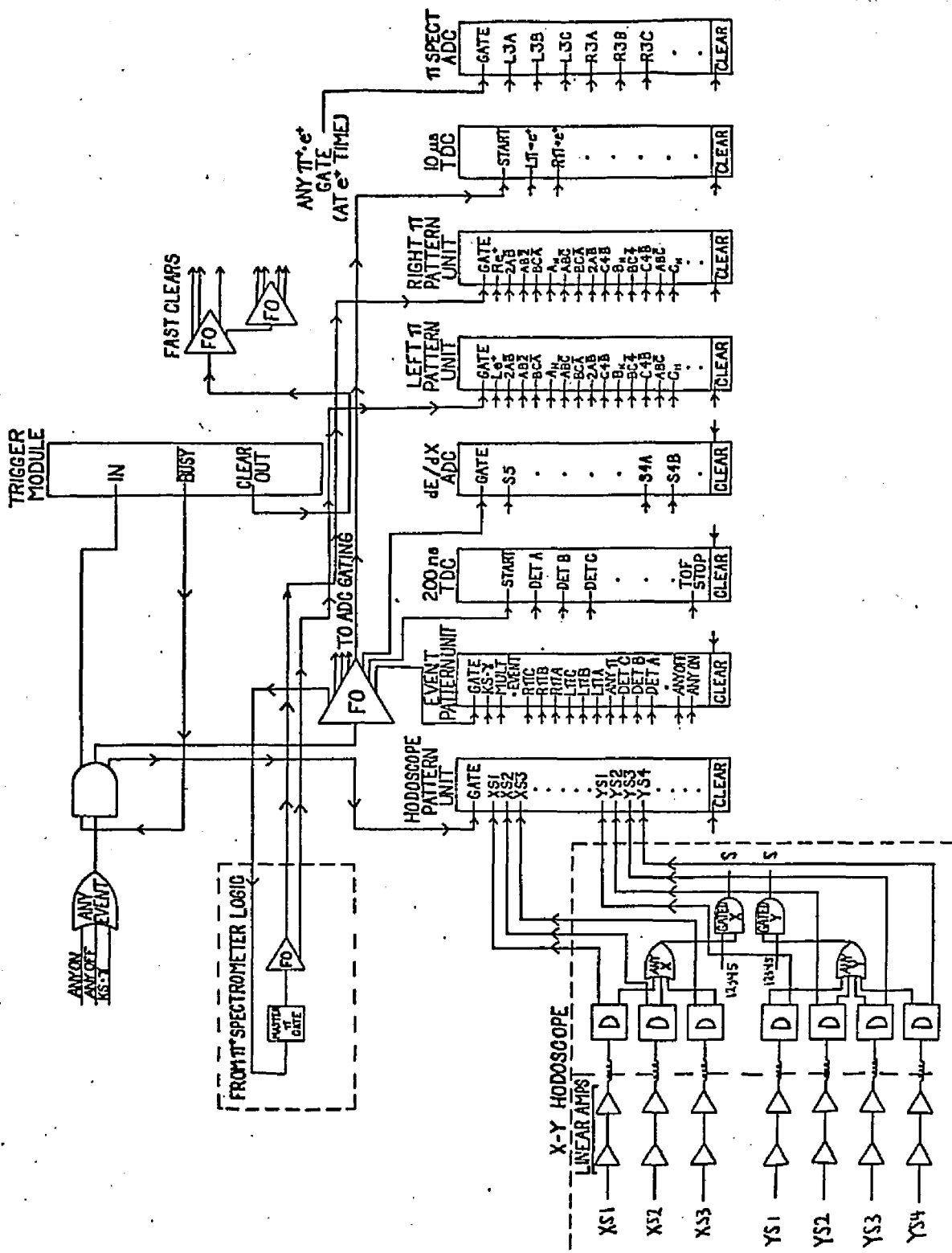


Figure 16

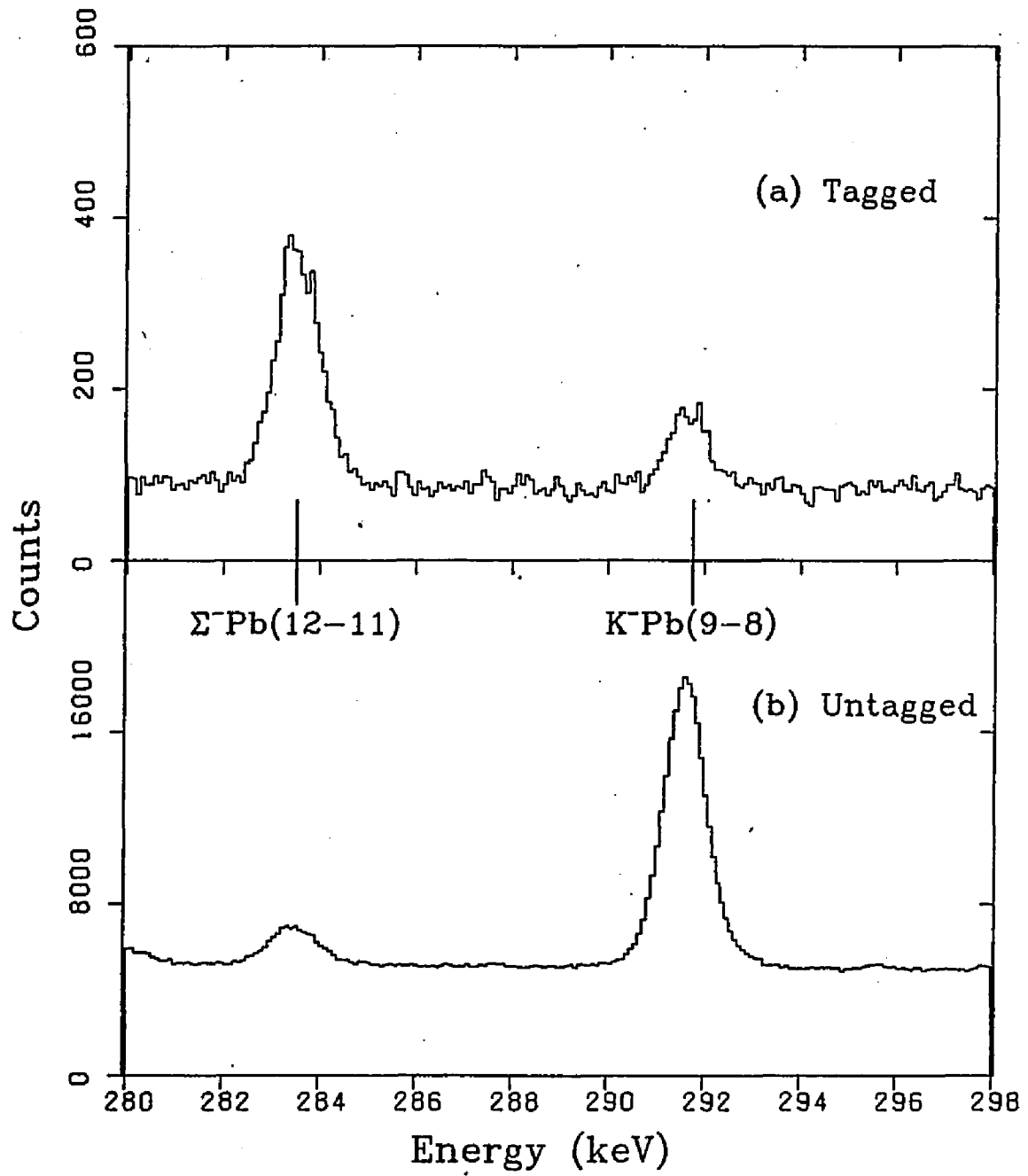


Figure 17

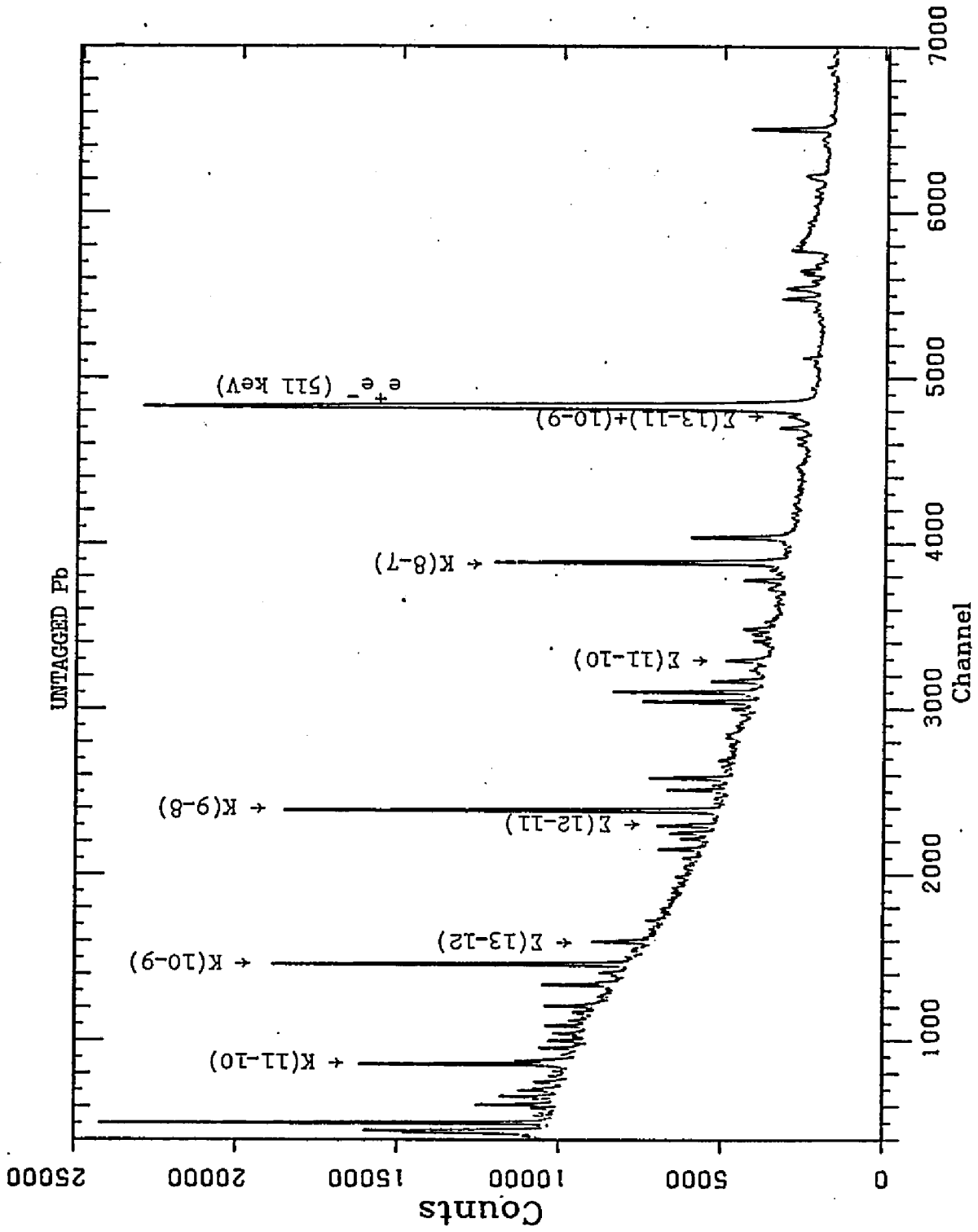


Figure 18

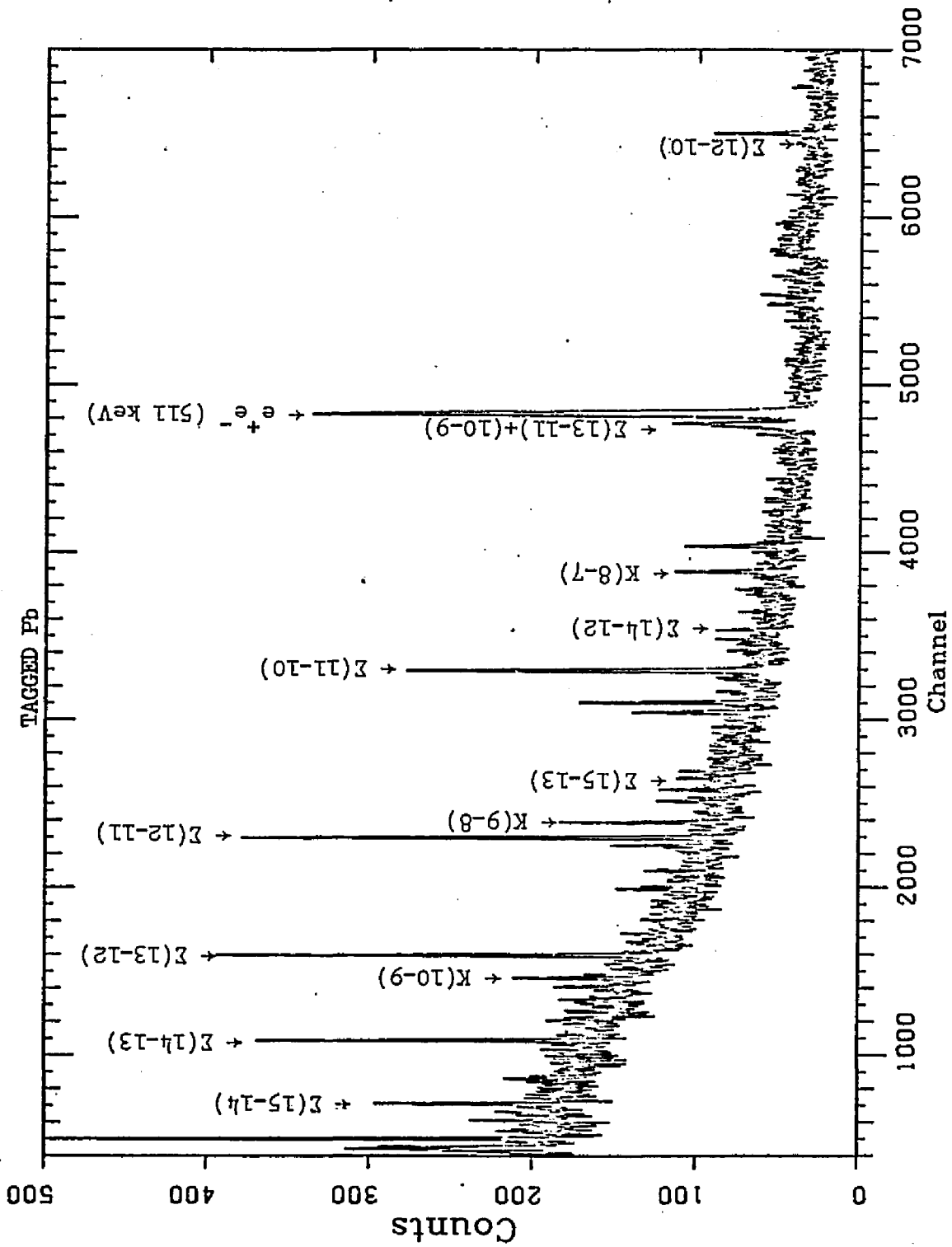


Figure 19

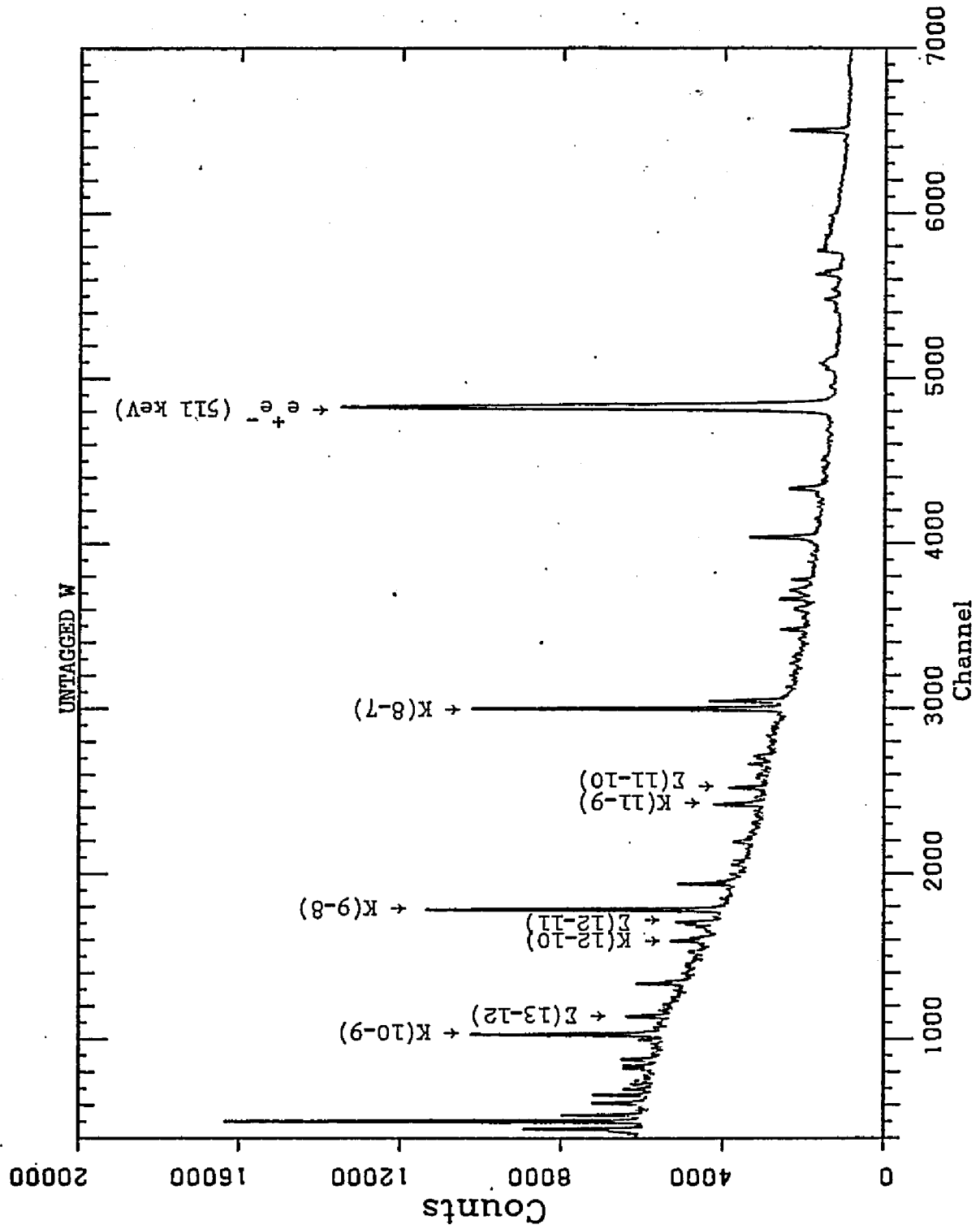


Figure 20

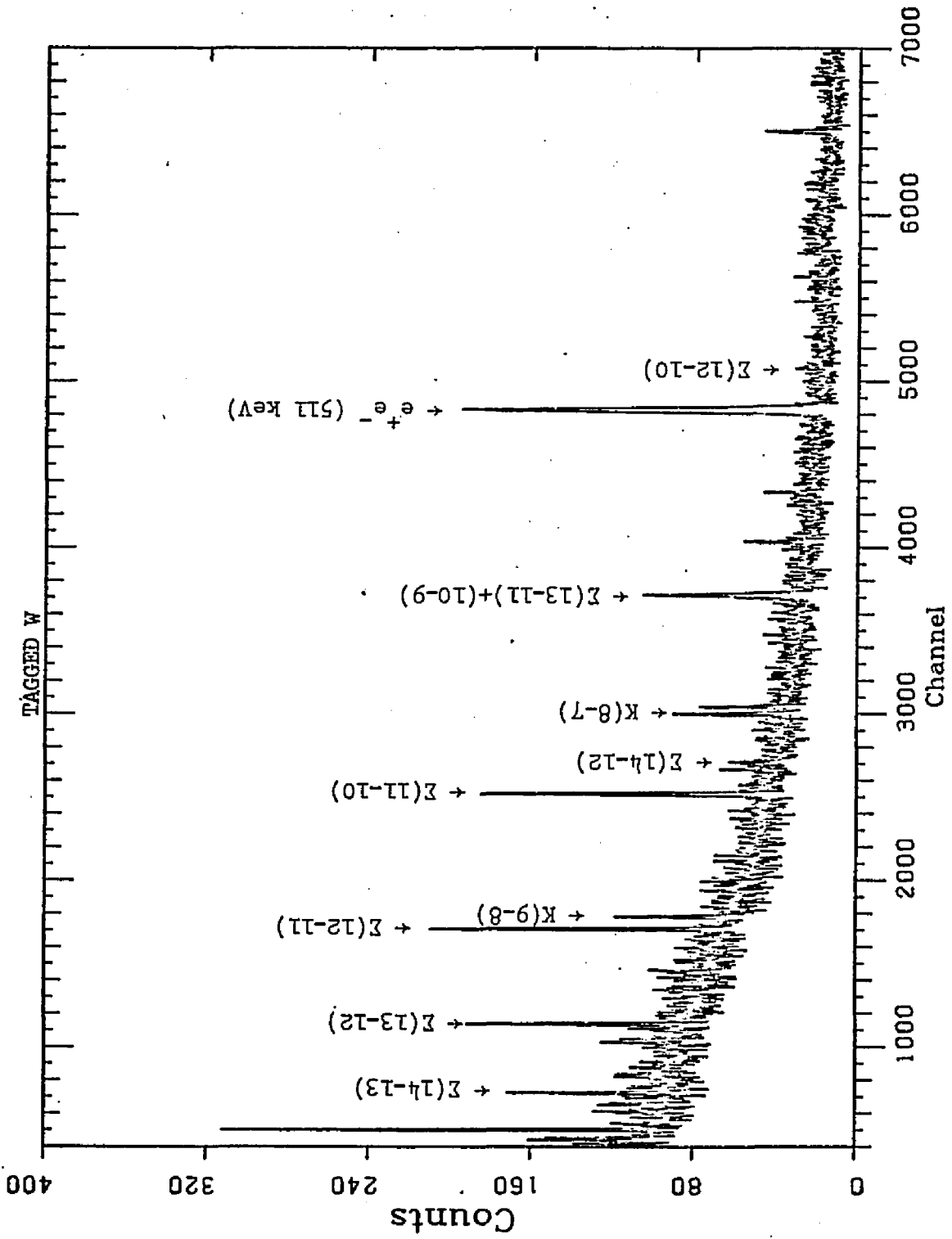


Figure 21

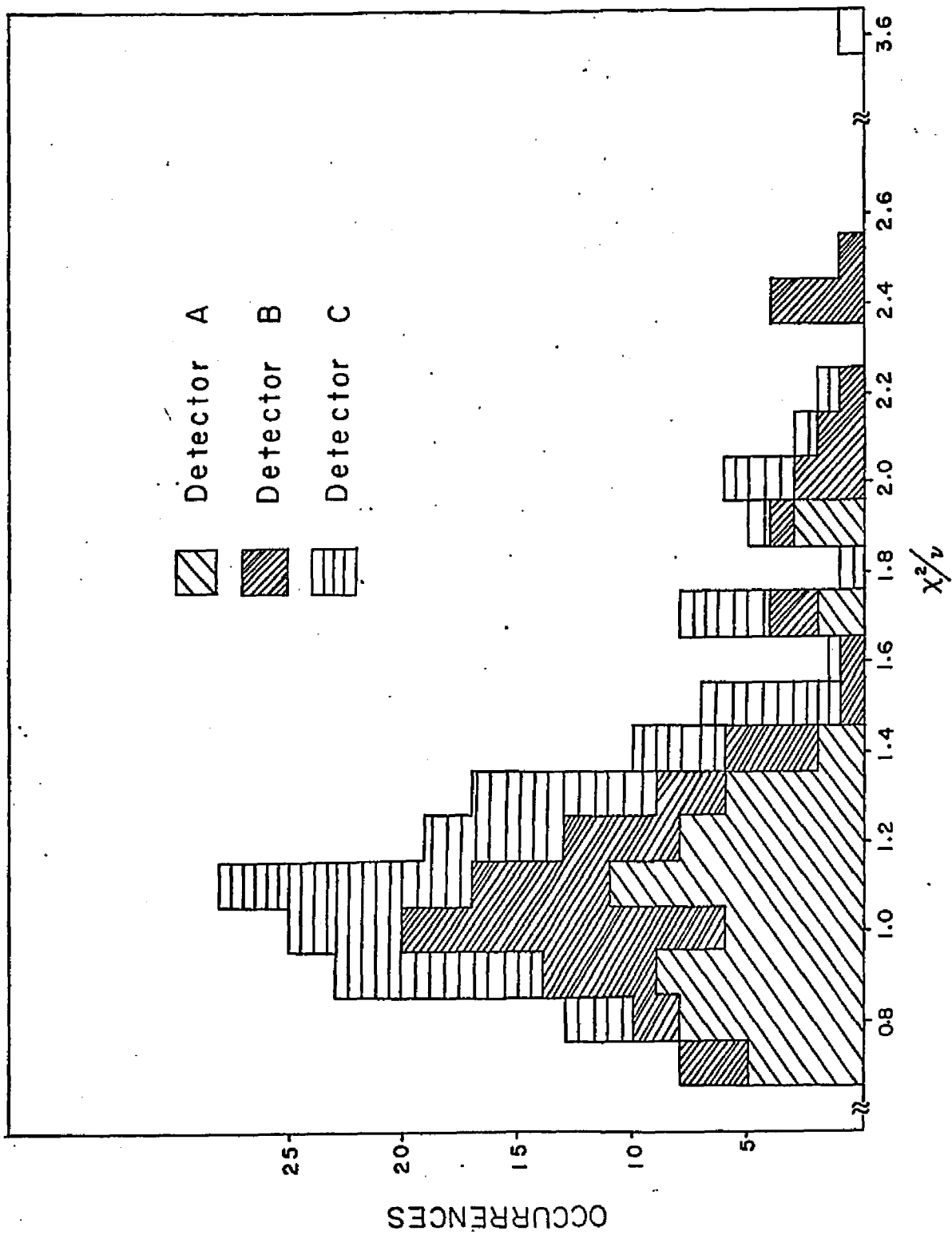


Figure 22

NO DEGRADER, 12 CM ABOVE DETECTOR
DET B SOURCES: BA IR SE EU

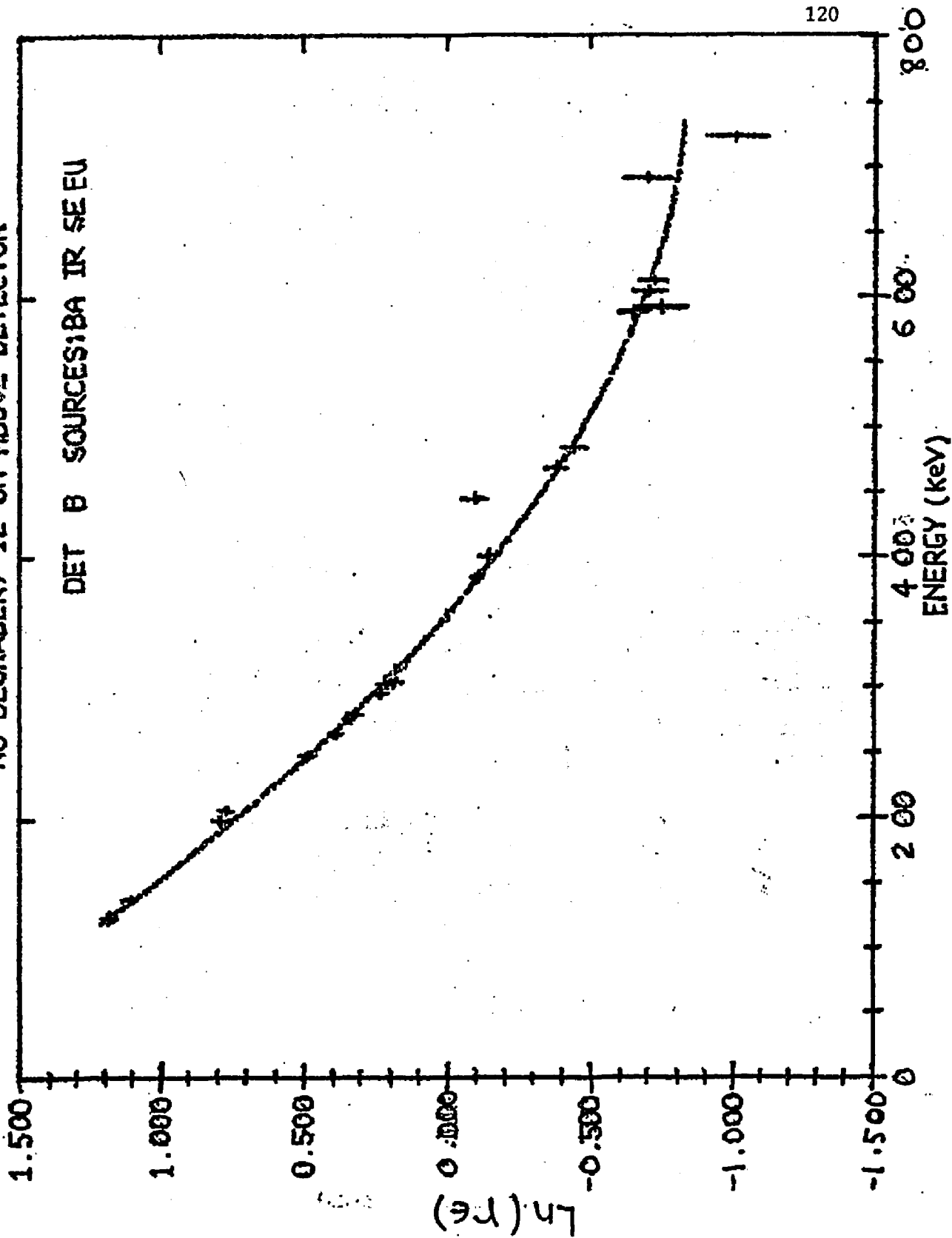


Figure 23

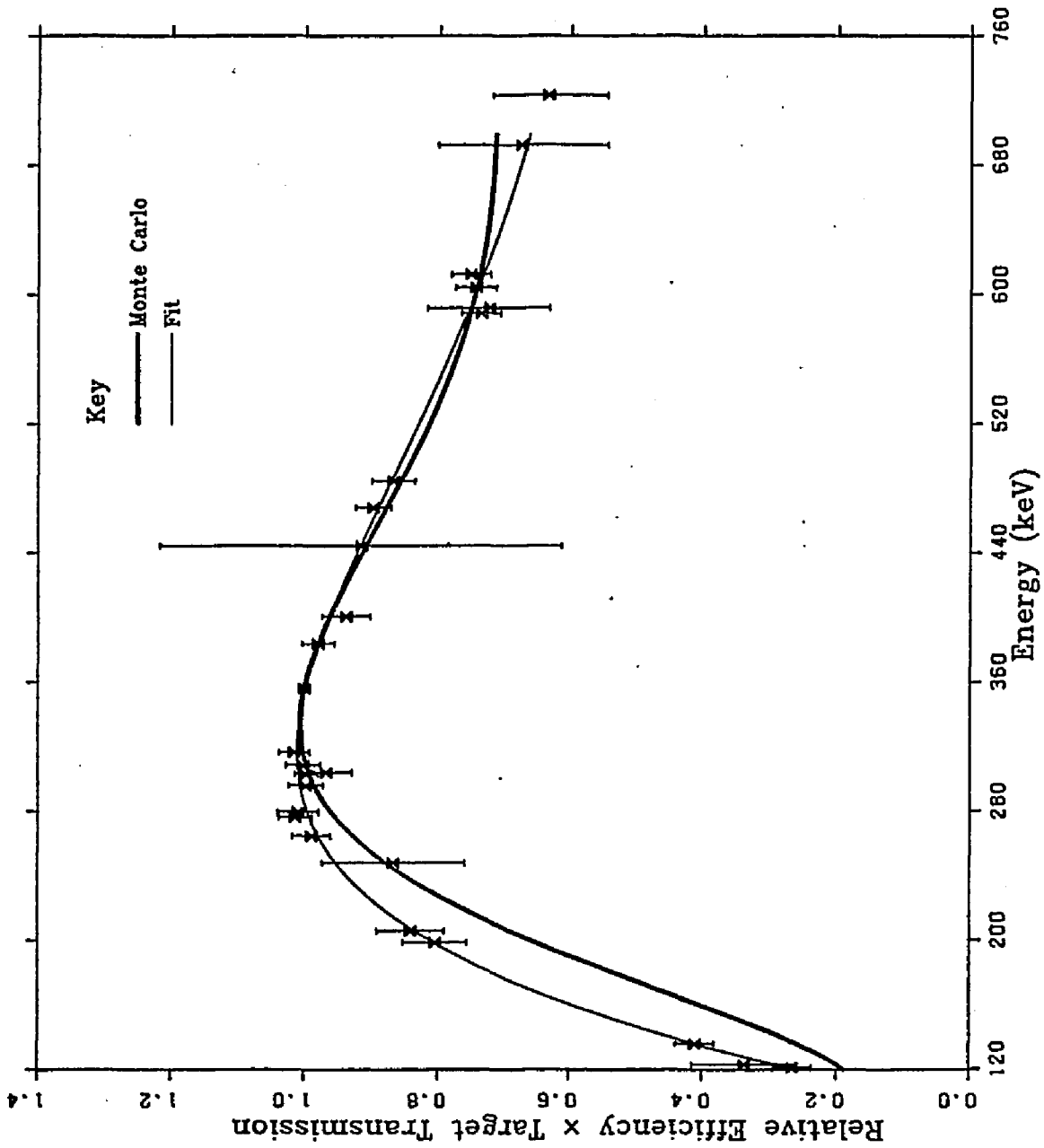


Figure 24

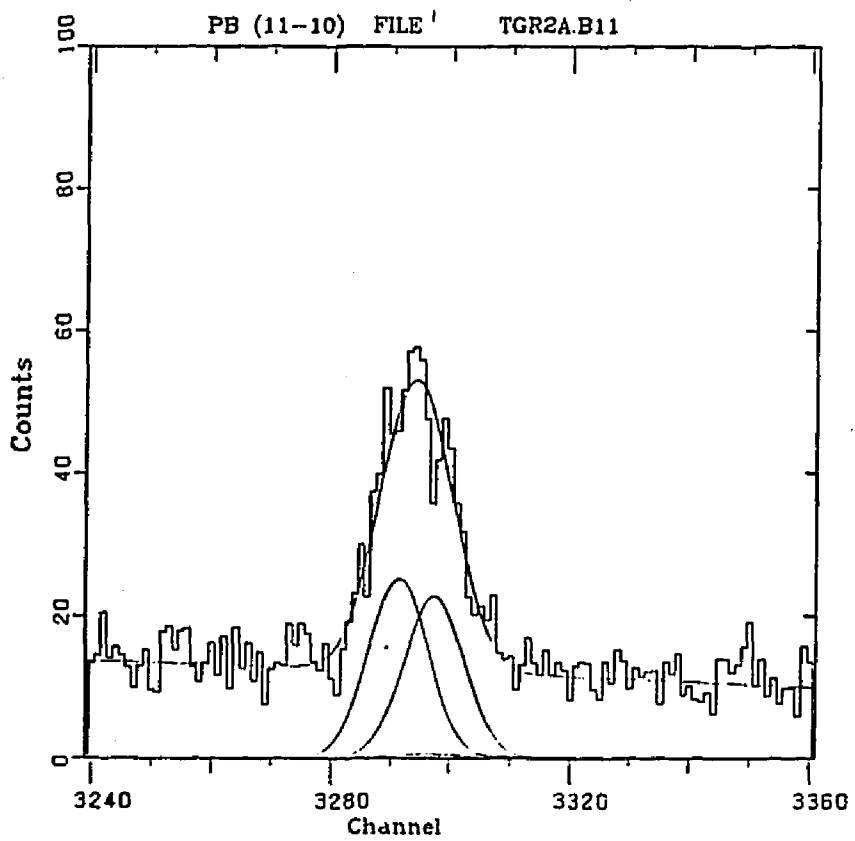
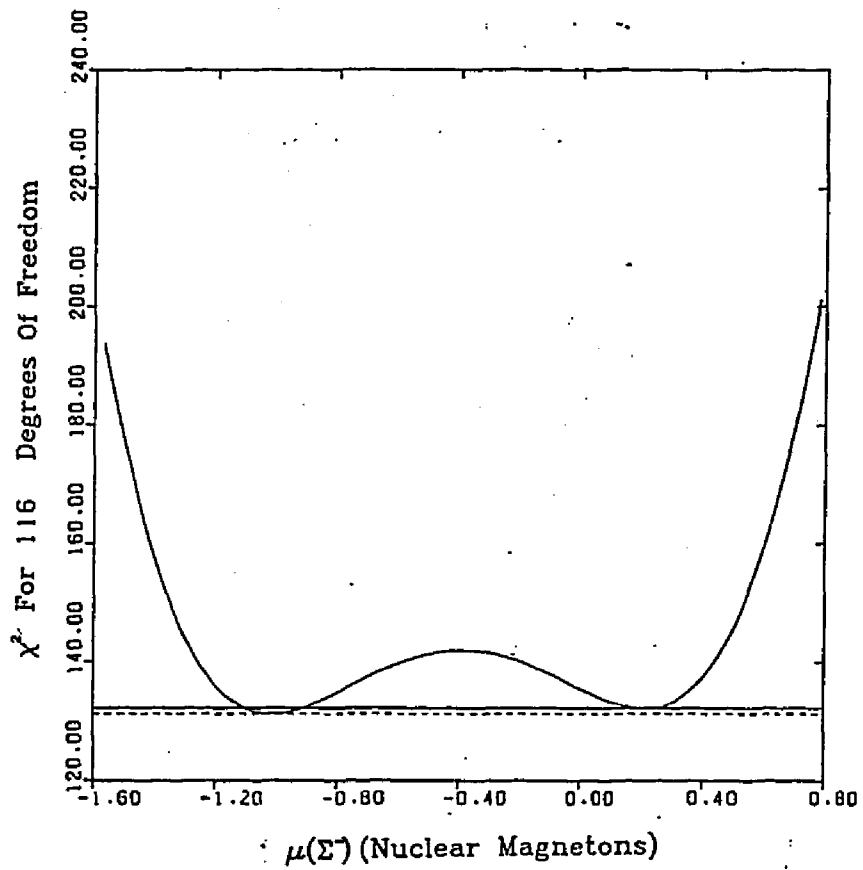


Figure 26

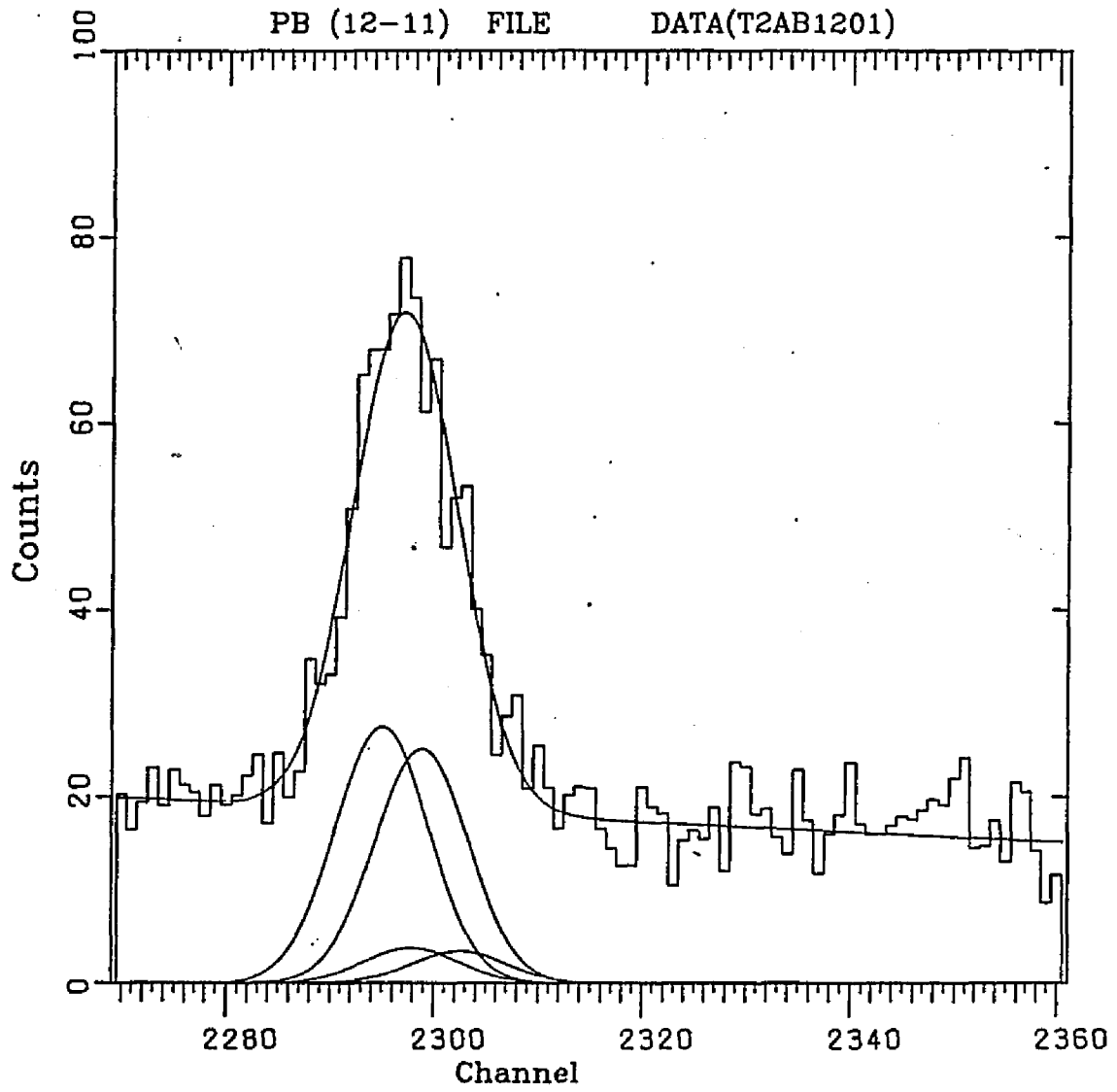


Figure 27

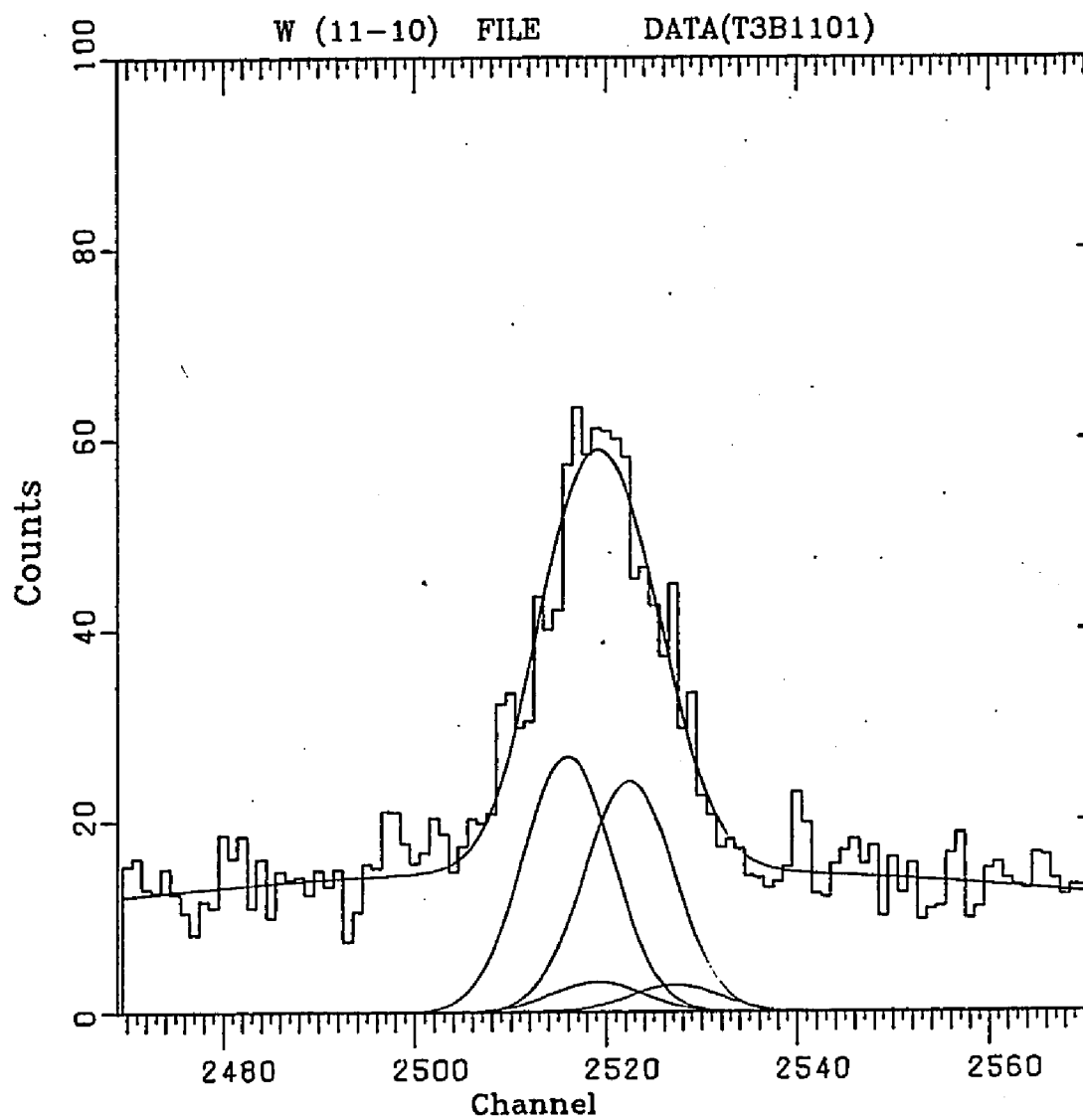


Figure 28

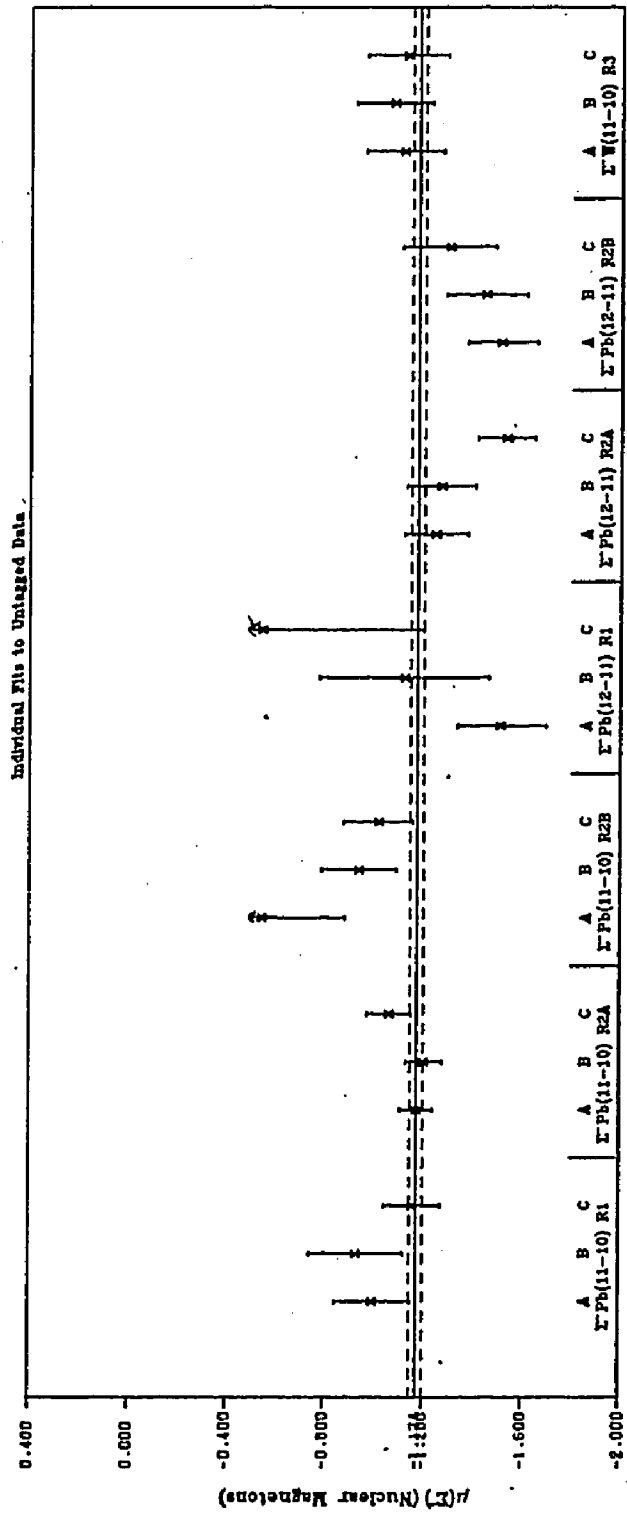


Figure 30

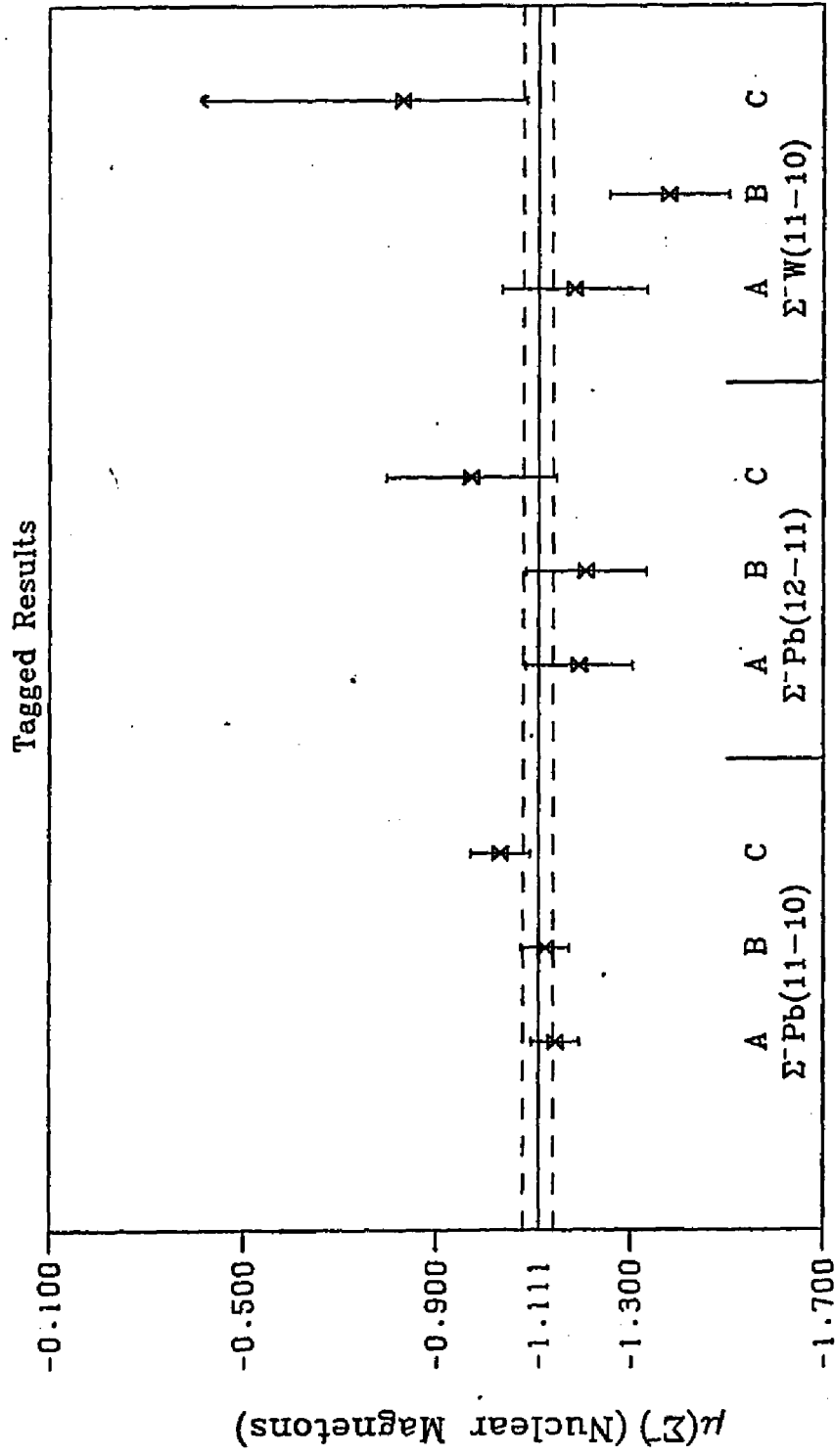


Figure 31